PRECISION AND MOBILITY ANALYSIS FOR MICROROBOT DESIGN AND CONTROL

by

MUHAMMED RAŞİD PAÇ

Presented to the Faculty of the Graduate School of
The University of Texas at Arlington in Partial Fulfillment
of the Requirements
for the Degree of

DOCTOR OF PHILOSOPHY

THE UNIVERSITY OF TEXAS AT ARLINGTON

December 2012

To my beloved wife Münteha and parents Emine and Mahmut.

ACKNOWLEDGEMENTS

I would like to first thank my supervising professor Dr. Dan O. Popa for his valuable advises, continued support, and encouragement. I am also thankful to Dr. Frank L. Lewis, Dr. Robert Magnusson, Dr. Brian L. Huff, Dr. Micky Rakotondrabe, Dr. Aditya N. Das, and Dr. Zeynep Celik-Butler for serving in my dissertation committee.

I acknowledge the support from University of Texas at Arlington Research Institute (UTARI) which provided access to a wonderful facility and professional research environment. I owe special thanks to Dr. Aditya N. Das, Dr. Rakesh Murthy, and Dr. Mohammad Mayyas for their technical advises and help with setting up experiments at UTARI. I am indebted to Dr. Rakotondrabe for being a source of inspiration in our research collaboration. Many thanks to my past and present colleagues at UTARI and Next Generation Systems (NGS) research group for all the support and friendship they have given. I am also grateful to the Department of Electrical Engineering (EE) for giving me the chance to serve as a graduate teaching assistant (GTA) for the Control Systems course and to earn the outstanding GTA award. I owe thanks to Dr. Popa, Dr. Lewis, Dr. Jonathan Bredow, and Dr. Kambiz Alavi for their mentorship towards being a better teacher. I truly appreciate the kind help of the administrative staff of the EE Department and UTARI in fulfilling many logistic tasks.

I cannot thank enough to my wife and parents who have been committed to my success and have given a wholehearted support all along. This thesis is dedicated to them, with love and gratitude.

November 13, 2012

ABSTRACT

PRECISION AND MOBILITY ANALYSIS FOR MICROROBOT DESIGN AND CONTROL

Muhammed Raşid Paç, PhD

The University of Texas at Arlington, 2012

Supervising Professor: Dan O. Popa

The emerging field of microrobotics extends from manipulation of nanostructures to 3D assembly of micromachines, and to control of motile bacteria as manipulation tools. Microrobots are not necessarily small themselves but the smallest scale in which they operate is measured in micrometers. Microrobots have to be precise, fast, and flexible to be useful as top-down manufacturing tools. As the relative magnitudes of uncertainties and errors with respect to the operational precision of robots grow towards smaller scales, the requirement for better precision increases. Hence, the concepts of precision analysis and precision-based design are important steps in microrobotic system development. In the case of microrobotic systems involving untethered micro-agents, the primary research focus is on the mobility of the micro-agent and controlling its degrees of freedom. Both of these topics, however, have been insufficiently addressed to date although they constitute a decisive consideration towards the ultimate success of the technology.

This thesis investigates how to analyze the precision of a microrobot and how to design it based on given precision requirements. Considering the kinematic descrip-

tion of a robot as a mapping between its parameter-space and task-space, we develop a new mathematical formalism for precision analysis and design of robots via interval extension of robot kinematics. An interval is a closed set of numbers represented by its two bounding values. We use intervals to represent uncertain and erroneous parameters in a kinematic description and extend the products of exponentials (POE) formulation to intervals. We define interval functions that take the uncertain POE parameters of a manipulator as input arguments and calculate the forward kinematics map to produce an interval result. We show via theorem-proof pairs, simulations, and experiments that the distribution of the end-effector position due to uncertain kinematic parameters can be bounded using our method. This formulation helps understand the effects of mechanical and sensing errors on the positioning precision of a micromanipulator. Hence, it can be used as a performance evaluation method towards automating a microassembly process. We also propose a new method of precision design of robots by applying our interval POE formulation to the inverse kinematics problem. This provides the bounds on the individual error terms of the parameters such that custom design or configuration of a microrobotic system for a particular end-effector precision requirement can be done. For the microrobotic systems employing a micro-agent as the tool, analysis and control of mobility requires a similar mapping between the parameter-space and the task-space of the micro-agent. To address mobility, we propose a novel power delivery and motion control method based on use of pulsed laser. Simulation and experimental results show that power delivery to a micro-agent is possible with pulsed laser and mobility with multiple degrees of freedom can be achieved.

TABLE OF CONTENTS

APPENDIX

LIST OF ILLUSTRATIONS

LIST OF TABLES

CHAPTER 1

INTRODUCTION

The success of conventional manufacturing is owed mostly to the capability of mass production. Producing goods in a fast, timely, predictable, and precise manner was made possible with the introduction of automation in the factory floor and it has been a vital component of modern manufacturing systems since then. Factory robots have been the face of automation as they replaced human workers in many operations that require fast pace, high accuracy and repetition or in operations that are dangerous for humans.

One of the areas in which manufacturing automation found extensive use is microchip production. It has proved to be one of the most sophisticated industries in terms of product quality and complexity thanks in part to the precision of the associated production systems. The possibility of making increasingly small, complex, and cheaper circuits had initiated the philosophy of miniaturization which then penetrated into the other manufacturing fields related to metrology, instrumentation, telecommunications, and many more. As the concept of miniaturization has been adopted by various industries, the requirement for automation in general and for high precision robots in particular arose to make the idea of miniaturization both technically and economically viable.

Microrobotics was initially conceived as a field of research towards understanding and controlling the microworld via sensing and manipulation [1–5]. Besides, as part of the miniaturization trend, microrobotics has advanced in the past decade towards being an enabling technology for manufacture of systems that involve very

small and heterogeneous components [6, 7]. While miniaturization is an objective of microrobotics in all facets of the technology, currently microrobots are not necessarily "small" themselves but they have end-effectors and sensors that operate at the micro-scale. Indeed, the definition of microrobotics by Bellouard is:

"...a technology discipline that refers to design of systems capable of physically interacting in a controlled and prescribed manner with millimeter and sub-millimeter objects [8]."

Microrobotics has built upon many disciplines ranging from microelectronics and mechatronics to materials science and nanotechnology. For instance, concepts of precision engineering lie in the foundations of microrobotics since the required operational precision is very high. Similarly, the techniques of microelectronics fabrication led to the invention of micro-electro-mechanical systems (MEMS) which can create $2\frac{1}{2}$D micro-devices via additive and subtractive processes. In addition to monolithic microfabrication, other micromachining techniques such as laser cutting and micromilling are used to make micro-scale parts. Today, commercially available micromachining services such as MEMSCAP MUMPS [9], Sandia SUMMIT [10], and Microfabrica MICA Freeform [11] processes can achieve manufacture of complex microstructures. However, a limitation of these state-of-the-art technologies is the lack of heterogeneous integration capability. In other words, these fabrication processes can only handle a very limited number of material types and forms. Microrobotics offers a solution to this limitation via a set of top-down robotic assembly processes that is called microassembly [12]. Devices that can be built through microassembly may vary from a miniaturized sensor [13] to robotic micro-agents that are themselves small [14]. These micro-agents are used as manipulation and sensing instruments under the control of a larger system for micro/nano-manufacturing, material characterization, and biomedical purposes [15].

Robotics in micro-scale is different from macro-scale robotics in several ways. The dominant physical principles that govern interactions in micro-scale are significantly different than those in the macro-scale. Along the scale down, the surface-to-volume ratio of objects increases which makes surface effects and forces become dominant. This is called the scaling effect [16]. For instance, weight of a micro-object becomes negligible in comparison to its surface area. Hence, the forces that control its motion are mostly surface-based such as van der Waals, capillary, and electrostatic forces [16, 17]. Also, the nature of the micro-scale forces change significantly depending on the environmental conditions, interacting materials, and their chemical and electrical conditions [18]. The different characteristics of these forces require a whole new set of interaction schemes between microrobots and micro-objects [19].

From a control systems perspective, robotics in micro-scale is also more challenging. First, incorporation of feedback sensors into the micro-world is often very difficult. The most common ways to acquire information from a microrobotic system is via imaging using optical or electron microscopes [20–22]. In certain cases, force or tactile feedback is also possible [21]. However, signal-to-noise ratio is generally very low and the required precision is comparable to the amount of errors and uncertainties in the system [23]. Given all these challenges, there appears to be a large area yet untouched by research that will extend from robotics into the micro-world.

A typical microrobotic system is composed of several fundamental elements such as motion control hardware, manipulation tools, cameras with high magnification objectives, data acquisition electronics, and a computer control system. An illustration of such a typical configuration is given in Figure 1.1. The elements of a microrobotic system are connected to each other as depicted in Figure 1.2. The interactions between these elements are shown with arrows. Figure 1.2 describes a general control system structure where the actuators are controlled to perform ma-

nipulation tasks in the workcell from which certain measurements are fed back to the control computer. In some of the microrobotic systems, mobile micro-agents are employed in the workcell to perform manipulation tasks. These agents are powered and controlled wirelessly and are targeted mostly for biomedical applications such as cell manipulation and minimally invasive surgery [15, 19]. In this thesis, we refer to such systems as micro-agent systems.

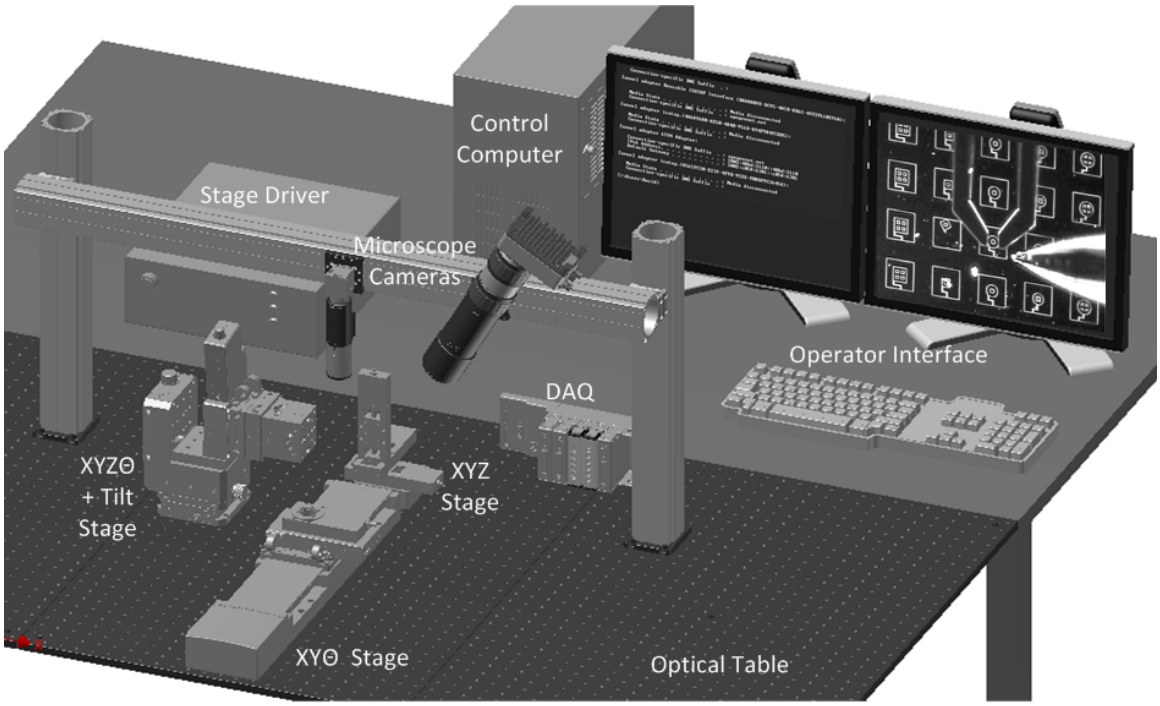

Figure 1.1. A typical microrobotic system.

Depending on the type of the microrobotic system, the user has an operator or supervisor role. If the system is teleoperated, then the user is the operator who manually controls certain interface devices such as keyboard, mouse, and joystick to drive the manipulators and perform robotic operations. Also, the operator is responsible for interpretation of the sensory data and sequencing of operations. If the system

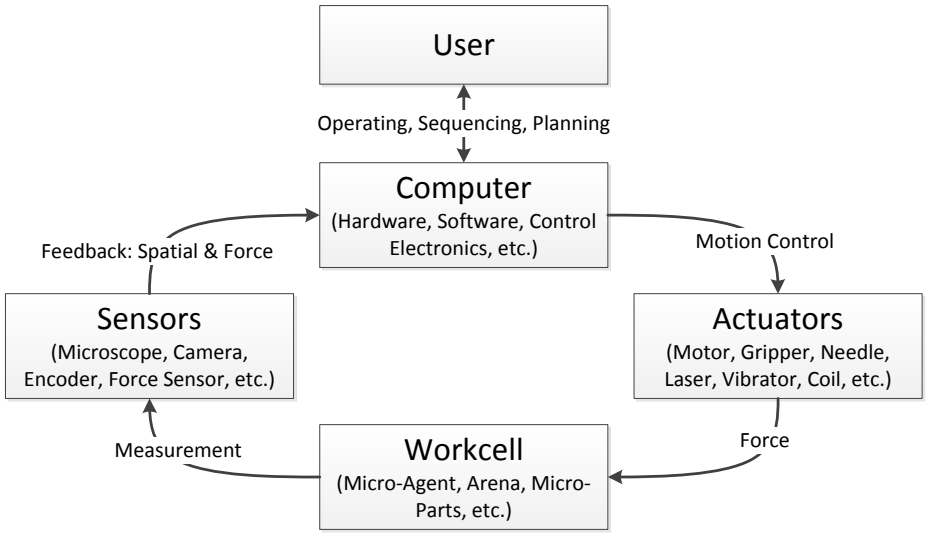

Figure 1.2. Control structure of a microrobotic system.

is semi or fully automated, on the other hand, then the user has mostly supervisory roles such as task planning and manipulator jogging for motion scripting. In this case, most of the data processing tasks are handled by software automatically. That is, the intelligence and agility of a human operator is replaced with a set of programs to control the devices. Experience has shown that successfully operating a microrobotic system can be difficult even for trained humans. Hence, it can be much more so for computer programs in certain respects. That is, developing automation programs that can accurately harness the sensory feedback, handle manipulators safely, and completely carry out an assembly or manipulation task is a very big challenge. On the other hand, it has been understood that automation is the key to the success of microrobotics and the two main issues are the lack of flexible precision robots and the lack of standardization of system design and configuration [24].

Precision of robotic systems can be understood via some classical concepts in metrology: accuracy, repeatability, and resolution [25]. These are also called precision metrics and can be used as performance measure for microrobots. For instance,

accuracy defines the maximum error in achieving a commanded (desired) point in space with the end-effector of a robot. Repeatability, on the other hand, specifies the ability to return to a particular point over repeated attempts. Resolution is the smaller of the minimum positional increment that a robot can make or sense. These terms can be visualized as shown in Figure 1.3 [26] where the dots represent the repeated attempts of a robot to bring its end-effector to a commanded position in space.

Mobility is also an important term that needs to be defined here. It refers to the number of degrees of freedom (DOF) of a mechanism. For instance, an elevator has a single degree of freedom whereas a car has two translational and one rotational degrees of freedom. This concept is particularly important for mobile micro-agents as it is difficult to decouple different DOFs of a wirelessly powered micro-agent. That is, the state-of-the-art in mobile microrobotics mostly suffers from constraints that result in mixed rotational and translational motions [27,28]. This limits the usefulness of these micro-agents as microrobotic tools to perform precise manipulation and assembly operations.

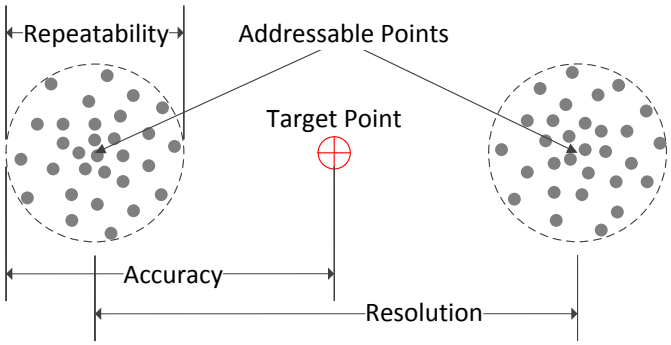

Figure 1.3. Definition of precision metrics.

1.1 Motivation for This Research

Robotic manipulation is inherently a top down serial process. That is, building blocks of a product are individually handled and assembled together in a serial way. Hence, it has to be fast enough to make practical sense for mass manufacturing purposes. As one of the ultimate goals of microrobotics is to facilitate manufacture of micro and nano scale systems, automation of microrobots is an essential step in realization of the technology. There are, however, big challenges facing automation in micro-scale [29,30]. One of them is the design and control of microrobots based on precision and mobility requirements of a given task. It is not a well addressed problem in the literature to date, although it is an important requirement for automation towards mass production.

The success of automated assembly and manipulation tasks is highly dependent on the precision of robotic positioners and/or agents employed. In turn, precision metrics for robots depend on the kinematic design, choice of actuators, sensors, and control system. In case of a microassembly operation, the precision requirements of a given task determine the necessary configuration of the microassembly cell. One of the challenges here is to adequately allocate the assembly tolerance to the degrees of freedom of the robot. At small scales, precision is the most important factor driving successful task completion but often times microscale precision requirements come with significantly higher hardware costs. Hence, during the design of precision robots, the associated precision budget have to be allocated carefully among the degrees of freedom of a robotic system to achieve favorable cost vs precision tradeoffs.

Kinematic description of a robot involves certain parameters and variables such as link lengths, joint axis vectors, and joint positions. In an ideal robot model, these are all assumed to be perfectly precise values. A practical implementation, however, requires calibrating the robot to minimize the uncertainty in the knowledge of such

parameters. Even with calibration, identification of kinematic parameters can only be done with a limited precision. Therefore, there needs to be a kinematic model that can handle these uncertainties with ease and efficiency. Deviation of the robot kinematics from its ideal model is due to many factors such as geometry errors, sensor resolution, vibration, mechanical flexing, and so on. These errors can be categorized as random (stochastic) which are uncorrectable or repeatable (deterministic) which are correctable via calibration [31,32]. The parametric uncertainties of a manipulator are due especially to the limited resolution of joint sensors and the limited precision in calibration of the mechanism [33].

Precision robot design based on task-space precision requirements have not been sufficiently addressed in the robotics literature. While there are many works discussing how to analyze errors [33–41], they do not satisfactorily address the inverse problem, i.e. how to find the bounds on those errors to guarantee a given end-effector precision. In these works, general small-angle error transformations of joints are incorporated into the forward kinematics formulation and their combined influence on the end-effector position is found. On the other hand, precision machine design literature has mostly discussed the analysis problem via the concept of *error budget* [31]. This approach also relies on first-order and small-angle approximations of errors and sampling methods to calculate their effect on the tools position. Studies on tolerance allocation in mechanisms address the problem from the geometry design perspective [42]. Among more recent studies, there is a growing interest in methods based on interval analysis [43, 44]. However, these works do not take into account robot specific factors such as joint sensor errors. Microrobotics research, on the other hand, has not yet come to the point of creating guidelines for design based on precision although several custom-designed microassembly systems with architectural

similarities have appeared [14, 45, 46]. Therefore, there is a need for an established methodology that can allow precision analysis as well as precision design.

In the case of a micro-agent system, the specifications of a mobile micromanipulation task reflect on the required design of the micro-agent. However, the vision of microrobotics with untethered manipulation agents whose dimensions range from millimeters to micrometers faces a key limiting factor: Delivering power and control wirelessly. In order to overcome this bottleneck, the concept of remote power delivery has recently emerged [19, 30]. The main challenge in this case is to map the design and control parameters to the desired degrees of freedom of the micro-agent such that the required mobility and precision can be obtained. Over the last several years, approaches to this problem has concentrated around a very few number of methods such as electrostatic [28] and magnetic [47–50] actuation. In these methods, the power source is global hence only one micro-agent can be controlled in general and also the energy density of the power source may not be sufficient for demanding tasks such as pushing and moving objects for microassembly. Recently, structural differences or additional clamping mechanisms have been introduced to accommodate multiple micro-agents inside the same arena [51–53]. However, most of the current designs lack the capability to address individual degrees of freedom of the micro-agent but rather generate coupled motions in the form of translation, rotation, and tumbling. Therefore, analysis of mobility and motion precision is still to be addressed as a research problem in micro-agent systems.

1.2 Methodology and Contributions

The basic methodology in this thesis is to approach the microrobot design and control problem from the viewpoint of precision-based performance metrics. Considering that the ultimate goal of using robots to do micro-scale operations is to achieve

a certain level of precision, we consider it essential to incorporate precision metrics into the design phase. The level of precision of a microrobotic system is adversely affected by the increasing relative magnitudes of errors and uncertainties with respect to operational precision towards smaller scales. Therefore, analysis of errors and uncertainties plays an important role in the characterization and evaluation of the system.

Often times, microrobotic operations require configuring custom manipulators from individual axes due to the special requirements of the task [14, 45, 46]. This introduces the problem of properly choosing the right equipment and the right configuration for a given set of assembly and manipulation tasks. Making design choices at this stage requires a thorough analysis of the aimed precision level and the capabilities of the alternatives in those terms.

In this thesis, we develop a generic formulation of robot kinematics using interval variables and parameters and employ interval analysis to predict the effect of errors as they propagate to the manipulator end-effector. We use intervals as a mathematical construct to model errors and uncertainties in the analytical description of robotic manipulators. Interval analysis is a mathematical tool for computation of rigorous bounds on solutions to ideal model equations when the input arguments of the model are represented as intervals instead of point values [54]. It extends the model equations to the interval domain and allows for analytical and computational handling of uncertain data without having to assume a distribution for it or to sample it. Thus, it helps avoid the complex mathematical formulations involving distribution functions. We show that this method offers rigorous precision bounds in terms of interval numbers which are much easier to work with than sets of points as in the case of error sampling methods. We use this formalism to analyze the precision of a microrobotic system based on the error and uncertainty specifications of its individual

components. Then, we use this formalism for the inverse kinematics formulation of manipulators such that we can determine the allowable errors and uncertainties in the building blocks of a manipulator based on given end-effector precision metrics. Therefore, we can use this method for both precision analysis and precision design. As emphasized in Figure 1.4, this analysis can aid not only microrobot design but also configuration, optimization, performance prediction, and automation. Interval analysis constitutes a major part of the mathematical foundation for precision evaluation of microrobots. The validity of the proposed methodology is tested using simulation studies as well as experiments.

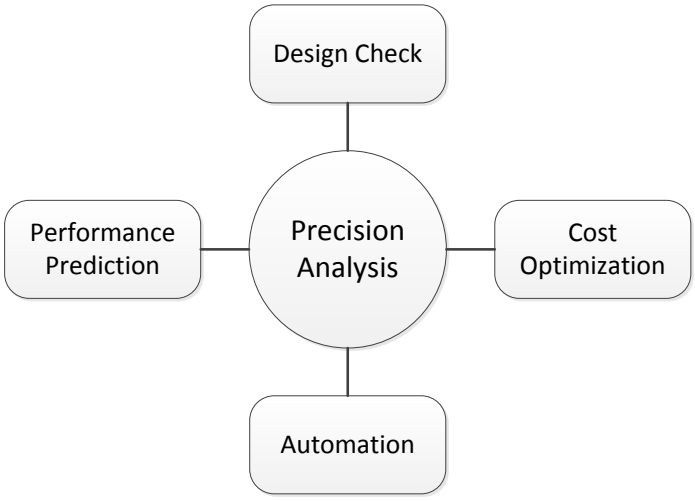

Figure 1.4. Precision analysis as a tool for microrobot design and automation.

Also, the promises and challenges of wirelessly controlled mobile micro-agents as part of microrobotic systems is discussed. In the future of this line of research, there is a need for tight integration of various functionalities such as communication, sensing, and actuation as they have to take place simultaneously with the provision of remote power. The current state-of-the-art in remote powered micro-agents is limited only to actuation functionality [55]. The most important consideration in this case

is to be able to control the motion of the micro-agent in a desired way with desired precision. This requires appropriate couplings between the power source and the actuation schemes of the agent such that different degrees of freedom of the agent can be effectively addressed using the degrees of freedom of the control signal. The degrees of freedom of a signal are defined here to be the tunable spatio-temporal signal parameters such as frequency, amplitude, duty cycle, position, gradient, and so on, that can possibly couple with distinct actuator responses. Achieving the desired device operation with available controls in the driving signal is a challenge that requires redesign of current micro-actuators and invention of new ones. Also, shaping of the control signal via its spatio-temporal parameters to address certain actuator response is a combined effort of accordingly designing the microdevice and selecting the device materials. In this respect, we propose a new micro-agent design that can be powered and controlled by a pulsed laser source and achieve three degrees of mobility. Using laser as the power source allows for delivering very high density energy and focusing it on a particular spatial location so that multiple micro-agents can be independently addressed. Also, the pulse frequency can be used to excite different responses of a micro-agent, providing a means to address its multiple degrees of freedom.

The main contributions of the dissertation can be summarized as follows:

1. We present a new method to model and analyze uncertainties in a robotic system. We extend the products of exponentials (POE) formulation of robot kinematics to intervals for the first time [56, 57]. We define interval functions that can take the uncertain POE parameters of a manipulator as input arguments and calculate the forward kinematics map to produce an interval result, an interval homogeneous transformation matrix, that represents the deviation of the end-effector from its ideal pose. Interval functions have to obey the theorems of interval analysis in order to guarantee bounding of all possible solutions.

We show via several theorem-proof pairs, simulations, and experiments that our interval extension functions are indeed guarenteed. This formulation helps understand the effects of mechanical and sensing errors on the positioning precision of a micromanipulator. Therefore, it can be used as a tool for performance evaluation and design check. It can also be used in automating microassembly processes to determine which of the three control modes, open-loop, calibrated, closed-loop, is most suitable based on the required operational precision. The concept of precision analysis and design is illustrated in Fig. 1.5 with a simple 2-DOF manipulator with uncertain kinematic parameters. In this illustration, precision analysis amounts to the mapping of parameter-space intervals to the task-space intervals and bounding them using the interval forward kinematics map. The obtained bounds quantify how precise the end-effector positioning is.

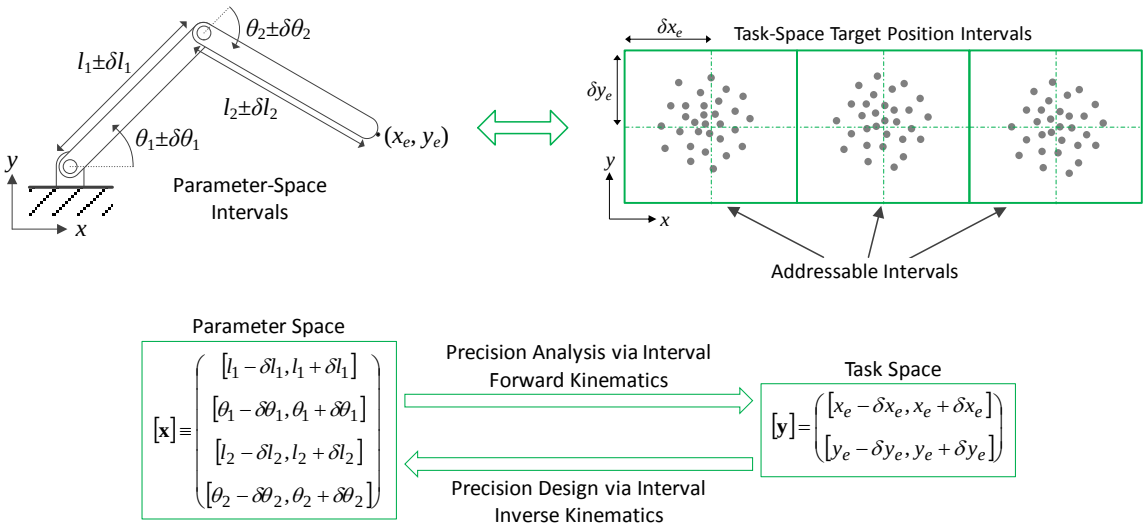

Figure 1.5. An illustration of the concept of precision analysis and design.

2. We develop a new method of precision design of microrobots by applying our interval POE formulation to the inverse kinematics problem [58,59]. In this case, as illustrated in Fig. 1.5, the input argument of the problem is the desired set of end-effector poses in task-space represented in general with an interval homogeneous transformation matrix. We use a set inversion algorithm together with our interval extensions of the kinematics formulation to effectively search the kinematic parameter space and find the set of solutions to the given end-effector pose intervals. This solution provides a measure of the maximum allowable error in each parameter of the kinematic model such as joint sensor, joint axis location, and mechanism tolerances such that the given end-effector precision is guaranteed . Hence, custom design or configuration of a microrobotic system for a particular precision requirement can be done with the help of this method. In particular, the solution can be used to determine the resolution required in each joint sensor and the maximum allowable tolerance and misalignment in different members of the mechanical structure.
3. We present a new power delivery and motion control idea for micro-agent systems that require high energy density without global field constraints [60, 61]. The idea is that focused laser can be used as a very high density energy source to wirelessly delivery power to thermally actuated micro-agents. We create novel mobile micro-agent designs to be powered and controlled wirelessly using a pulsed laser source. We also develop a photo-thermo-mechanical model for the mathematical analysis of these designs. As illustrated in Fig. 1.6, the mathematical model allows performing the mobility analysis that reveals the task-space performance of the system. Conversely, achieving certain task-space behaviors requires designing the mechanical structure and actuators of the micro-agent as well as driving the control parameters of the system accordingly.

We show that temporal variables such as frequency of a pulsed laser source can be used to address different actuation modalities of a micro-agent so that desired degrees of freedom can be obtained. Also, multiple micro-agents can be independently controlled using multiple sources or scanning a single source at a fast rate across multiple locations. This eliminates the limitations of global magnetic and electrostatic field methods.

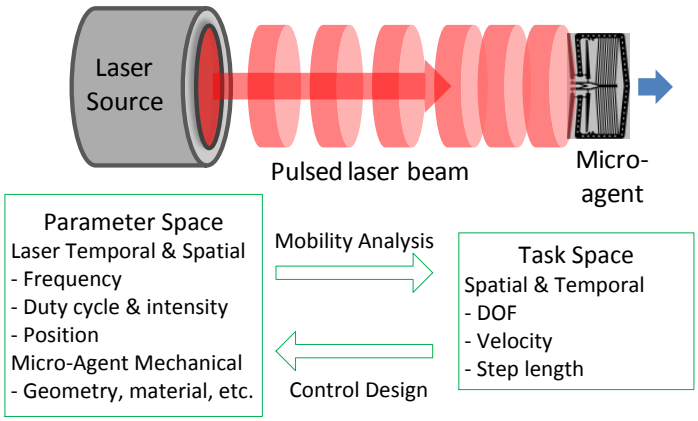

Figure 1.6. An illustration of the concept of mobility analysis and control.

1.3 Thesis Organization

Chapter 2 provides background information about the research in the field of microrobotics. Chapter 3 covers the essential concepts of Interval Analysis that is made much use of in the rest of the dissertation. We develop our kinematic analysis method in Chapter 4 using the POE formulation. We present several theorems and their proofs to establish the interval-based forward kinematics map. In Chapter 5, we validate our method via simulation and experimental results. Also, we discuss how the proposed precision analysis method can be applied to practical micro-assembly problems. We then discuss the microrobot design problem in Chapter 6 by apply-

ing our method to the inverse kinematics problem. We offer simulation examples to show how to design a microrobot based on given precision requirements. In Chapter 7, we focus on microrobotic systems with mobile micro-agents. We present our micro-agent design ideas and a methodology to control their mobility using a pulsed laser source. We analyze the mobility of a laser-driven micro-agent with respect to its control parameters. We present simulation and experimental results on a laser-powered micro-actuator and a 3-DOF micro-agent. We also discuss two alternative power delivery and control methods based on vibration and magnetic actuation. In Chapter 8, we introduce our fabrication and microassembly techniques used to perform microrobotic tasks. We conclude the thesis in Chapter 9 with a discussion on future work. Appendices provide some details about the simulations, experiments, and experimental setups used. Finally, the references are listed at the end of this thesis.

CHAPTER 2

BACKGROUND IN MICROROBOTICS

Over the last two decades, several research groups around the world have developed robotic systems that can perform 3-dimensional micro and nano scale assembly and manipulation (Fig. 2.1). The group at the Institute of Robotics and Intelligent Systems, Zurich, developed a microassembly unit that has 6-DOFs split as a θXYZ stage and a 2-DOF manipulator [14]. The system can handle parts with dimensions from 5 to 800 μm. At University of Texas, Arlington, Das et al. developed μ^3 a microassembly system with 20-DOFs split into two manipulators and a sample holding stage [46]. Microrobotics was also applied to microsytems packaging by Popa et. al [62]. Manipulation in nano-scale inside SEM was demonstrated by Fatikow [22]. They used cm-scale mobile robots with 3-DOF planar mobility and 2-DOF on-board manipulator to do handling under the SEM column with real-time image feedback from the electron sensor. Several other research groups around the world working in microrobotics field are R. S. Fearing at University of California Berkeley, M. Sitti, A Rizzi, and R. Hollis at Carnegi Mellon University, W. L. Cleghorn and J. K. Mills at University of Toronto, F. Lutz and M. Gauthier at University of Franche Comte, S. Martel at Ecole Polytechnique de Montreal, T. Fukuda and F. Arai at University of Nagoya. After such successful realizations of manually operated or semi-automated microrobotic systems in the last decade, now the focus is on advancing the technology towards full automation and high yield [63–66].

Microrobots can be characterized as systems that have multi-scale operation and precision. On one hand, the system needs to have a motion range in the order of

centimeters (10^{-2} m). On the other hand, it also needs to have a motion resolution of a micrometer (10^{-6} m) or less. This is 4 orders of magnitude difference and poses rather different challenges in system design than that in meso-scale robotics [67]. In order to bridge the scale gap, microrobotic systems most often employ long-range coarse positioning actuators together with short-range fine positioning actuators.

As part sizes decrease below 1mm, handling components using robotic techniques becomes markedly more difficult. During the last two decades, research in microrobotics shed light on important factors that drive the operational yield in the micro and nano realms, in particular: surface effects [17]; microgripper design [68]; manipulator precision and choice of control methods [62] have been investigated. It has been observed that choosing successful control and planning strategies for microrobots is highly dependent on the precision of the actuation systems employed [66]. Enabling automation in micro-scale operations require either very precise robots so that tasks can be performed mostly in open-loop control or very precise feedback sensors so that closed-loop control routines can be used. Since provision of either alternative is an extreme solution in terms of cost, hybrid solutions have been developed to take advantage of both approaches and optimize cost and complexity [66, 67].

A review of microrobotics in terms of precision motion control can be done under two categories. One is the category of microassembly robots whose end effectors are micro-grippers, micro-tweezers, or other kinds of micromanipulators. The second category is the microrobotic systems with wirelessly powered mobile micro-agents which serve as the end effector of the system. In the first case, precision and mobility requirements can be defined in a more classical way. Hence, from an automation perspective, the focus is on successfully sequencing and planning operations via open or closed loop control schemes [66, 69–71]. In the case of micro-agent systems, on the other hand, the micro-agent design and fabrication technology is still its infancy

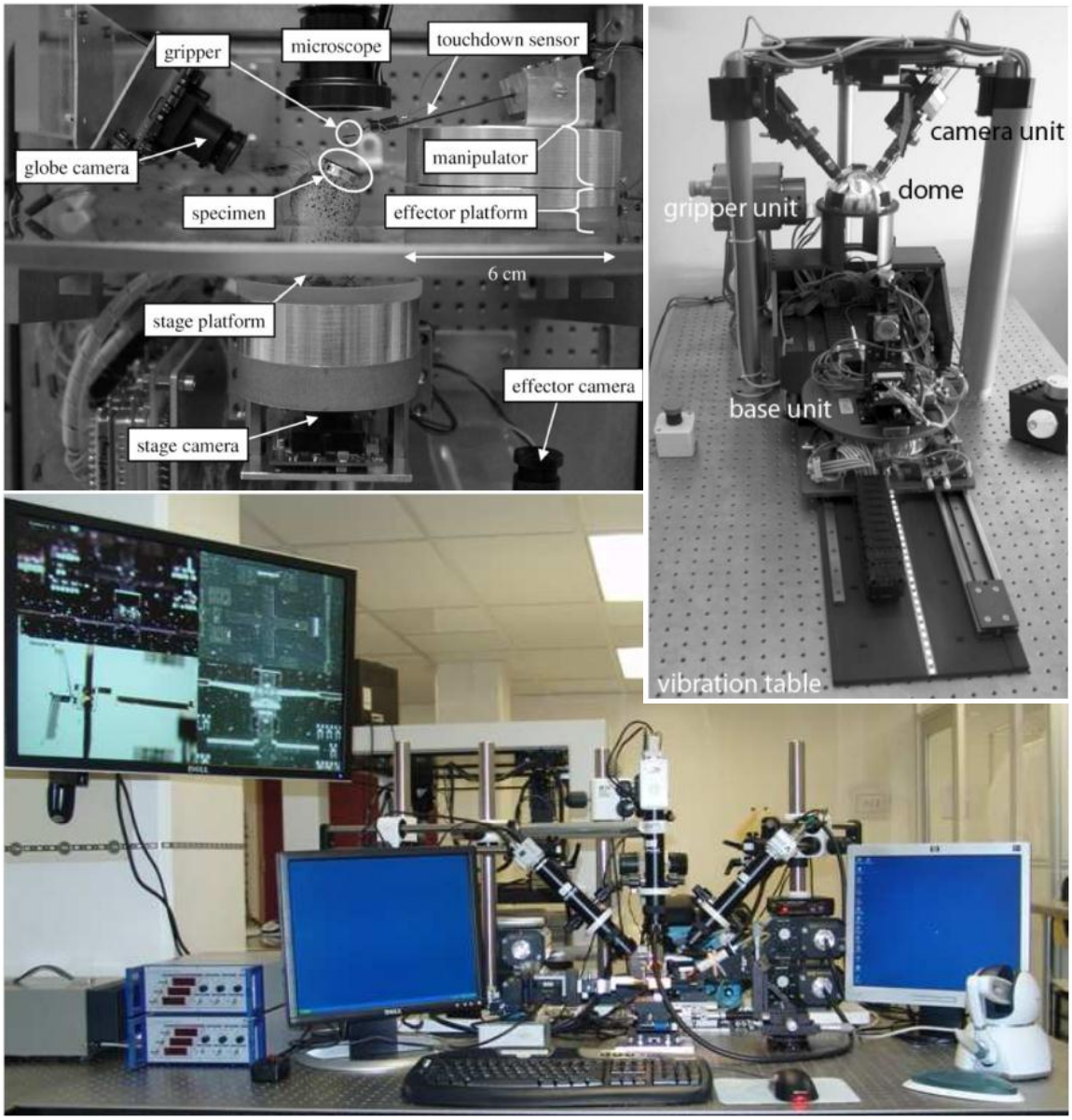

Figure 2.1. Micro/nano-robotic systems developed by [22] (upper left), [14] (upper right), [46] (lower).

towards making power delivery and motion control possible through wireless means [15,19]. Thus, analyzing precision for automating the manipulation processes has not been addressed so far.

2.1 Microassembly Robots: Precision Analysis

The success of automated assembly by robotic manipulators is highly dependent on the precision of the positioning mechanisms employed. The importance of precision becomes more prominent when the desired operational accuracy is in micro/nano scale. Most of the parametric uncertainties that are negligible in conventional robotics become the predominant error sources in micro/nano applications. With the emergence of micro-manufacturing technology in the last decade, there is a growing demand for methods that can help system designers analyze the effects of imprecision on the performance of a manipulator [12].

In most cases, micro-assembly operations require building a custom manipulator from individual axes due to the special requirements of the tasks [14, 45, 46]. This introduces the problem of properly choosing the right equipment and the right configuration for a given set of assembly tasks. In this respect, quantitative analysis of mechanism designs, choice of actuators, sensors, and overall control system is an important topic.

In order to address the consequences of errors in a robotic system, an understanding of their sources and nature is essential. There are many sources of errors involved in the operation of a manipulator such as mechanical imprecision, sensing resolution, control performance, vibration, and structural deformation [32]. Kinematic errors fall under the category of mechanical and sensing factors and basically account for the discrepancy between the actual system and its ideal model. The uncertainties in the knowledge of kinematic parameters such as link lengths, axis vectors, angles, and positions become significant when the required precision is comparable to the amount of errors. Then, these uncertainties have to be taken into account and the magnitudes of the errors they cause at the end-effector have to be identified.

The importance of precision analysis has been insufficiently addressed in the field of automated micro-assembly although it is a decisive consideration for the success of this technology. Das and Popa [72] considers the overall effect of individual link/joint uncertainties in a modular robotic chain for several different configurations of the same components. The uncertainties were assumed to be normally distributed and a Monte Carlo sampling analysis was carried out to make robot kinematic design choices for peg-in-hole microassembly tasks. In [56], we considered the overall effect of individual link/joint uncertainties in a serial robotic chain.

2.1.1 *Error Analysis in Robotics*

In late 80's and early 90's, modeling errors in robot kinematics was a popular topic. The effect of joint resolution errors on the end-effector position was discussed in [33] using the manipulator Jacobian with small angle approximation of error displacements. Generalized kinematic errors were modeled as small angle transformations in [37] and analyzed via a modified Denavit-Hartenberg (D-H) notation that allows arbitrary assignment of coordinate frame origins. In [39], the geometric uncertainties were modeled as small-angle transformations that have normally distributed parameters. Even for a 3-axis linear machine, the analytical formulation grows rather complicated, limiting the applicability of the method to relatively simple kinematic designs. Similarly, [40,41,73] analyze the errors via simplifying small-angle and reduced-order approximations. These works are limited in terms of the capability to provide guaranteed bounds on the task-space uncertainty of the robot end-effector because they have approximate formulations and rely on sampling of errors.

Modeling and analysis of errors in multi-axis machines has also been studied in the area of precision machine design due to its impact on product quality. Given the desired tooltip accuracy, the allowable amount of error in a machine's components

is referred to as the error budget [31]. Formulation of the error budget starts with determining the kinematic model of the mechanism and mapping errors through this model. The resulting tooltip errors provide a measure of the relative importance of various error sources as well as bounds for accuracy. This approach relies on first order and small angle approximations of errors and work reasonably well for simple kinematic designs for which accuracy bounds can be related to error bounds in closed forms. However, for more complex configurations the above method requires computational evaluation of accuracy bounds based on sampling of errors.

In precision engineering, one way of classifying errors and uncertainties is based on their sources [31, 32]:

- Mechanical: Errors related to the geometry of the manipulator assembly, tool and part tolerances, joint clearances, and backlash.
- Sensing: Errors due to the limited resolution of joint sensors, cameras, and other sensing equipment.
- Control: Errors involved in the dynamic and static behavior of the manipulator controller.
- Vibration: Errors due to the ambient vibration and the vibration induced by the motion of the manipulator.
- Flexure: Errors created by deformation of mechanisms due to loading or changes in temperature.

Apart from the sources of errors, their uncertainty nature is also important. In that respect, there are two types of errors: repeatable (deterministic) and random (stochastic). Given the same conditions and configuration, repeatable errors result in the same discrepancy between the desired and actual operation of the manipulator tool. Random errors, on the other hand, manifest themselves unpredictably and can be modeled with random distributions.

Figure 2.2 illustrates two examples of errors in a manipulator joint, namely Abbe error and joint error. Abbe error has a geometrical or mechanical source that results in a difference between the designed and actual axis of the joint which in turn causes a deviation at the end of the link that is amplified by the length of the link. This error is repeatable in nature and can be compensated for. Joint error, on the other hand, is due to the finite resolution of the joint angle sensing instrument, commonly joint encoder, and it is random. While there are many other error sources even in a single axis, what is important is to determine the major ones such that the dominant factors causing the apparent imprecision in the overall robot operation can be detected. In precision engineering terminology, this is called error mapping and sensitivity analysis [31].

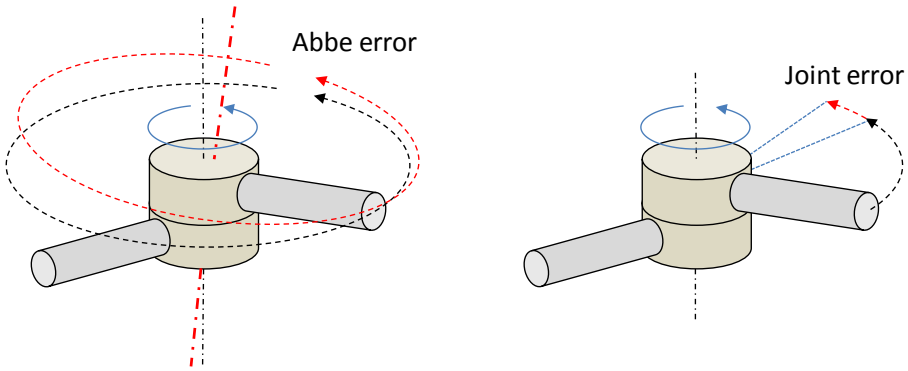

Figure 2.2. Illustration of two error types: Abbe error (on the left) and joint angle error (on the right).

2.1.2 *Use of Intervals in Mechanism Design and Tolerance Analysis*

Recent studies address the mechanism design and tolerance allocation problems by using intervals to find guaranteed solutions.

In [43], a tolerance allocation method is presented based on modeling the D-H parameters of a manipulator with intervals to account for the uncertainty in manufacturing and assembly of the manipulator mechanism. Optimal design of joint tolerances was found using an optimization tool of MATLAB to satisfy the cost and precision requirements. Two of the D-H parameters, offset distance d_i and angle about common normal α_i, of the 4-DOF SCARA robot and the 6-DOF Stanford arm were modeled using intervals such that a total of 7 and 11 parameters, respectively, were designated as optimization design variables. The cost of mechanism precision was described with a reciprocal polynomial and exponential cost function, respectively. Then, the interval matrix arithmetic operations were used to carry out the forward kinematics transformations. In the SCARA robot case, the objective function of the optimization problem was set to be the minimization of the manufacturing cost subject to criteria that bounds the range of uncertainty in joint parameters and end-effector orientation. For the Stanford arm, the objective function of the optimization problem was set to be the minimization of the volumetric end-effector error subject to criteria that bounds the range of uncertainty in joint parameters, end-effector orientation, and the total cost of precision of d_i. The optimization problem was computationally solved using MATLAB and numerical results were presented, showing the optimal values of the joint parameters as the allowable orientation error or the cost were changed. In the results presented, it is counter-intuitive to see that the optimal value of the objective function, i.e. end-effector error, decreases with increasing allowed orientation error. As the orientation tolerance is increased, in other words, the optimization would be expected to generate a less precise design due to the cost constraint and a higher end-effector error. However, neither in the paper nor in the thesis there is any explanation or verification of the calculated optimal results. Another point is that the choice of D-H parameters representation is not

desirable from a modeling perspective because it can only capture a limited number of error factors in the model. As suggested by Mooring et al. [32], D-H parameters require modifications to satisfy certain requirements to be a good model for error representation.

Reference [74] presents an optimization method for tolerance allocation in manufacturing processes. It uses intervals to represent tolerance parameters and applies the response surface methodology to obtain tolerance surfaces for process responses expressed in terms of interval parameters. A metal extrusion problem is analyzed to present results obtained via this method and via the ordinary least squares (OLS) estimation technique. It can be seen in these results that the response model obtained via OLS is contained in the solution set of the interval-based model. However, the paper lacks the explanation of how the results support the concluding remark stating that the proposed method allows more production and acceptance in the manufacturing process.

In [75], a feature-based approach to tolerance analysis is presented for mechanical assemblies with geometrical and dimensional tolerances. Intervals were used to mathematically describe the uncertainty of dimensions and geometrical form of features. The tolerance zones of these uncertain geometric entities were modeled using interval vectors representing small translational and rotational degrees of freedom (SDOF). A class of tolerance zones was defined in terms of interval SDOF vectors to account for all common types of 2D and 3D tolerances in general assemblies. Then, the tolerances of individual features of a part are propagated towards the parts target feature and ultimately to the global target feature via geometrical transformations represented with rotation matrices and translation vectors.

Another reference in [76] presents a method to find the range of parameter values for a 6-DOF parallel robot such that certain workspace and accuracy requirements

are satisfied. A linear approximation for the inverse error model of the robot is evaluated with input interval arguments such as desired workspace and allowed parameter ranges to find the corresponding range of joint displacement values. Then, the resulting joint displacement intervals are compared with their allowable values. If the comparison is affirmative, then the input intervals are regarded as feasible workspace and parameter ranges. Otherwise, they are either discarded if there is no overlap between allowable and calculated joint intervals or bisected to repeat the process until every input interval either has a width smaller than a threshold or is classified as feasible or not. In this way, the feasible range of values for the parameters of the robot is determined. Then, the optimal values within the feasible range are found by either sampling or introducing additional requirements to further carry out the process.

Interval analysis was also used as a computational tool to solve for the forward kinematics of a parallel manipulator in a given search space represented by interval variables [77], [78]. Another application of interval computations was to search for geometric design solutions for an RRR manipulator based on five given task-space positions [79].

2.2 Mobile Micro-Agent Systems: Mobility Analysis

Microrobotic agents that are built using monolithic fabrication, micromachining, and microassembly systems are envisaged to be useful in many future applications such as biological cell manipulation and in vivo exploration of human body for medical diagnosis and treatment [30], automated micro/nano handling [69], and nanomanufacturing inside SEM [80]. Recognizing the promise of this research, the National Institute of Standards and Technology (NIST) started organizing microrobotics challenges in 2007 [55]. The objective is to design devices of size in fractions

of a millimeter such that they can operate without tethers. In previous years, there has been a popular trend towards employing electromagnetic actuation techniques as in Fig. 2.3. However, there are also some demonstrations of alternative locomotion mechanisms and micro-agent designs such as the optically-guided micro-bubble in liquid environments [81].

One of the earliest works in mobile micro-agent design is [28] which discusses a microrobot of dimensions 250x60x10 μm and uses an untethered scratch drive actuator that is powered through a capacitive coupling with the underlying substrate. The robot has a forward speed of 200 $\mu m/s$ and turning radii of 176 μm. Another work, [27], presents a 250x130x100 μm magnetic microrobot that can operate under the excitation of an external magnetic field and move at 2.8mm/s. One of the most successful designs is a resonant magnetic actuator composed of two paramagnetic bodies, a spring system, and a metal frame. It can move forward, backward, and turn in place with a forward speed up to 12.5mm/s [82].

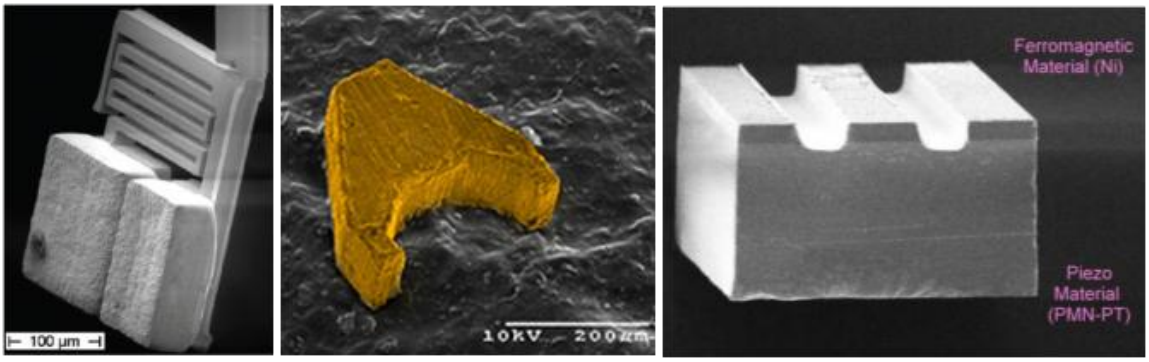

Figure 2.3. Magnetic resonant [49] (left); magnetic [27] (middle); magnetic-piezoelectric [50] (right) microrobots.

Both electrostatic and electromagnetic field methods are challenged by the fact that the field is global and it cannot differentiate between individual robots unless

some properties of the field couple with corresponding differences in microrobot design [52]. On the other hand, as a directed and focused source of energy, pulsed laser is a promising alternative. The microactuators suitable for this type of power delivery are thermal microactuators. There have been studies on heating up thermal actuators through unconventional sources such as laser. For instance in [83], a 10 mW laser was used to heat a 1mm long bimorph actuator and a deflection of 11.8 μm was obtained. Similarly, experiments with a chevron type actuator were carried out in [84] and a deflection of 2 μm for a 400 μm actuator under 18mW of laser power was reported. Elbuken et al. used a laser powered microgripper with bent-beam actuated fingers for micromanipulation [85]. With 50mW incident laser power, deflections up to 50 μm were obtained with two 1000 μm fingers. The use of laser in providing power to actuators of a locomotive microdevice was reported in [86] where a three-legged crawler of size 30m made of thin metal film bimorphs was described. A pulsed laser beam of 3 μm spot size and power up to 20mW is focused on a leg to generate impact drive motion with a speed up to 100 μm/s.

There is also a major interest in controlling microorganisms using microrobotic systems and integrating fabricated microstructures with motile microorganisms [87–90]. The microorganisms are driven by external stimuli such as UV light [91], magnetic fields [87], electric fields [89], or chemical stimuli [90]. While this approach is limited in terms of 3D micromanufacturing purposes, there is a great potential for biomedical applications such as targeted drug delivery and cell manipulation.

We discuss the promises and challenges of using laser as a source of energy and means of control for untethered microdevices in [60]. Achieving the desired device operation with available controls in the laser signal is a challenge that requires redesign of current microactuators and invention of new ones. In addition, for multiple target spots on a device, the laser beam can be multiplexed or separate lasers

can be used simultaneously. Shaping of the control signal based on such variables of the laser as output power, pulse width, and beam spot is a combined effort of accordingly designing the microdevice and selecting the device materials. We then proposed in [61] using a single laser beam focused onto the whole body of the robot. It is shown through simulations that an appropriate selection of these parameters along with a corresponding mechanical design can generate appropriate "stick and slip" motions resulting in 3-DOF (planar) operation for the microrobot. The paper proposes a microrobot design with thermal actuators and details its photothermal model and lumped thermal analysis. The thermal analysis is then coupled with a basic stick-slip model to predict the microrobots controllability. Based on the simulation results, we anticipate the microrobot with the thickness of a few microns and the width of several hundred microns can achieve speeds in excess of a few mm/second, comparable with more conventional electrostatically and electromagnetically actuated microrobots. Initial experiments on chevron actuators also indicate that pulsed laser can effectively drive stick-slip microrobots.

CHAPTER 3

BACKGROUND IN INTERVAL ANALYSIS

Interval analysis is a mathematical tool for computation of rigorous bounds on solutions to ideal model equations when the input arguments of the model are represented as intervals instead of point values. It extends the model equations to the interval domain and allows for analytical handling of uncertain data without having to assume a distribution for it or sampling it. It also helps avoid the complex mathematical formulations involving distribution functions [54, 92].

3.1 Intervals and Interval Operations

Intervals are denoted with a closed set of values such as

$$[a, b] = \{x \in \mathbb{R} : a \leq x \leq b\} \tag{3.1}$$

An *interval variable* is defined with two bounding point values called as the left and right endpoints:

$$[x] = [\underline{x}, \overline{x}],\ \underline{x} : \text{left endpoint}, \overline{x} : \text{right endpoint} \tag{3.2}$$

In this thesis, interval variables will be denoted by square bracketed letters (e.g. $[x]$). Also, 'point' and 'real' terms will be used interchangeably for point-valued real numbers as in [54, 92].

Basic arithmetic operations are defined for intervals with a general form as in (3.3).

$$[x] * [y] = \{x * y : x \in [x],\ y \in [y]\} \tag{3.3}$$

where * denotes addition, subtraction, multiplication, or division. This concept can be extended to definition of functions such as

$$f([x]) = \{f(x) : x \in [x]\} \tag{3.4}$$

The definitions in (3.3) and (3.4) can be interpreted as a *computational* description of operations on intervals.

What is more interesting in interval analysis is the *endpoint formulas* for operations. Given two intervals $[x]$ and $[y]$, for instance, their multiplication is defined as

$$[x] \cdot [y] = [\min\{S\}, \max\{S\}],\ S = \{\underline{x}\underline{y}, \underline{x}\overline{y}, \overline{x}\underline{y}, \overline{x}\overline{y}\} \tag{3.5}$$

Similarly, given a real function $f(x)$, the range of values it takes as the argument x varies through an interval $[x]$ can be described using the endpoints of $[x]$. For instance, let $f(x) = x^2$ be the real function to be defined for interval argument. One of the choices would be

$$[f_1]([x]) = [x] \cdot [x] \tag{3.6}$$

where $[f_1]$ represents an interval equivalent of f. For $[x] = [-1, 2]$, for example, $[f_1]([x])$ above produces a result of $[-2, 4]$. On the other hand, if (3.4) is carried out for the same $[x]$, the result would be $[1, 4]$, a smaller interval enclosed by $[-2, 4]$. Then, the interval function in (3.6) is said to *overestimate* the result due to *interval dependency*. Hence, one of the objectives of defining an interval function is to find the solution that is as close as possible to the solution in (3.4) which is called the *set*

image. For this example, a better interval function definition for $f(x) = x^2$ is in (3.7) which results in the exact boundary as the set image.

$$[f_2]([x]) = \begin{cases} [\underline{x}^2, \overline{x}^2], & 0 \leq \underline{x} \leq \overline{x} \\ [\overline{x}^2, \underline{x}^2], & \underline{x} \leq \overline{x} \leq 0 \\ [0, \max\{\underline{x}^2, \overline{x}^2\}], & \underline{x} \leq 0 \leq \overline{x} \end{cases} \tag{3.7}$$

Analytical expressions as in (3.7) are available for many other basic arithmetic operations and functions with intervals. These are called *interval extenstions* of real operations and functions. For more information on basics of intervals, the reader is referred to the introductory text by Moore et al. [54].

3.2 Error and Uncertainty Modeling with Intervals

The concept of intervals can be applied to any uncertain quantity or source of error that appears in the description of a system. For example, given a random variable x that is assumed to have a Gaussian distribution of (μ, σ), the corresponding interval variable can be written as

$$[x] = \mu + 3\sigma[-1, +1] = [\mu - 3\sigma, \mu + 3\sigma] \tag{3.8}$$

such that it represents 99.7% of the random distribution. There are many examples of such uncertainties in robotic assembly systems such as link lengths, joint orientations, part dimensions, and other geometrical errors. However, the precise nature of their distributions is rarely known. If the uncertainty has definable bounds, on the other hand, those bounds can directly be used in the definition of the corresponding interval variable.

3.3 Fundamentals of Interval Analysis

Given n intervals $[x_1], \ldots, [x_n]$ and a real valued function f of n variables $x_1, \ldots, x_n$, the mapping defined as

$$\begin{aligned} &f([x_1], \ldots, [x_n]) \triangleq \\ &\{f(x_1, \ldots, x_n) : x_1 \in [x_1], \ldots, x_n \in [x_n]\} \end{aligned} \tag{3.9}$$

gives the precise values of f as the inputs vary through the given intervals. That is, $f([x_1], \ldots, [x_n])$ is the image of the set $\{[x_1], \ldots, [x_n]\}$ under mapping f. In general, set image can only be constructed partially by computational sampling methods. Hence, the purpose of finding an interval extension function, $[f]$, for f is to bound the set image in a compact and guaranteed manner. By definition, an interval extension function must satisfy

$$f(x_1, \ldots, x_n) = [f](x_1, \ldots, x_n) \tag{3.10}$$

An important property for some of the interval functions is *inclusion isotonicity* [54, p. 46]. An interval function is inclusion isotonic if

$$[x_i] \subseteq [y_i] \Rightarrow [f]([x_1], \ldots, [x_n]) \subseteq [f]([y_1], \ldots, [y_n]) \tag{3.11}$$

for all $i = 1, \ldots, n$. Another definition to be covered here is as follows: An interval function is called *rational* if it is computed by a finite sequence of interval arithmetic operations. A rational interval function can arise as a natural extension of a real-valued function. For instance, given a function $f(x_1, x_2) = (x_1^2 + c)x_2$, its natural interval extension is $[f]([x_1], [x_2]) = ([x_1]^2 + [c])[x_2]$ where c is a constant term.

The following lemma and theorem form the basis of interval analysis and our mathematical elaboration that follows.

Lemma 1. *All rational interval functions are inclusion isotonic [54, p. 47].*

Theorem 1. *Fundamental Theorem of Interval Analysis [54, p. 47]: If* $[f]$ *is an inclusion isotonic interval extension of* f*, then*

$$f([x_1], \ldots, [x_n]) \subseteq [f]([x_1], \ldots, [x_n]) \tag{3.12}$$

This theorem allows one to find using a finite number of evaluations the bounds on the range of values a real function assumes as its arguments vary over given intervals. It guarantees that the interval value of $[f]([x_1], \ldots, [x_n])$ encloses all possible values of $f([x_1], \ldots, [x_n])$.

The concepts of set image and interval extension are illustrated in Fig. 3.1 for a real function, f, with two arguments. It should be noted that the mapping $f([x_1], [x_2])$ is a sampling process whereas $[f]([x_1], [x_2])$ is basically an analytical evaluation of an interval function with two interval arguments.

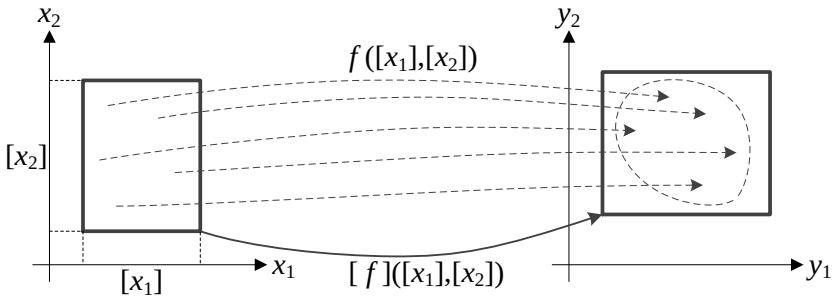

Figure 3.1. Set image and interval extension of a function.

3.4 Computational Interval Analysis

Interval analysis comes with computational methods that allow one to bound the set image as closely as desired. The process of obtaining increasingly tighter bounds on the result is called *refinement* [54, p. 53]. There are many computational

methods that can be used in the process of refinement such as the *centered form, mean-value form, slope form, monotonicity test form,* and *Skelboe's algorithm* [54, pp. 63-83].

3.4.1 *Bounds Refinement*

The refinement process, as illustrated in Fig. 3.2, can be described as follows: Consider an interval extension $[f]$ of a real function f over the interval $[x] = ([x_1], [x_2])$. The subdivisions of $[x]$ are given by

$$[x_{i,j}] = [\underline{x}_i + (j-1)\frac{w([x_i])}{k}, \underline{x}_i + j\frac{w([x_i])}{k}] \tag{3.13}$$

where $w([x_i]) = \overline{x}_i - \underline{x}_i$ is the width of the interval $[x_i]$ and $k \in \mathbb{N}$. For the particular case in Fig. 3.2, $k = 2$ and $j = 1, 2$. Then, the refined solution is found by the union of all $[f]([x_{i,j}])$:

$$[f_k]([x]) = [f]([x_{1,1}], [x_{2,1}]) \cup [f]([x_{1,1}], [x_{2,2}]) \ldots \cup [f]([x_{1,k}], [x_{2,k}]) \tag{3.14}$$

$[f_k]([x])$ provides an overestimation that is an order of k less than what $[f]([x])$ produces. Given a finite computational resolution, therefore, the refinement method can be used to make $[f_k]([x])$ arbitrarily close to the set image $f([x])$. It should be noted that the order of subdivisions k is a user-defined parameter. The resolution to which the above refinement procedure can be continued is limited by the number representation system in the associated computer program. Also, computational interval analysis software are designed such that the guaranteed nature of interval calculations are preserved when there is round-off for the least significant digit of an interval variable. This is simply achieved by outward rounding ([54, p. 3], [92, p. 294]).

The computational complexity of the above refinement procedure is $O(k^n)$ where k is the number of subdivisions and n is the size of interval vector $[x]$. For a certain $[x]$, therefore, complexity is polynomial with k. In order to reduce overall computation time without incurring overestimation, the user can choose to reduce k and implement one of the more efficient refinement procedures mentioned earlier. We will show in Chapter 5 that this is not necessary if the significant portion of the refinement takes place with a small number of subdivisions.

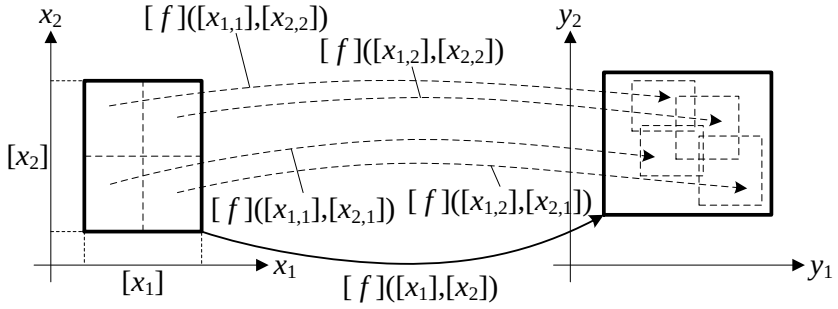

Figure 3.2. An illustration of the concept of subdivisions and refinement.

3.4.2 *Set Inversion via Interval Analysis*

Given a nonlinear function $\mathbf{f}$ from $\mathbb{R}^n$ to $\mathbb{R}^m$ and a set $\mathbb{Y}$ in $\mathbb{R}^m$, finding $\mathbb{X}$ described as

$$\mathbb{X} = \{\mathbf{x} \in \mathbb{R}^n \mid \mathbf{f}(\mathbf{x}) \in \mathbb{Y}\} = \mathbf{f}^{-1}(\mathbb{Y}) \tag{3.15}$$

is the set inversion problem [92, p. 55]. Jaulin et al. addressed this problem via an algorithm called SIVIA (Set Inversion Via Interval Analysis) [93]. For a given $\mathbb{Y} \in \mathbb{R}^m$, $\mathbb{X}$ can be bounded arbitrarily closely with a lower bound $\underline{\mathbb{X}}$ and an upper bound $\overline{\mathbb{X}}$ such that $\underline{\mathbb{X}} \subset \mathbb{X} \subset \overline{\mathbb{X}}$ provided that an inclusion function $[\mathbf{f}]$ can be found for $\mathbf{f}$.

The process of finding $\mathbb{X}$ using SIVIA is illustrated in Fig. 3.3 for 2-dimensional x and y spaces. SIVIA starts with an initial search domain $[\mathbf{x}_0]$ that is guaranteed to contain $\overline{\mathbb{X}}$. Then, the following 4-step procedure is applied:

- If the mapping $[\mathbf{f}]([\mathbf{x}])$ results in an interval (box) in the y-space that intersects with $\mathbb{Y}$ without being fully enclosed by $\mathbb{Y}$ as in Fig. 3.3(a), then $[\mathbf{x}]$ is said to contain part of the solution set $\mathbb{X}$ but regarded as *undetermined*. If the width of $[\mathbf{x}]$ is greater than a predetermined resolution parameter ε, then it needs to be bisected along the longest side and the procedure needs to be repeated recursively on each sub-box.
- If $[\mathbf{f}]([\mathbf{x}]) \cap \mathbb{Y} = \emptyset$ as in Fig. 3.3(b), then $[\mathbf{x}]$ is not part of $\mathbb{X}$ hence can be discarded.
- If $[\mathbf{f}]([\mathbf{x}]) \subset \mathbb{Y}$ as in Fig. 3.3(c), then $[\mathbf{x}] \subset \mathbb{X}$ and $[\mathbf{x}] \in \overline{\mathbb{X}}$ and $[\mathbf{x}] \in \underline{\mathbb{X}}$.
- Finally, if $[\mathbf{x}]$ is undetermined and $width([\mathbf{x}]) < \varepsilon$ as in Fig. 3.3(d), then the procedure stops for $[\mathbf{x}]$ and it is added to the upper bound $\overline{\mathbb{X}}$ of $\mathbb{X}$.

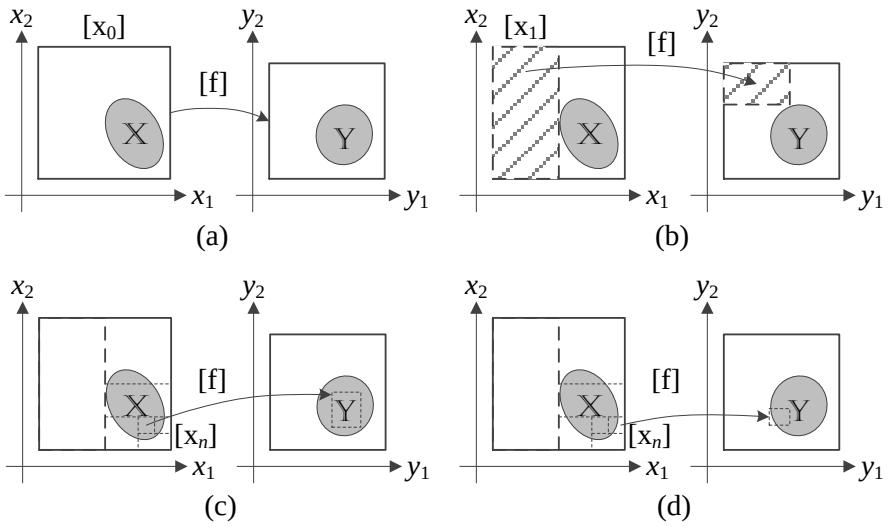

Figure 3.3. SIVIA algorithm procedure (based on Jaulin et al. 2001).

CHAPTER 4

PRECISION ANALYSIS OF MICROROBOTS

The basic rule of guaranteeing yield in robotic assembly is to make sure that the robot precision is high enough for the given assembly tolerance. One of the challenges here is to adequately allocate the assembly tolerance to the degrees of freedom of the robot for which a thorough analysis of errors and uncertainties in the system is required.

There are many sources of errors involved in the operation of a manipulator such as mechanical imprecision, sensing resolution, control performance, vibration, and structural deformation [31,32]. These errors basically account for the discrepancy between the actual system and its ideal geometric model. Some of these errors such as axial misalignments are deterministic and can be compensated for whereas some others are random in nature and determine the repeatability of the manipulator.

In microrobotics, generally the user is also the designer of the robotic system. In the case of a user-assembled manipulator, for instance, one has the chance to choose the individual axes based on the precision requirements of the aimed task and to optimize the system cost accordingly. Hence, analyzing the effect of kinematic errors of individual axes or the resolution of the feedback sensor on the overall manipulator precision provide useful information for design and component selection. The analysis also gives insight into how additional errors are introduced by the user during the manual assembly process so that they can be avoided and properly compensated for.

In conventional kinematics analysis of a manipulator, mathematical modeling is done using the nominal values of the physical quantities such as link lengths, axis

vectors, angles, and positions. The uncertainties in the knowledge of those quantities become significant when the required precision is comparable to the amount of errors which is mostly the case in microassembly and micro-manipulation tasks. Then, the system uncertainties have to be taken into account and the errors they cause have to be identified and eliminated, if possible.

In this chapter, we present the mathematical foundations of interval robot kinematics with product of exponentials (POE) formulation. We present several theorems and their proofs to establish the interval-based forward kinematics map. We define interval functions that can take the uncertain POE parameters of a manipulator as input arguments and calculate the forward kinematics map to produce an interval result, an interval homogeneous transformation matrix, that represents the deviation of the end-effector from its ideal pose.

POE formulation is a good model in the sense that it can capture kinematic errors better than the well known Denavit-Hartenberg (D-H) parameters method. Properties of a good kinematic model for error analysis and calibration purposes were identified by [32, 94] as completeness, equivalence, and proportionality. A complete kinematic model can account for any deviation of the actual robot structure away from the nominal design. For this, it must have enough number of independent kinematic parameters. It should also allow for arbitrary placement of reference frame and zero position. The number of independent kinematic parameters is to be equal to the number of contraint equations required to completely specify the pose of the tool and joint frames. Proportionality implies that small variations in the kinematic parameters should correspond to small deviations in the actual robot structure. In D-H model, for instance, small deviations in axis alignment for revolute joints with nearly parallel axes can cause widely varying model parameters. Finally, model equivalence refers to the ease with which parameters of one model is transformed into the other.

Two complete models has to be equivalent and one cannot produce a greater accuracy. With respect to these properties, exponential formulation of robot kinematics is a good model [32, 95].

4.1 Product of Exponentials (PoE) Formulation

The forward kinematics map of a serial manipulator with n joints and corresponding screw coordinates s_i, $i = 1, \ldots, n$ can be modeled using the product of exponentials formulation [96, p. 85] as follows:

$$g(\Theta) = e^{\hat{s}_1\theta_1} \ldots e^{\hat{s}_n\theta_n} g_0 \tag{4.1}$$

where g represents the end-effector configuration with respect to the base reference frame and $\Theta = (\theta_1 \ \ldots \ \theta_n)^T$ is the generalized joint displacement vector. The initial configuration, g_0, of the end-effector is transformed to the final one, $g(\Theta)$, by n screw motions of the joints given by $\exp(\hat{s}_i\theta_i)$.

Fig. 4.1 shows the screw parameters of the revolute and prismatic joint types. For the revolute joint, ω_i and q_i are the joint axis and location (i.e. any point along the joint axis) vectors, respectively. Angular joint displacement is denoted by θ_i and the location of a point of interest on the next link is represented by p_0. For the prismatic joint, the joint axis vector and joint displacement are denoted by v_i and θ_i, respectively.

The generator of a screw motion, $\hat{s}$, is called a twist and is given by (4.2). For a revolute joint, $\hat{\omega}$ and v are defined as in (4.3). For a prismatic joint, the same expression in (4.2) applies with $\omega = 0$ and v replaced by the joint axis vector.

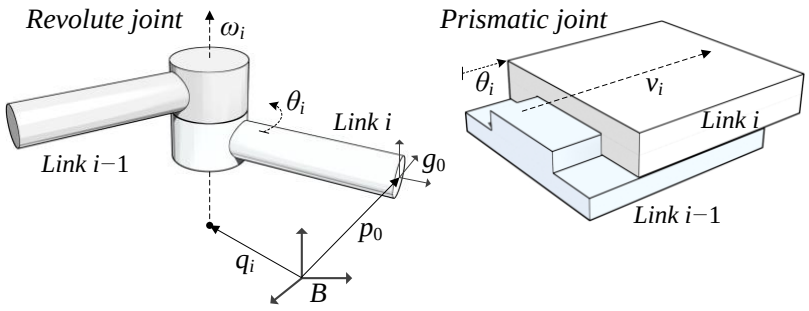

Figure 4.1. Revolute and prismatic joint parameters.

For a general screw motion with combined rotational and translational motion, $v = -\omega \times q + h\omega$ where h stands for the pitch of the screw motion.

$$\hat{s} \triangleq \begin{pmatrix} \hat{\omega} & v \\ 0 & 0 \end{pmatrix} \tag{4.2}$$

$$\hat{\omega} \triangleq \begin{pmatrix} 0 & -\omega_z & \omega_y \\ \omega_z & 0 & -\omega_x \\ -\omega_y & \omega_x & 0 \end{pmatrix} \quad v \triangleq -\omega \times q \tag{4.3}$$

In the following parts, we extend the forward kinematics map to intervals starting with rotational and translational motion transformations.

4.2 Interval Extension of Rotation Transformation

For a revolute joint with joint parameters as in Fig. 4.2(a), the rotation about ω by θ takes a point of interest on link l from p_0 to p_1. It was shown in [96, pp. 45-46] that

$$\begin{aligned} p_1 &= q + e^{\hat{\omega}\theta} l = q + e^{\hat{\omega}\theta}(p_0 - q) \\ &= q + e^{\hat{\omega}\theta} p_0 - e^{\hat{\omega}\theta} q \\ \Rightarrow \begin{pmatrix} p_1 \\ 0 \end{pmatrix} &= \underbrace{\begin{pmatrix} e^{\hat{\omega}\theta} & (I - e^{\hat{\omega}\theta})q \\ 0 & 1 \end{pmatrix}}_{T(\hat{\omega},\theta,q)} \begin{pmatrix} p_0 \\ 1 \end{pmatrix} \end{aligned} \tag{4.4}$$

where $e^{\hat{\omega}\theta}$ is the rotational part and $(I - e^{\hat{\omega}\theta})q$ is the translational part of the transformation $T(\hat{\omega}, \theta, q)$.

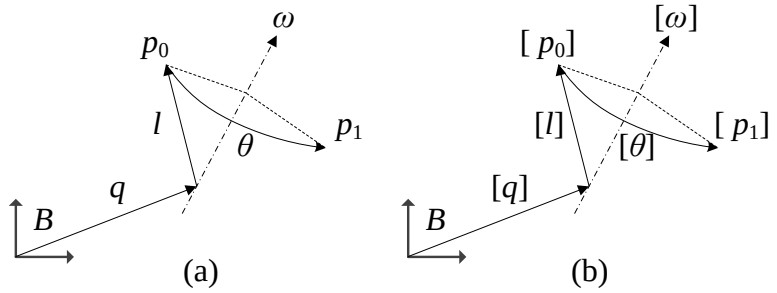

Figure 4.2. Rotation transformation and its interval representation.

It can be seen that the interval extension of revolute joint formulation first requires finding the interval extension for the rotation transformation $exp(\hat{\omega}\theta)$. Extending the formulation in (4.4) to the interval case depicted in Fig. 4.2(b) can be done by first defining a rotation transformation as follows:

$$\exp(\hat{\omega}\theta) \subseteq [R]([\hat{\omega}], [\theta]) \triangleq \exp([\hat{\omega}][\theta]) \tag{4.5}$$

where $\hat{\omega} \in [\hat{\omega}]$ and $[\hat{\omega}] \subset so(3)$, $\theta \in [\theta]$ and $[\theta] \in \mathbb{IR}$, and $[R]([\hat{\omega}], [\theta])$ is an inclusion isotonic interval function.

In order to find an inclusion isotonic closed-form expression for $[R]([\hat{\omega}],[\theta])$, we will use *Rodrigues' formula* [96, p. 28]. For $\hat{\omega} \in so(3)$ and $\theta \in \mathbb{R}$, $exp(\hat{\omega}\theta)$ is given as

$$e^{\hat{\omega}\theta} = I + \frac{\hat{\omega}}{\|\omega\|}\sin(\|\omega\|\theta) + \frac{\hat{\omega}^2}{\|\omega\|^2}\Big(1 - \cos(\|\omega\|\theta)\Big) \tag{4.6}$$

The interval extension of Rodrigues' formula for interval arguments $[\hat{\omega}] \subset so(3)$ and $[\theta] \in \mathbb{IR}$ first requires a proper definition for interval vector norm. The classical p-norm definition with real-valued absolute value function [54, p. 15] [97]

$$\|[\omega]\|_p \triangleq \left(\sum_{j=1}^{3} |[\omega_j]|^p\right)^{\frac{1}{p}} \tag{4.7}$$

is not a rational interval function as it is not inclusion isotonic. Instead, the following 2-norm definition that produces an interval result can be used.

$$\|[\omega]\|_2 \triangleq \sqrt{|[\omega_1]^2 + [\omega_2]^2 + [\omega_3]^2|} \tag{4.8}$$

where the absolute value function, $|[x]|$, is defined as [98]

$$|[x]| \triangleq \{|x| : x \in [x]\} \tag{4.9}$$

It can be shown as follows that this norm definition is inclusion isotonic.

Lemma 2. *For* $\omega \triangleq (\omega_1 \quad \omega_2 \quad \omega_3)^T$*, assume* $\omega \in [\omega] \in \mathbb{IR}^3$*. If* $\|[\omega]\|_2$ *is defined as in (4.8), then the following inclusion holds:*

$$\|\omega\|_2 \subseteq \|[\omega]\|_2 \tag{4.10}$$

Proof. First, the above inclusion holds for $[\omega] = \omega$, satisfying (3.10). Let $[f]([\omega]) \triangleq [\omega_1]^2 + [\omega_2]^2 + [\omega_3]^2$. Since $[f]$ involves a finite sequence of arithmetic operations, it is a rational interval function. Hence, it follows from Lemma 1 (in Chapter 3) that it is inclusion isotonic. Then, $\|[\omega]\|_2 = \sqrt{|[f]([\omega])|}$. Since the square root function is

monotonic, it is inclusion isotonic too. Also, the interval extension of absolute value function $|[x]| \triangleq \{|x| : x \in [x]\}$ is analytically defined as

$$\text{abs}([x]) = |[x]| \triangleq \begin{cases} [\underline{x}, \overline{x}] & \underline{x} \geq 0 \\ [-\overline{x}, -\underline{x}] & \overline{x} \leq 0 \\ [0, \max(|\underline{x}|, |\overline{x}|)] & \text{otherwise} \end{cases} \tag{4.11}$$

This is a standard extension with inclusion isotonicity [54, p. 198]. Therefore, it satisfies Theorem 1 (in Chapter 3) so the inclusion in (4.10) holds. □

Also, the trigonometric functions in (4.6) have standard inclusion isotonic extensions [54, p. 198]. That is, given $[\omega] \in \mathbb{IR}^3$, $[\theta] \in \mathbb{IR}$, $\omega \in [\omega]$, and $\theta \in [\theta]$, the following inclusions hold:

$$\begin{aligned} \sin(\|\omega\|_2\theta) &\subseteq \sin(\|[\omega]\|_2[\theta]) \\ \cos(\|\omega\|_2\theta) &\subseteq \cos(\|[\omega]\|_2[\theta]) \end{aligned} \tag{4.12}$$

Theorem 2. *Given $[\omega] \in \mathbb{IR}^3$, $[\theta] \in \mathbb{IR}$, $\omega \in [\omega]$, $\theta \in [\theta]$, and the following interval function*

$$\begin{aligned} [R]([\omega], [\theta]) \triangleq \; & I + \frac{[\hat{\omega}]}{\|[\omega]\|_2} \sin(\|[\omega]\|_2[\theta]) \\ & + \frac{[\hat{\omega}]^2}{\|[\omega]\|_2^2} \left(1 - \cos(\|[\omega]\|_2[\theta])\right) \end{aligned}, \tag{4.13}$$

the following inclusion holds:

$$e^{\hat{\omega}\theta} \subseteq [R]([\omega], [\theta]) \tag{4.14}$$

Proof. First, it is trivial to show that the above inclusion holds for $[\omega] = \omega$ and $[\theta] = \theta$, satisfying (3.10). From Lemma 2 and (4.12), it follows that (4.13) is a rational interval function involving a finite sequence of interval arithmetic operations

and inclusion isotonic interval functions. Hence, it is inclusion isotonic too, satisfying Theorem 1. This leads to that the above inclusion holds. □

Therefore, $[R]([\omega],[\theta])$ is an interval extension function for the rotation transformation $\exp(\hat{\omega}\theta)$.

4.3 Interval Extension of Revolute Joint Transformation

Having found the interval extension of the rotation transformation part in (4.4), we can now formulate the interval extension of the revolute joint transformation in Fig.4.2(b). For the translational part of (4.4), $[R]([\hat{\omega}],[\theta])$ can be used as in the following lemma.

Lemma 3. *Let* $[\hat{\omega}] \subset so(3)$, $[\theta] \in \mathbb{IR}$, *and* $[q] \in \mathbb{R}^3$. *Given* $\hat{\omega} \in [\hat{\omega}]$, $\theta \in [\theta]$, $q \in [q]$, *and* $[R]([\hat{\omega}],[\theta])$ *defined as in 4.13, the following inclusion holds:*

$$(I - e^{\hat{\omega}\theta})q \subseteq \Big(I - [R]([\omega],[\theta])\Big)[q] \tag{4.15}$$

Proof. Point evaluation of the right hand side of (4.15) is equal to the left hand side. Also, it is a rational interval function as it is obtained via a finite sequence of interval arithmetic operations. From Lemma 1, therefore, it is inclusion isotonic and satisfies Theorem 1, leading to the above inclusion. □

From Theorem 2 and Lemma 3, the interval extension for the joint transformation of a revolute joint can be written as

$$[T]([\hat{\omega}],[\theta],[q]) \triangleq \begin{pmatrix} [R]([\omega],[\theta]) & \Big(I - [R]([\omega],[\theta])\Big)[q] \\ 0 & 1 \end{pmatrix} \tag{4.16}$$

Therefore, Theorem 2 and Lemma 3 lead to the following theorem.

Theorem 3. *For $\hat{\omega} \in [\hat{\omega}]$, $\theta \in [\theta]$, $q \in [q]$, and $p_0 \in [p_0]$ the following inclusion holds:*

$$T(\hat{\omega}, \theta, q) \begin{pmatrix} p_0 \\ 1 \end{pmatrix} \subseteq [T]([\hat{\omega}], [\theta], [q]) \begin{pmatrix} [p_0] \\ 1 \end{pmatrix} \tag{4.17}$$

Proof. First, the right hand side of (4.17) is equal to the left hand-side when $[\hat{\omega}] = \hat{\omega}$, $[\theta] = \theta$, and $[q] = q$, satisfying (3.10). Also, it is a rational interval function as it is obtained via a finite sequence of interval arithmetic operations. From Lemma 1, therefore, it is inclusion isotonic and satisfies Theorem 1, leading to the above inclusion. □

Theorem 3 can be generalized to transformation of solid-body configurations by the following corollary.

Corollary 1. *For $\hat{\omega} \in [\hat{\omega}]$, $\theta \in [\theta]$, $q \in [q]$, and $g_0 \in [g_0]$, where $[g_0] \subset SE(3)$ the following inclusion holds:*

$$T(\hat{\omega}, \theta) g_0 \subseteq [T]([\hat{\omega}], [\theta], [q])[g_0] \tag{4.18}$$

Proof. The proof follows directly from the reasoning in the proof of Theorem 3. □

4.4 Interval Extension of Prismatic Joint Transformation

For a prismatic joint, the screw in (4.2) applies with $\omega = 0$ and v replaced by the joint axis vector. Hence, the screw coordinates is $s = (0, v)$. The exponential of this screw is given by [96, p. 47]

$$e^{\hat{s}\theta} = T(v, \theta) \triangleq \begin{pmatrix} I & \theta v \\ 0 & 1 \end{pmatrix} \tag{4.19}$$

where θ represents the amount of linear displacement and v is the joint axis vector. The interval extension of $T(v, \theta)$ calls for the following theorem.

Theorem 4. *Given* $[v] \in \mathbb{IR}^3$, $[\theta] \in \mathbb{IR}$, $v \in [v]$, $\theta \in [\theta]$, *and the following interval function*

$$[T]([v], [\theta]) \triangleq \begin{pmatrix} I & [\theta][v] \\ 0 & 1 \end{pmatrix}, \tag{4.20}$$

the following inclusion holds:

$$T(v, \theta) \subseteq [T]([v], [\theta]) \tag{4.21}$$

Proof. Similar to the previous proofs, the point evaluation of $[T]([v], [\theta])$ gives $[T](v, \theta) = T(v, \theta)$, satisfying (3.10). Second, the displacement component of $[T]([v], [\theta])$ involves an interval arithmetic operation, hence is inclusion isotonic and satisfies Theorem 1. Then, the above inclusion holds. □

Therefore, $[T]([v], [\theta])$ is an interval extension of prismatic joint transformation $e^{\hat{s}\theta}$ with $s = (0, v)$.

4.5 Interval Extension of General Screw Transformation

Screw motion can be described with a homogeneous transformation obtained via the exponential of the corresponding twist $\hat{s}\theta$. An interval extension function for $[T]$ that satisfies $\exp(\hat{s}\theta) \subseteq [T]([\hat{s}], [\theta])$ can be found by calculating the exponential of the corresponding interval twist $[\hat{s}][\theta]$. Note that $[\hat{s}][\theta]$ is a 4×4 interval matrix and bounding its exponential is not a trivial computation. Alternatively, we can use the following closed form expression [96, p. 46]:

$$T(\hat{s},\theta) = e^{\hat{s}\theta} = \begin{pmatrix} e^{\hat{\omega}\theta} & (I - e^{\hat{\omega}\theta})q + h\theta\omega \\ 0 & 1 \end{pmatrix} \tag{4.22}$$

where $s = (\omega, -\omega \times q + h\omega)$ is the screw coordinate. Using the previous lemmas and theorems, the following interval extension for screw transformation can be presented.

Theorem 5. *Given* $[\hat{s}] \subseteq SE(3)$, $[\theta] \in \mathbb{IR}$, $s \in [s]$, $\theta \in [\theta]$, *and the following interval function*

$$[T]([\hat{s}],[\theta]) \triangleq \begin{pmatrix} e^{[\hat{\omega}][\theta]} & (I - e^{[\hat{\omega}][\theta]})[q] + [h][\theta][\omega] \\ 0 & 1 \end{pmatrix}, \tag{4.23}$$

the following inclusion holds:

$$T(\hat{s},\theta) = e^{\hat{s}\theta} \subseteq [T]([\hat{s}],[\theta]) \tag{4.24}$$

Proof. The inclusion in (4.24) holds for $[T](\hat{s},\theta)$ so it satisfies (3.10). The expression for $[T]([\hat{s}],[\theta])$ in (4.23) is composed of previously extended components such as $\exp([\hat{\omega}][\theta])$ in Theorem 2 and $(I - e^{[\hat{\omega}][\theta]})[q]$ in Lemma 3. Also, $[h][\theta][\omega]$ is a rational interval function hence is inclusion isotonic. Then, $[T]([\hat{s}],[\theta])$ is a finite combination of inclusion isotonic interval extension functions and is inclusion isotonic itself. Hence, it is an interval extension function satisfying Theorem 1. □

On the other hand, the alternative way of bounding $\exp([\hat{s}][\theta])$ calls for a more elaborate formulation. We will use the following definitions for ease of notation: $S \triangleq \hat{s}\theta$ and $[S] \triangleq [\hat{s}][\theta]$. There are a few methods proposed in the literature for computation of interval matrix exponential [99, 100] which are based on bounding the truncated Taylor series expansion of the matrix exponential. We will follow the method of [100] to develop the other interval extension of screw transformation.

Given an $n \times n$ real matrix S, its exponential can be expressed as

$$\exp(S) = \sum_{i=0}^{k} \frac{S^i}{i!} + \sum_{i=k+1}^{\infty} \frac{S^i}{i!} = H(S,k) + M(S,k) \tag{4.25}$$

The elements m_{ij} of the remainder term M are well-known to be bounded as [101]

$$|m_{ij}| \leq \rho(\|S\|, k) \triangleq \frac{\|S\|^{k+1}}{(k+1)!(1 - \frac{\|S\|}{k+2})} \tag{4.26}$$

Goldsztejn shows in [100] that the same bound applies to the exponentiation of an interval matrix $[S]$ such that

$$\exp([S]) \subseteq H([S],k) + M([S],k) \tag{4.27}$$

for $k \in \mathbb{N}$ such that $k + 2 > \|[S]\|_\infty$ and

$$M([S],k) \triangleq \rho(\|[S]\|_\infty, k).\,[E] \tag{4.28}$$

where $[E] \in \mathbb{IR}^{n \times n}$, $[e_{ij}] \triangleq [-1, +1]$ for $i, j = 1, \ldots, n$.

In order to reduce the overestimation due to interval dependency (i.e. multiple occurrence of an interval variable in an equation) and improve computational performance, the truncated exponential of $[S]$ is computed using the Horner scheme [102] such that

$$H([S],k) = I + [S]\left(I + \frac{[S]}{2}\left(\ldots\left(I + \frac{[S]}{k}\right)\right)\right) \tag{4.29}$$

In order to improve computational efficiency and accuracy as well as to satisfy $k+2 > \|[S]\|_\infty$ with a smaller k value, the *scaling and squaring* method is used as follows:

$$\exp([S]) \subseteq \left(\exp\left(\frac{[S]}{2^\alpha}\right)\right)^{2^\alpha} \tag{4.30}$$

where α is an integer. Therefore, the interval extension function that bounds the solid body transformation of a screw motion is given as

$$[T]([\hat{s}],[\theta]) \triangleq \left(H\left(\frac{[\hat{s}][\theta]}{2^\alpha}, k\right) + M\left(\frac{[\hat{s}][\theta]}{2^\alpha}, k\right)\right)^{2^\alpha} \tag{4.31}$$

for $(k+2)2^{\alpha} > \|[\hat{s}][\theta]\|$ such that

$$\exp([\hat{s}][\theta]) \subseteq [T]([\hat{s}],[\theta]) \tag{4.32}$$

It can be shown that the extension functions in (4.23) provides tighter bounds in less computational time than that in (4.31).

4.6 Interval Extension of the POE Formulation

Having found interval extension functions for joint transformations, we can now extend the POE formulation.

Theorem 6. *Let $[T]([\hat{s}_i],[\theta_i])$, $i = 1,\ldots,n$, be the interval extension of joint transformations of a serial manipulator with n joints and uncertain joint parameters represented by $[\hat{s}_i]$ and $[\theta_i]$ and $[g_0]$ be its uncertain initial configuration. Then, for $\hat{s}_i \in [\hat{s}_i]$, $\theta_i \in [\theta_i]$, and $g_0 \in [g_0]$, the following inclusion holds:*

$$\begin{aligned} g(\Theta) &\triangleq e^{\hat{s}_1\theta_1}\ldots e^{\hat{s}_n\theta_n}g_0 \\ &\subseteq [T]([\hat{s}_1],[\theta_1])\ldots[T]([\hat{s}_n],[\theta_n])[g_0] \end{aligned} \tag{4.33}$$

Proof. The right hand side of (4.33) is a rational interval function as it is obtained via a finite sequence of interval arithmetic operations. From Lemma 1, therefore, it is inclusion isotonic. Then, Theorem 1 is satisfied and leads to the above inclusion. □

Hence, the interval extension function for the forward kinematics map is

$$[g]([\Theta]) \triangleq [T]([\hat{s}_1],[\theta_1])\ldots[T]([\hat{s}_n],[\theta_n])[g_0] \tag{4.34}$$

4.7 Chapter Conclusions

In this chapter, we proposed a new general methodology for analysis of kinematic errors propagated in robotic manipulators. We extended the forward kinematic

map of serial manipulator to intervals using the product of exponentials formulation with interval joint parameters. Modeling the kinematics parameters of a manipulator with intervals allows us to capture the effect of the uncertainties and errors involved in real systems. An important application of this method is in the analysis of modular precision manipulators that can be assembled using individual linear and rotary stages as will be shown in the next chapter. The solutions provided by our interval functions guarantee bounding all possible solutions for the location of the end-effector. They also show how much the end-effector deviates from its nominal pose, hence providing a precision measure. This method can also be applied to analysis of tolerance stack-up in a multi-axis assembly.

CHAPTER 5

VALIDATION OF PRECISION ANALYSIS

This chapter focuses on analyzing the precision aspects of multi-axis manipulators and microassembly robots via simulations and experimental studies based on the precision analysis method introduced in the previous chapter. We apply our interval analysis method to model and analyze the kinematic errors. We show that the method offers a convenient way of carrying out the error propagation and tolerance analysis tasks. Also, it provides a way of predicting and evaluating the precision in microassembly operations.

The analyses that follow are done for parts of the micro-assembly system shown in Fig. 5.1. The system consists of a total of 13-DOF arranged into four separate manipulators. The $XY\theta$ manipulator carries the sample holder where MEMS parts can be placed. The other three manipulators carry tools such as a microgripper, micromanipulator, and vacuum tweezer. Two microscope cameras, one from top and one from side, are used to image the assembly area.

5.1 Case Study 1 –Uncertain Joint Angle and Position

The simulation of the simple case of a revolute joint with joint error of ± 2 deg is given in Fig. 5.2 where the final position $[p]([\theta])$ of the tip of the link is shown for nominal rotations of 10 deg to 90 deg with 10 deg increments. The error assumption is exaggerated in comparison to a practical case in order to illustrate its effects on the task space precision of the link tip position. The rectangular boxes Fig. 5.2 enclose the interval of tip position on the x-y plane. A close up view of one of those

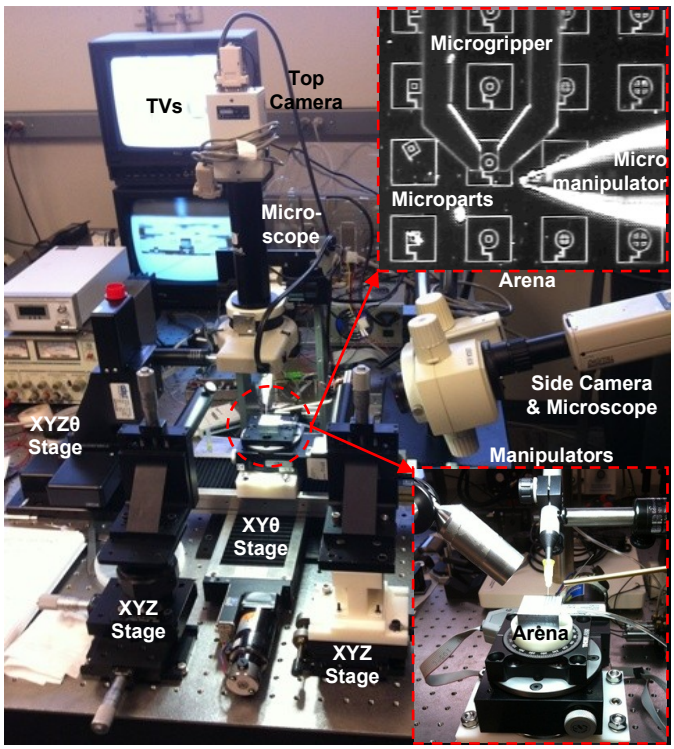

Figure 5.1. Analyzed micro-assembly system.

intervals in Fig. 5.3 shows that $[p]([\theta])$ calculation using the formulation in section 4.2 rigorously bounds the set image $p([\theta])$ that is roughly represented by solution points found using Monte-Carlo simulation of 5 samples uniformly picked from $[\theta]$. In other words, $p([\theta]) \approx \{\, p(\theta_i) \,|\, \theta_i \in \{\theta_{nom} - 2^o, \theta_{nom} - 1^o, \theta_{nom}, \theta_{nom} + 1^o, \theta_{nom} + 2^o\} \,\}$

Simulation results for a scenario in which the lengths of the links and hence the positions of the joints are imprecisely known is shown in Fig. 5.4. In this case, the second joint is rotated with precise steps of 20 deg and transforms the initial uncertain position $[p](0, [q])$ of the tip of link 2. The resulting intervals bounding the corresponding set images are shown with $[p](\theta, [q])$ and $p(\theta, [q])$, respectively. Comparison of the two results in Fig. 5.5 indeed shows that the rectangular interval boundaries enclose the set image of the transformation obtained by Monte Carlo simulation.

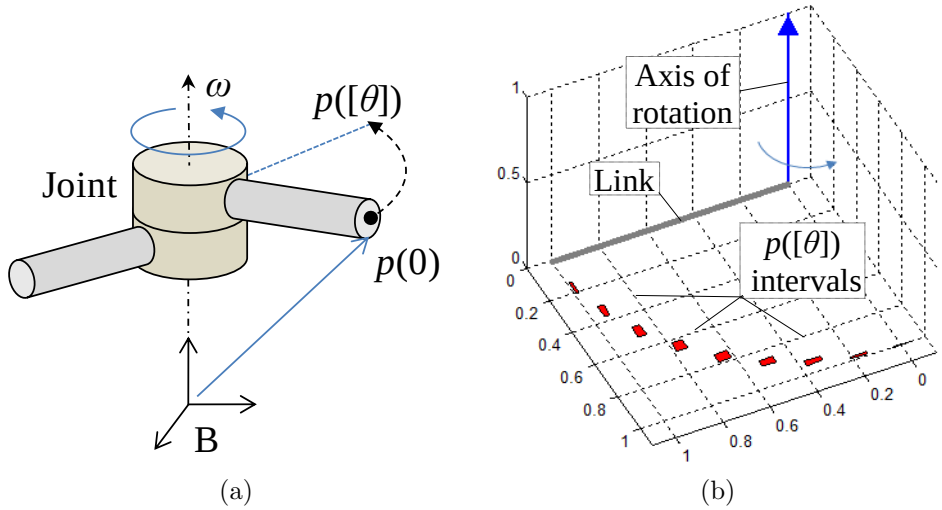

Figure 5.2. A revolute joint simulation with ±2 deg joint error.

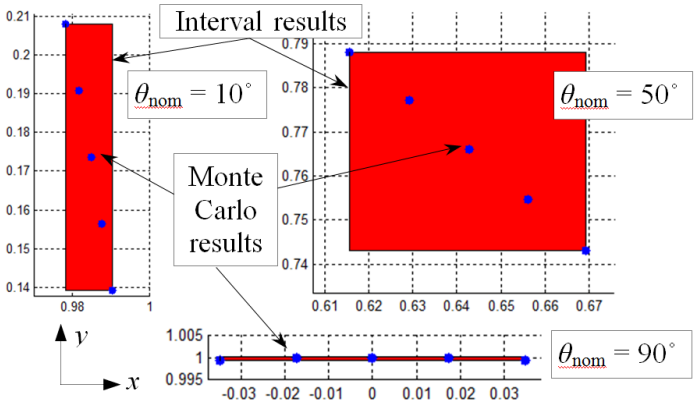

Figure 5.3. Interval analysis versus Monte-Carlo simulation of ±2 deg joint resolution error.

5.2 Case Study 2 –Uncertain Joint Axis

The case of an uncertain rotation axis is shown in Fig. 5.6 where there is up to 8 deg of uncertain tilt around x and y axes. The tip position of the link after rotations of 10 deg to 90 deg with 10 deg increments are found by using both the interval method in part 4.5 and Monte Carlo simulation. The close-up view of one of the interval bounds show that the set image obtained using the Monte Carlo simulation is completely enclosed.

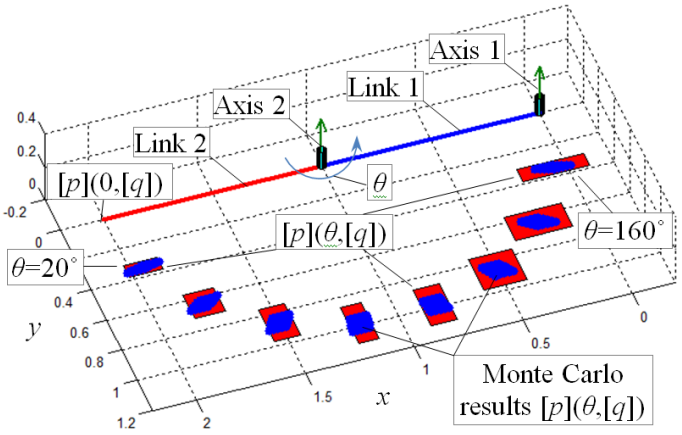

Figure 5.4. Planar two-link manipulator with nominal link lengths of 1 unit and ±4% error.

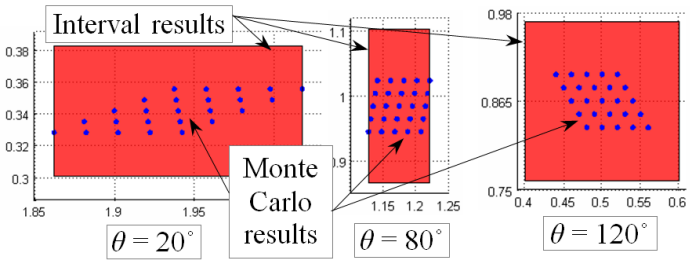

Figure 5.5. Interval analysis versus Monte Carlo simulation results for uncertain link lengths.

The three simulations given above are repeated using interval refinement described in part 3.4.1. In the comparison shown in Fig. 5.7, the uncertain intervals are divided into as many subintervals as the number of corresponding Monte Carlo sample solutions. For instance, in the case of the simulation in Fig. 5.2, the comparison is done for $\theta_{nominal} = 50\,\text{deg}$. Five sample points that uniformly span the uncertain range of the joint angle are used for Monte Carlo simulation. Hence, the interval solution also contains 5 subdivisions. In the case of the simulation in Fig. 5.4, there are 5 samples and subdivisions for the length of each link, resulting in 25 Monte Carlo samplings and subinterval evaluations. Similarly for Fig. 5.6, there are 5 samples for each of the uncertain tilt of the joint axis around x and y axes, resulting in 25

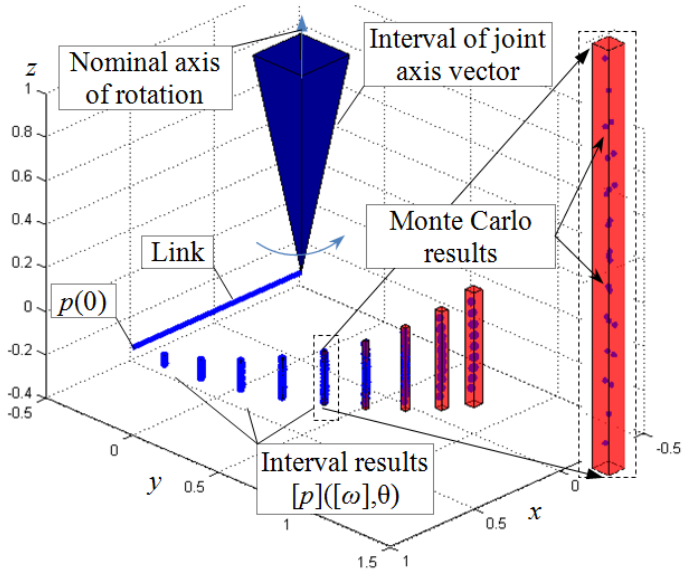

Figure 5.6. Rotation around an uncertain joint axis (with 8 deg of error) and bounds for link tip error.

samplings and subinterval evaluations. The results in Fig. 5.7 show that even with a very rough refinement (5 subdivisions per uncertain parameter), the error bounds can be significantly tightened.

5.3 Case Study 3 –Analysis of a 5-DOF Microassembly Robot

Simulations of a basic microassembly operation discussed below show that our interval analysis approach can provide precision bounds for a manipulator under the influence of uncertain error sources. The manipulator axes are assumed have small geometric errors that cannot be compensated for. Given the range of errors in these axes, we calculate the precision bounds on the end-effector pose using the interval extension of the forward kinematics map of the robot. The objective of this simulation is to evaluate the tolerance needed for the microgripper to be able to pick-up the peg as well as to evaluate the tolerance for the hole so that the peg can be inserted without closed-loop visual feedback except for the joint encoder readings.

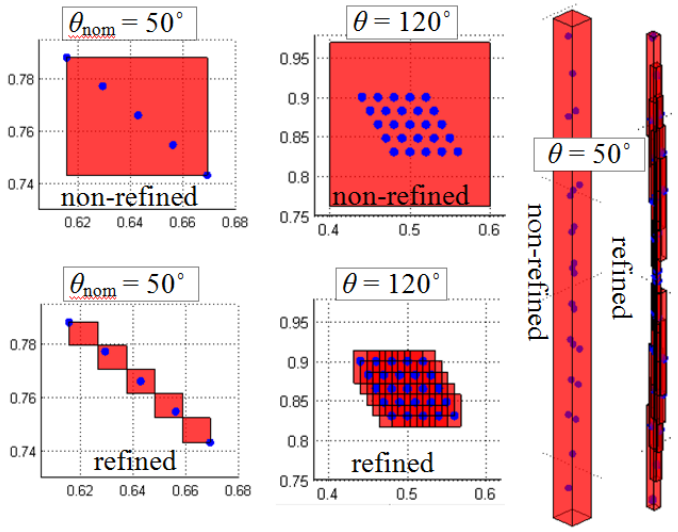

Figure 5.7. Comparison of the previous results with those obtained with interval refinement.

Fig. 5.8 shows a 5 degrees-of-freedom (DOF) robot that is a typical example for microassembly operations. The joint parameter uncertainty assumptions for the parameters in Fig. 5.9 are shown in Table 5.1.

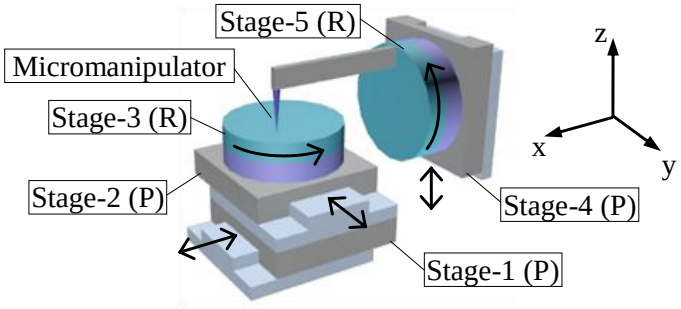

Figure 5.8. A typical micromanipulator setup with 5 DOF.

Simulation of this system is carried out for a standard peg-in-hole operation described in Fig. 5.10 with the tolerances of the microgripper and the hole for positioning errors. Table 5.2 lists the steps of the peg-in-hole operation. Figure 5.11

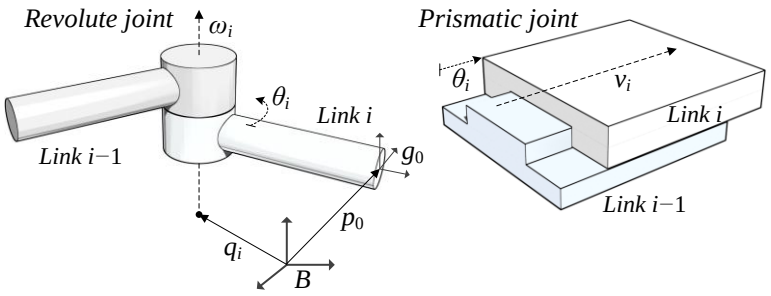

Figure 5.9. Revolute and prismatic joint parameters.

shows the initial poses of the peg, hole, and the manipulator in the reference coordinate frame that is initially coincident with the center of the Stage-3 top. Typically, the range of motion required in Stage-4 is much smaller than that in stage 1 and 2. Hence, the error in tool position due to motion of Stage-4 is much smaller than the error in peg position due to motion of stage 1 and 2. Also, since the tip of the manipulator is designed to be along the axis of rotation of Stage-5, Abbe error at the tool tip due to rotation of Stage-5 is much smaller than that at the peg or hole pose due to rotation of Stage-3. Therefore, the following examples will only take into account the errors caused by the first three stages (PPR) of the system.

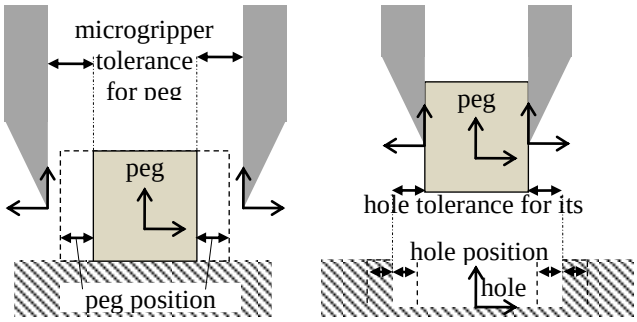

Figure 5.10. Illustration of peg-in-hole task.

Table 5.1. Simulated joint parameter values

Axis	Joint Axis (mm)	Joint Disp.	Joint Pos. (mm)
1(P)	$[v_{1x}] = [0.999999, 1.0]$ $[v_{1y}] = [-0.001, 0.001]$ $[v_{1z}] = [-0.001, 0.001]$	$[\theta_1] = \theta_{1,nom}+$ $[-10^{-3}, 10^3]$ (mm)	-
2(P)	$[v_{2x}] = [-0.001, 0.001]$ $[v_{2y}] = [0.999999, 1.0]$ $[v_{2z}] = [-0.001, 0.001]$	$[\theta_2] = \theta_{2,nom}+$ $[-10^{-3}, 10^3]$ (mm)	-
3(R)	$[\omega_{3x}] = [-0.001, 0.001]$ $[\omega_{3y}] = [-0.001, 0.001]$ $[\omega_{3z}] = [0.999999, 1.0]$	$[\theta_3] = \theta_{3,nom}+$ $[-10^{-3}, 10^3]$ (rad)	$[q_{3x}] = [-0.01, 0.01]$ $[q_{3y}] = [-0.01, 0.01]$ $[q_{3z}] = [0.0, 0.0]$
4(P)	$[v_{4x}] = [-0.001, 0.001]$ $[v_{4y}] = [-0.001, 0.001]$ $[v_{4z}] = [0.999999, 1.0]$	$[\theta_4] = \theta_{4,nom}+$ $[-10^{-3}, 10^3]$ (mm)	-
5(R)	$[\omega_{5x}] = [0.999999, 1.0]$ $[\omega_{5y}] = [-0.001, 0.001]$ $[\omega_{5z}] = [-0.001, 0.001]$	$[\theta_5] = \theta_{5,nom}+$ $[-10^{-3}, 10^3]$ (rad)	$[q_{5x}] = [-0.02, 0.02]$ $[q_{5y}] = [-0.02, 0.02]$ $[q_{5z}] = [-0.02, 0.02]$

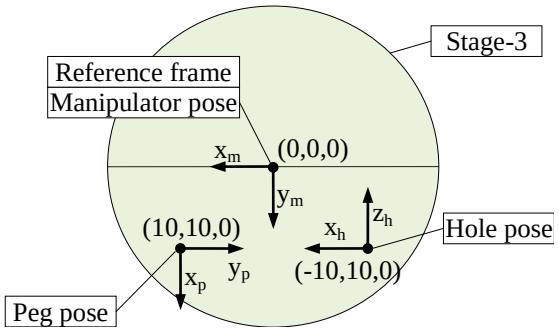

Figure 5.11. Initial poses (in mm) of the peg, hole, and manipulator on Stage-3 top plane.

The move to pick-up configuration in Fig. 5.11 involves lifting the manipulator off slightly, rotating Stage-3 by 90 deg, and moving the linear stages by $(10, 10)$ mm along their respective axes to nominally align the peg pose with the manipulator pose at the origin of the reference coordinate frame. The error in positioning of the peg is calculated using both the interval method and Monte Carlo simulations. Figure 5.12 shows the results for a few refinement cases. It has been observed that the

Table 5.2. Simplified steps of a cyclic pick-and-place operation

No	Current State	Action	Next State
0	Zero state	Move to pick configuration (Stages 1-5)	1
1	Pick config	Pick-up part (Stage-4)	2
2	Part Picked?	Yes Move to place config. (Stages 1-5)	3
2	Part Picked?	No Move to pick config. (Stages 1-5)	1
3	Place config.	Place part (Stages 4-5)	4
4	Part Placed?	Yes Move to pick config. (Stages 1-5)	1
4	Part Placed?	No - Move to place config. (Stages 1-5)	3

number of interval subdivisions provide a monotonic decrease in the overestimation of the error bound. This decrease is faster for some of the interval variables than the others. As shown in Fig. 5.13, for instance, dividing θ into 3 subintervals results in about 36% reduction in bound volume whereas dividing $[\omega_3]$ into 9 results in 32% reduction. Thus, interval analysis provides information about the sensitivity of the manipulator pose to individual error sources. Also, Fig. 5.12(b) shows that the in-plane positioning error of the peg is bounded by 0.084 mm. Then, a microgripper with 0.084 mm lateral gripping tolerance is guaranteed to compensate for the lateral positioning error of the peg during pick-up. It should be noted that the error bounds provided by interval analysis can further be improved in the computational expense of more refinements of interval variables. Also, the computational complexity of having N number of refinements is equivalent to running Monte Carlo simulations for N samples. Therefore, Monte Carlo simulations provide point results that are only valid at those particular points, whereas for a similar computational cost interval analysis provides a set of intervals that is guaranteed to cover the whole solution space.

After the peg is picked up by the manipulator, stages 1-3 move to the 'place' configuration and nominally align the hole with the peg. While the positioning error

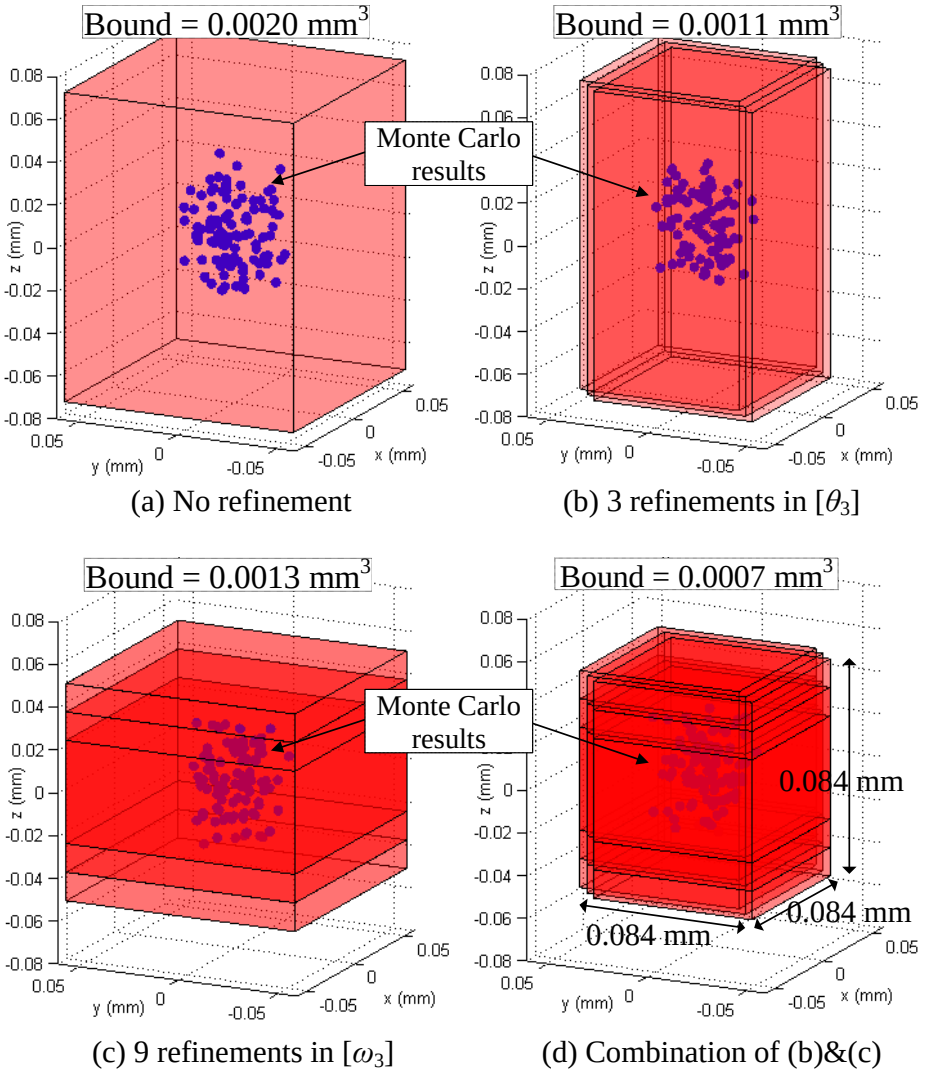

Figure 5.12. Interval bounding of peg position that has volumetric error of 0.0004 mm^3.

of the hole is similar to that of the peg, the orientation error of the hole is also important during the insertion operation. Fig. 5.14 shows the orientation error components about the three rotation axes with a volumetric representation. Fig. 5.14(d) shows that tilt of the hole about x and y axes are guaranteed to be less than 4.2 milliradians (mrad). Hence, it can be concluded that an insertion tolerance of 4.2 mrad about lateral axes is guaranteed to compensate for the misalignment of the hole

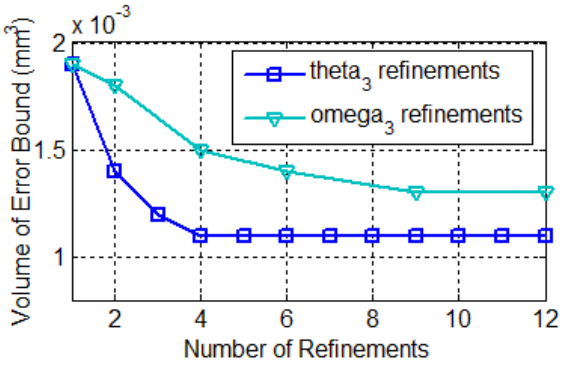

Figure 5.13. Volume of error bound vs number of refinements.

about the same axes. A similar statement holds for the z axis for which the tolerance required is 2.2 mrad.

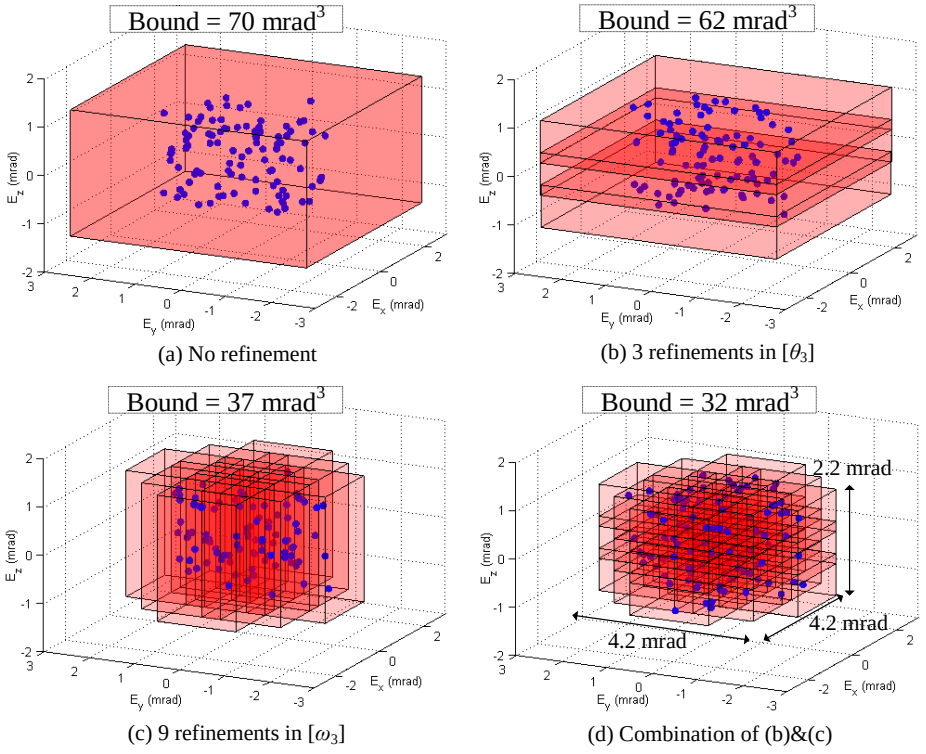

(a) No refinement

(b) 3 refinements in $[\theta_3]$

(c) 9 refinements in $[\omega_3]$

(d) Combination of (b)&(c)

Figure 5.14. Interval bounding of hole orientation that has volumetric error of 16 mrad^3.

In MATLAB/INTLAB, the average computational time required for the interval evaluation of the forward kinematics map in part 4.6 for the $XY\theta$ manipulator is 17.6 ms on an Intel i5 2.67 GHz computer. Evaluation of the point-valued kinematics map via Monte-Carlo sampling requires 1.8 ms per sample. Performing 100 sampling operations as in Fig. 5.12, for instance, takes about 18 ms whereas a total of 27 refinement operations as in Fig. 5.12(b) takes about 470 ms. However, it must be recognized that no finite number of Monte-Carlo samplings can provide the guaranteed bound that we obtained via our interval method.

5.4 Numerical Comparison of the Two Interval Screw Transformations

In this simulation, we compare the two interval extension functions found for general screw transformation in (4.23) and (4.31). A screw joint shown in 5.15 is defined with the parameters given in Table 5.3. The joint is rotated about its axis with 10^o increments from 10^o to 90^o and the tip position of the link is calculated using the extension functions in (4.23) and (4.31). For the formulation in (4.31), both k and α are chosen to be 5. Results show that method 1 provides a tighter bound than method 2 in less computational time. Actually, method 1 provides a very tight interval bound by comparing it with 125 Monte Carlo simulation results. In MATLAB/INTLAB on an Intel i5 2.67GHz computer, the average time to evaluate (4.23) is 5.4 ms whereas it is 6.3 ms for (4.31). Note that the interval results are found via a single evaluation of (4.23) and (4.31) using the interval arguments in Table 5.3. Evaluation of a single Monte Carlo sample through (4.22) takes about 1.74 ms. It should be noted, however, that a finite number of Monte Carlo simulations cannot guarantee bounding of all possible solutions.

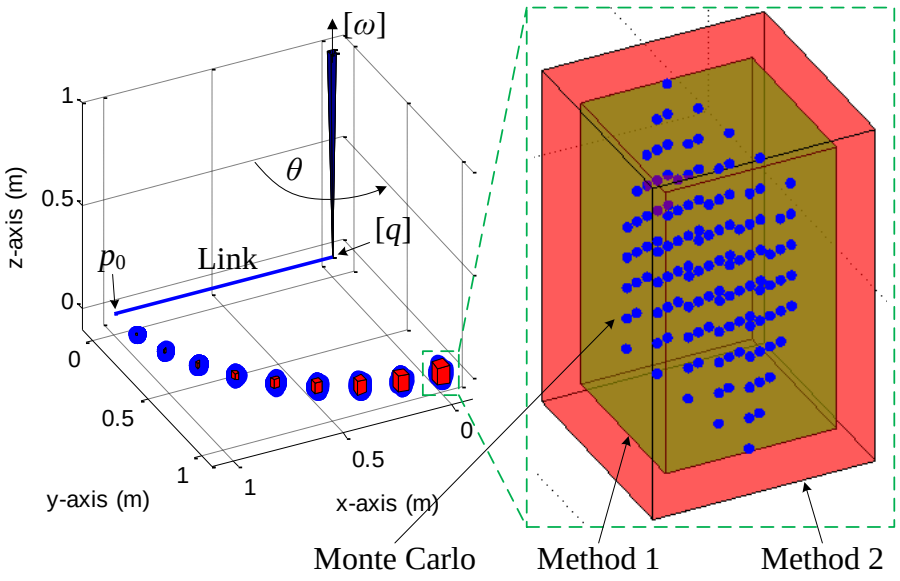

Figure 5.15. Comparison of the two extension functions: Method 1 (4.23), Method 2 (4.31)).

Table 5.3. Screw joint parameters.

$[\omega]$	$[q]$	p_0	$[h]$	θ
$(\pm 0.01, \pm 0.01, 1)$	$(\pm 0.01, \pm 0.01, \pm 0.01)$	$(1, 0, 0)$	± 0.01	$10^o, 20^o, 30^o \ldots, 90^o$

5.5 Experiments on the Interval Extension of Forward Kinematics Map

The accumulation of errors in assembling modular multi-axis manipulators can be analyzed using intervals as described in this case study. Analysis of tolerance stack-ups is an important topic in mechanism assembly. There are different mathematical models for approaching this problem. Worst case and statistical analyses are two common ways. As for computational methods, Monte-Carlo simulations are very popular [42]. We introduce interval analysis as new method for tolerance analysis.

We consider the kinematic chain of the $XY\theta$ manipulator in Fig. 5.1. The three axes stacked on top of each other is shown in Fig. 5.16. The individual axes are assembled together using mechanical fixtures such as base plates, bolts, and nuts.

Assembly fixtures introduce errors into the kinematic design of a modular manipulator due to their clearances. Although these errors are deterministic and can later be compensated for, it is useful to estimate the extent of the end effector deviation from the nominal values so that fixture design or selection can be done with better prior knowledge about their effects.

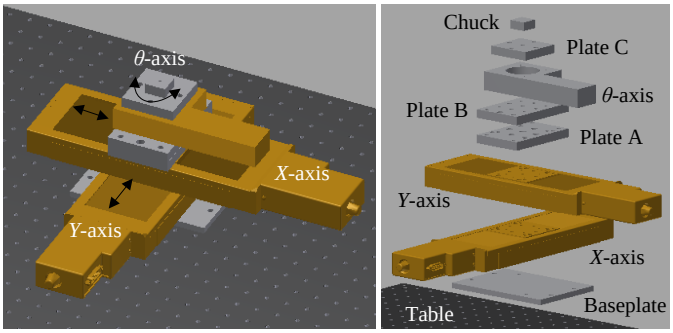

Figure 5.16. Kinematic assembly of the $XY\theta$ manipulator.

Figure 5.17 shows how in general two parts are mated together in assembled mechanisms. Two plates, one having a screw hole and the other one having the corresponding threaded hole, are fastened together with a screw. While doing this, the alignment between the two plates may not be perfect due to the tolerances of the holes. Figure 5.18 illustrates the alignment errors introduced. These errors result in deviation from the designed kinematic configuration. In order to determine the bounding values of this deviation, we can model the misalignment errors using intervals and calculate their combined effect on the positioning of the end effector.

The maximum amount of translational misalignment $d_{\max}$ between the two plates in Fig. 5.18 can be formulated as

$$d_{\max} = (r_h - r_s) + \delta r_t \tag{5.1}$$

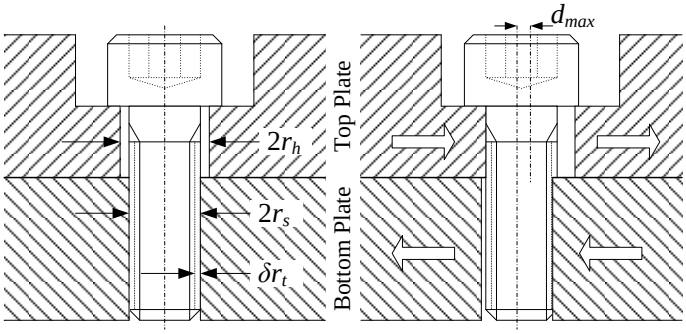

Figure 5.17. Perfect (left) and imprecise (right) fastening of fixture plates in an assembly.

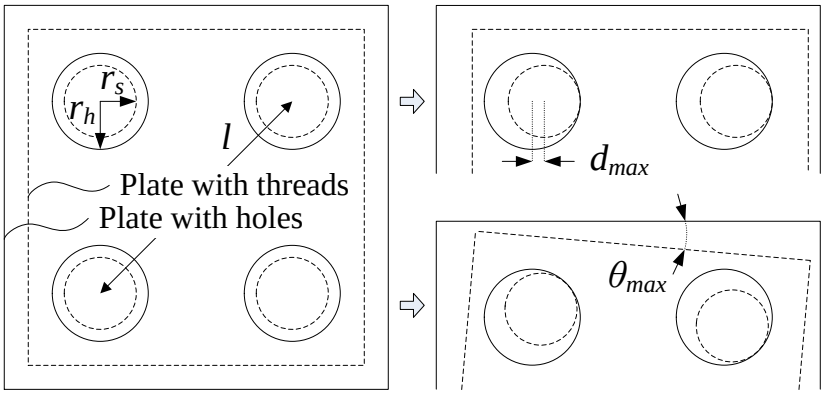

Figure 5.18. Errors involved in assembly of two plates.

where $r_h - r_s$ is the amount of play of the top plate around the screw and δr_t is the tolerance of the threaded hole in the bottom plate. Using $d_{\max}$, $\theta_{\max}$ can be found by a simple geometrical interpretation shown in Fig. 5.19 and calculated as in 5.2.

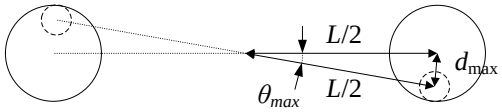

Figure 5.19. Geometrical analysis of maximum rotational misalignment.

$$\theta_{\max} = 2\sin^{-1}(\frac{d_{\max}}{l}) \tag{5.2}$$

Then, these maximum error values can be used to create the error transformation of mating plates as follows:

$$[T] = \begin{pmatrix} I_3 & [d] \\ 0 & 1 \end{pmatrix} \begin{pmatrix} [R]([\theta]) & \Big(I - [R]([\theta])q\Big) \\ 0 & 1 \end{pmatrix} \tag{5.3}$$

where the first term in the multiplication is the error transformation due to the translational tolerance whereas the second one is due to the rotational tolerance. $[d]$ is an interval vector such that $[d] = ([d_x] \quad [d_y] \quad 0)^T$. $[d_x]$, $[d_y]$, and $[\theta]$ are the intervals formed of the maximum deviations found in 5.1 and 5.2:

$$[d_x] = [d_y] = [-d_{\max}, d_{\max}] \quad [\theta] = [-\theta_{\max}, \theta_{\max}] \tag{5.4}$$

The rotational part $[R]([\theta])$ in (5.3) can be found using the formulation in (4.2). The variable q is the location of the center of rotation when the two plates misalign with respect to each other. This value can be taken as the midpoint of the two holes across which l is specified.

The procedure above can be carried out for all the fixture plates in the assembly and the total effect of these error sources can be found using the forward kinematics map. However, it should be noted that it is not the forward kinematics map of the manipulator but the combined effect of the homogeneous transformations described for each mating pair of plates as in (5.3). Below, we present this analysis considering three of the mating interfaces shown in Fig. 5.16: Base-Plate to Optical Table, X-Axis to Y-Axis, Plate-B to Plate-A. Fig. 5.20 shows part of the system with the $XY\theta$ manipulator and the overhead microscope camera. The camera is focused on

the sample holder (end-effector) of the manipulator and can measure its pose (x, y, ψ) with a resolution of about $4\mu m$.

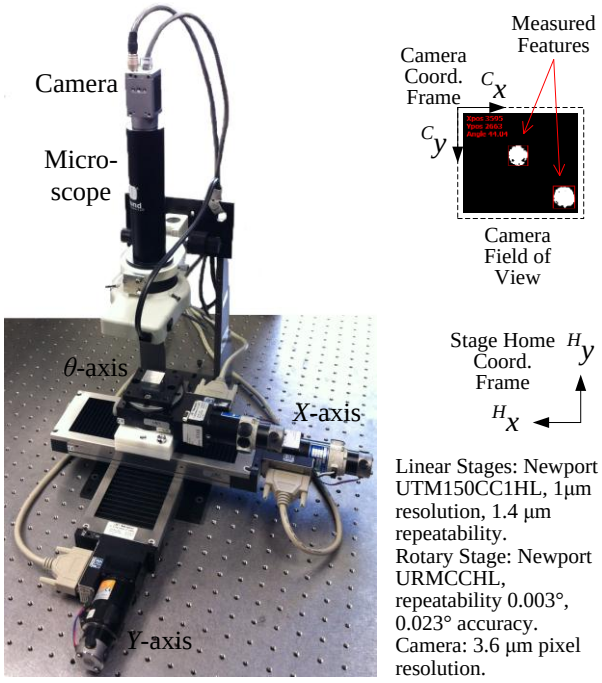

Figure 5.20. The image-based measurement system.

The first step is to list the necessary dimensions of each assembly mates as in Table 5.4. These are the values specified in the datasheets of the fixture plates and the corresponding standard screw sizes. Then, equation (5.4) can be evaluated for each pair of mates as in Table 5.5.

Table 5.4. Tolerances in fixture plates and corresponding error intervals (mm)

Mates	$2r_h$	$2r_s$	δ_t	l	q
Base Plate/Table	6.80	6.33	0.15	152.40	(1.731, 1.221, 0.0)
X-Axis/Y-Axis	3.60	3.00	0.10	89.10	(1.731, 0.121, 0.0)
Plate-B/Plate-A	6.87	6.33	0.15	113.59	(0.231, 0.121, 0.0)

Table 5.5. Error intervals corresponding to tolerances in (5.4

Mates	$[d]$ (mm)	$[\theta]$ deg
Base Plate/Table	$[0.39, 0.39]$	$[0.292, 0.292]$
X-Axis/Y-Axis	$[0.40, 0.40]$	$[0.511, 0.511]$
Plate-B/Plate-A	$[0.42, 0.42]$	$[0.427, 0.427]$

)

We find the total error transformation as in (5.5). This transformation can be applied to any point in the workspace of the manipulator to obtain the bounds of the uncertainty in the positioning of the end-effector due to fixture tolerances. In order to compare the result with the real case, we drive the manipulator to a known encoder position and use the microscope image to record the end-effector pose with respect to the camera reference frame. Then, we repeat this by disassembling and reassembling the fixture plates listed in Table 5.4 so that the fixture errors change. By recording many readings this way, a distribution of end-effector points is obtained in the XY plane as shown with filled dots in Fig. 5.21. The average of that distribution is found to be $p_0 = (3.82,\ 3.11,\ 0)^T$. If the error transformation is applied to this point as in (5.5), an interval position vector, P, is obtained that encloses all the point results as shown in Fig. 5.21(a). Similarly, Fig. 5.21(b) shows that this error transformation causes an angular deviation of about 2 degrees at the end-effector.

$$[P] = T_1 T_2 T_3 p_0 =$$

$$\begin{pmatrix} [0.9997, 1.0002] & [-0.0215, 0.0215] & 0 & [-1.2262, 1.2263] \\ [-0.0215, 0.0215] & [0.9997, 1.0002] & 0 & [-1.2439, 1.2439] \\ 0 & 0 & 1 & 0 \\ 0 & 0 & 1 & 1 \end{pmatrix} \begin{pmatrix} 3.82 \\ 3.11 \\ 0 \\ 1 \end{pmatrix} \tag{5.5}$$

$$= \begin{pmatrix} [2.53, 5.12] \\ [1.79, 4.44] \\ 0 \\ 1 \end{pmatrix}$$

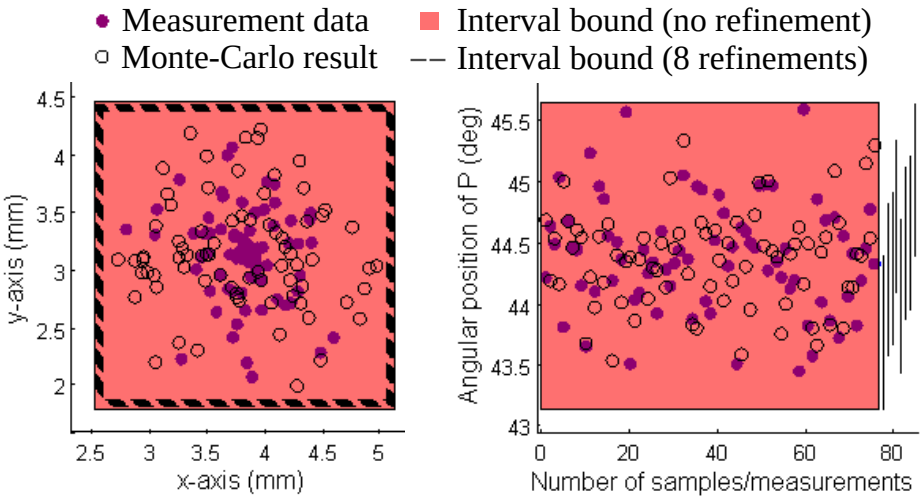

(a) XY position (b) Angular position

Figure 5.21. End-effector position measurement data in the 75 disassembly-reassembly experiments and the interval bounds.

Fig. 5.21 shows that the experimental data and the Monte-Carlo simulation results are similarly distributed, confirming the accuracy of the error model. The result of our interval method based on this error model totally encloses all experi-

mental and Monte-Carlo results as expected. Also shown in Fig. 5.21 with dashed boundaries in (a) and solid lines in (b) are the results of the interval method with 2^3 refinements in $[\theta]$. Fig. 5.21(a) shows 8 dashed boxes almost overlapping with each other, enclosing slightly smaller areas than the interval result without refinement. Similarly, Fig. 5.21(b) shows 8 vertical lines spanning almost the same total range as the interval result without refinement. These observations mean that the interval extension function in (5.5) does not cause too much overestimation hence refinement cannot improve the result significantly.

In MATLAB/INTLAB, the average computational time required for the evaluation our interval formulation in 5.3-5.5 is 11ms on an Intel i5 2.67GHz computer. Evaluation of the point-valued equations via Monte-Carlo sampling requires 0.66ms per sample. Performing 75 sampling operations as in Fig. 5.21, for instance, takes about 50ms. However, it must be recognized again that no finite number of Monte-Carlo samplings can provide the guaranteed bound that we obtained via only one interval evaluation in Fig. 5.21.

5.6 Chapter Conclusions

Microassembly robots have to be designed and developed according to the particular requirements of the aimed task. This introduces the need for custom design of manipulators using basic motion control elements such as linear and rotary stages. Selection and assembly of these stages must be done with prior knowledge of the predicted precision of the assembled manipulator. Hence, a mathematical tool is needed to incorporate the error specifications of individual axes into the forward kinematics map of the manipulator. We have showed that interval analysis can be conveniently used for kinematic modeling of robotic manipulators with parametric uncertainties and errors. It very well fits into the product of exponentials formulation as a natural

extension to interval variables. The approach models uncertainties and errors as intervals and calculates the forward kinematics map using analytical and computational tools of interval analysis. This method can be applied to various problems such as tolerance analysis of a multi-axis stage assembly and precision evaluation of a manipulator with random axis errors. Experimental and simulation results verify that the estimated bounds successfully enclose volumetric end-effector pose error. This framework can be applied as a design tool for precision motion control systems and as yield prediction mechanisms for microassembly planning.

CHAPTER 6

PRECISION DESIGN OF MICROROBOTS

In the previous chapters, the exponential formulation of the forward kinematics map for serial manipulators was extended to intervals. This makes it possible to use interval analysis to find guaranteed precision bounds on the end-effector pose given the uncertainty of the kinematic parameters. Here, we use this formulation as an inclusion function in the computation of solutions to set-valued inverse kinematic problems. We propose a new method that can solve the inverse problem of bounding the allowable uncertainty in kinematic parameters of a manipulator based on given end-effector precision specifications. Besides precision machine designers, this method bears an importance for those roboticists who have to design a manipulator using elementary building blocks. For instance, custom design of multi-axis precision manipulators using individual single-axis stages is a common practice in the micro-assembly area [14, 45, 46]. The cost of such stages increase significantly with the increase in motion precision. For a given application, therefore, determining the level of precision required in each axis is an important yet insufficiently addressed consideration.

Simulation results are presented in a few case studies to illustrate how we can go from an uncertainty interval at the end-effector to a design domain of allowable uncertainties at individual joints and links. The proposed method can be used to determine the level of precision needed in the design of a manipulator such that a predefined end-effector precision can be guaranteed. Also, the approach is general as such it can be easily extended to any degree-of-freedom and kinematic configuration.

Computing the joint angles of a manipulator for a given end-effector pose is called inverse kinematics. There are two main types of solution to this problem: closed-form solutions and numerical solutions [103, p. 106]. Closed-form solutions are based on analytical expressions of the inverse relationship between joint angles and end-effector pose. Due to the complex nonlinear nature of robot kinematic equations, finding a closed-form solution is difficult in general. On the other hand, numerical solutions rely on the description of forward kinematics map and repeated evaluation of approximate joint angles until the desired end-effector configuration is sufficiently approached.

6.1 Inverse Kinematics with Joint Parameter Uncertainty

Consider the simple example shown in Fig. 6.1 where a two-link planar manipulator with revolute joints is depicted. The knowledge of the link lengths and joint positions are assumed to be uncertain to the extent denoted by δl_i and $\delta\theta_i$ for $i = 1, 2$, respectively. Given the nominal link lengths l_i and joint positions θ_i, the corresponding interval arguments can be expressed as

$$[\mathbf{x}] \triangleq \begin{pmatrix} [l_1] \\ [\theta_1] \\ [l_2] \\ [\theta_2] \end{pmatrix} \triangleq \begin{pmatrix} [l_1 - \delta l_1, l_1 + \delta l_1] \\ [\theta_1 - \delta\theta_1, \theta_1 + \delta\theta_1] \\ [l_2 - \delta l_2, l_2 + \delta l_2] \\ [\theta_2 - \delta\theta_2, \theta_2 + \delta\theta_2] \end{pmatrix}. \tag{6.1}$$

We showed in the previous chapters that the rotation part of the revolute joint transformation can be extended to intervals by using *Rodrigues' formula*.

$$R(\omega, [\theta]) \triangleq e^{\hat{\omega}[\theta]} = I + \hat{\omega}\sin([\theta]) + \hat{\omega}^2(1 - \cos([\theta])) \tag{6.2}$$

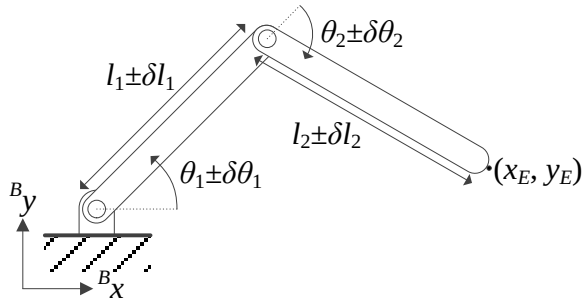

Figure 6.1. Two-link manipulator with uncertain link lengths and joint angles.

where $\omega = (0, 0, 1)^T$ is a real vector for the manipulator in Fig. 6.1. Then, the inclusion function for the transformation of the end effector pose can be written as

$$[\mathbf{f}]([\mathbf{x}]) = [T](\omega_1, [\theta_1], [q_1]) \cdot [T](\omega_2, [\theta_2], [q_2]) \cdot [\mathbf{f}]([\mathbf{x}_0]) \tag{6.3}$$

where

$$[T](\omega_i, [\theta_i], [q_i]) = \begin{pmatrix} R(\omega_i, [\theta_i]) & \Big(I - R(\omega_i, [\theta_i])\Big)[q_i] \\ 0 & 1 \end{pmatrix}. \tag{6.4}$$

Then, the inverse problem for this mapping can be posed as follows:

For a given interval of end-effector position $[\mathbf{y}] = [\mathbf{f}]([\mathbf{x}])$*, what should be the manipulator parameters* $[\mathbf{x}] = ([l_1], [\theta_1], [l_2], [\theta_2])^T$*?*

Note that the answer to the above question can provide not only the range of $[\theta_i]$ for the desired interval of end-effector position but also the maximum allowable uncertainty in $[\theta_i]$ and $[l_i]$. Therefore, this methodology can be used as a tool for precision design of manipulators. That is, determination of the required joint encoder resolution and of the manufacturing tolerance for the robot mechanism can be done based on the results of this inverse kinematic analysis.

When the kinematic mechanism is as simple as the one in Fig. 6.1, the point-valued inverse kinematics problem can be solved analytically as in (6.5) [103, p. 112]. These equations provide a couple of solutions for θ_1 and θ_2 for each end-effector position (x, y). However, as the number of joints increases, the forward kinematics

map becomes non-invertible. Also, incorporation of mechanism errors and parameter uncertainties introduces additional degrees of freedom to the formulation. Then, finding the inverse solution with interval arguments requires a set-based computational method. In order to address this problem, next we will introduce the use of a set inversion algorithm that is based on interval analysis.

$$\begin{aligned} \theta_2 &= \pm \cos^{-1}\left(\tfrac{x^2+y^2-l_1^2-l_2^2}{2l_1l_2}\right) \\ \theta_1 &= \operatorname{atan2}(y,x) \mp \cos^{-1}\left(\tfrac{x^2+y^2+l_1^2-l_2^2}{2l_1\sqrt{x^2+y^2}}\right) \end{aligned} \tag{6.5}$$

6.2 General Case of Inverse Kinematics via Set Inversion

Let $\mathbf{f}$ be the forward kinematics map of a serial manipulator from $\mathbb{R}^n$ to $SE(3)$ where n is the total number of joint variables and parameters that are uncertain. Also, let $\mathbb{Y}$ be a subset of $SE(3)$. Then, calculating $\mathbb{X}$ in (6.6) is the inverse kinematics problem in presence of joint parameter uncertainties for a given set of end-effector configurations. This is inherently a set inversion problem and can be addressed using SIVIA [93] that was introduced in Chapter 3.

$$\mathbb{X} = \{\mathbf{x} \in \mathbb{R}^n \mid \mathbf{f}(\mathbf{x}) \in \mathbb{Y}\} = \mathbf{f}^{-1}(\mathbb{Y}) \tag{6.6}$$

Application of SIVIA to a general inverse kinematics problem requires comparing $[\mathbf{f}]([\mathbf{x}])$ with $\mathbb{Y}$ and determining whether or not they intersect or one includes the other. This is relatively simpler if $\mathbb{Y}$ can be represented as an interval so that both $[\mathbf{f}]([\mathbf{x}])$ and $\mathbb{Y}$ are 4×4 interval matrices. Then, the comparison can be done element-wise. Otherwise, each member of $\mathbb{Y}$ has to be compared with $[\mathbf{f}]([\mathbf{x}])$ one by one.

6.3 Simulations

In this section, we present some example simulation results that show how the proposed method can be implemented. We carried out interval calculations using MATLAB and a toolbox called INTLAB developed by S. M. Rump [98]. INTLAB supports many operations with real and complex interval scalars, vectors, and matrices. It provides efficient functions for basic operations in algebra, trigonometry, etc.

In order to verify the results obtained using interval analysis, we also performed Monte Carlo analysis. When an analytical expression for inverse kinematics is available, it can directly be used to go from the configuration space to the parameter space. For instance, by evaluating equation (6.5) for various samples of the input arguments $[l_1]$, $[l_2]$, $[x]$, and $[y]$, one can obtain a set of points in the joint space whose convex hull approximately provides the inverse solution $\mathbb{X}$. We refer to this as the Monte Carlo solution in the next part.

6.3.1 *Precision Design of the Two-Link Manipulator*

In this part, we present the solution to the inverse kinematics problem of the two-link manipulator discussed in section 6.1. This serves as a validation example such that we verify the interval analysis results with Monte Carlo simulation of inverse kinematic equations. The results will enable us to determine the minimum joint encoder resolution required to achieve a given end-effector precision.

For the manipulator parameters given in Table 6.1 and for a sample end-effector position $([x], [y]) = (1.4 \pm 0.01, 1.2 \pm 0.01)$, the solutions of the SIVIA algorithm for a stopping criterion of $\varepsilon = \frac{\pi}{1800}$ is shown in Fig. 6.2. The picture on the left shows the 7018 subpavings (i.e. bisected arguments) of θ_1 and θ_2 each of which represent an interval sample from the joint space. SIVIA produces increasing concentration around

the two solution regions as it converges by bisecting initial 'undetermined' intervals. The exploded view of one of those regions on the right shows that the remaining undetermined region $\overline{\mathbb{X}}$ (yellow) found by SIVIA properly encloses the inverse Monte Carlo solution $\mathbb{X}$ (blue line) which in turn encloses the lower bound $\underline{\mathbb{X}}$ (green region) as suggested by SIVIA.

Table 6.1. Two-link manipulator simulation parameters.

l_1	δl_1	l_2	δl_2	$[\theta_1(0)]$	$[\theta_2(0)]$
1	0.001	1	0.001	$[0, \frac{\pi}{2}]$	$[-\frac{\pi}{2}, \frac{\pi}{2}]$

The result in Fig. 6.2 shows that if the joint positions can be addressed as precisely as to fit in the lower bound (green region, $\underline{\mathbb{X}}$), then it can be *guaranteed* that the end-effector can be positioned in the given interval $([x], [y]) = (1.4 \pm 0.01, 1.2 \pm 0.01)$. The question is then how to quantify the precision based on this result.

Fig. 6.3(a) shows $\underline{\mathbb{X}}$ in more detail where an interval of (θ_1, θ_2) with the largest overlapping area with $\underline{\mathbb{X}}$ is encircled. If the length of this interval along θ_1 is A and that along θ_2 is B, then the proper design choice for the joint resolution of the manipulator about these two axes can be described as in equation (6.7). This makes sure that the actual joint positions $[\theta_1] \triangleq [\theta_1 - \delta\theta_1, \theta_1 + \delta\theta_1]$ and $[\theta_2] \triangleq [\theta_2 - \delta\theta_2, \theta_2 + \delta\theta_2]$ can be commanded to be inside $\underline{\mathbb{X}}$ for a certain value of θ_1 and θ_2. This is explained pictorially in Fig. 6.3(b) with an arbitrarily positioned grid of addressable intervals each of which represents the set of actual joint positions for a given position command. When the condition in (6.7) is satisfied, there exists at least one interval of $([\theta_1], [\theta_2])$ that completely overlaps with $\underline{\mathbb{X}}$. In Fig. 6.3(b), there are five such possible joint positions shown by boxes with the slash pattern. Therefore, $\delta\theta_1^*$ and $\delta\theta_2^*$ are the coarsest resolution values for the joint encoders that guarantee the given end-effector precision.

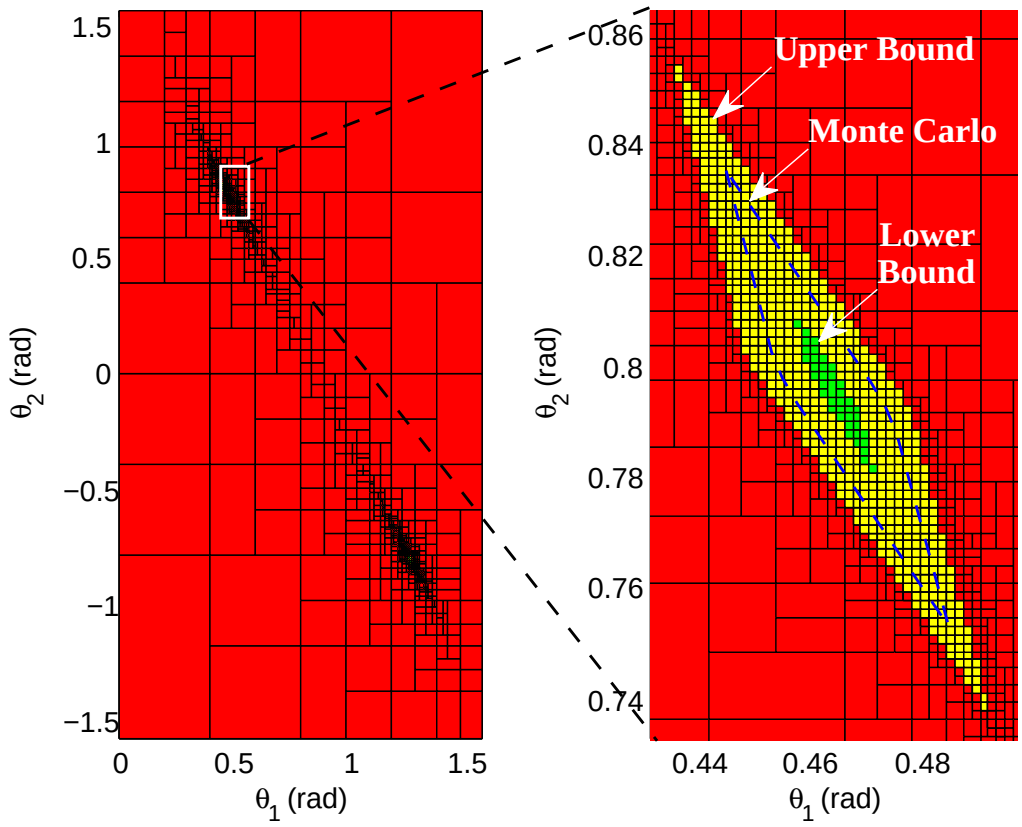

Figure 6.2. Bounds on θ_1 and θ_2 of the two-link manipulator for $([x],[y]) = (1.4 \pm 0.01, 1.2 \pm 0.01)$.

In this case, (A, B) is measured to be $(\frac{\pi}{900}, \frac{\pi}{450})$ which correspond to $(\delta\theta_1^*, \delta\theta_2^*) = (0.05\,\text{deg}, 0.1\,\text{deg})$. For this particular end-effector position, it can be seen that the resolution requirement for the first joint is higher as it can introduce more Abbe error due to its distance from the end-effector.

$$\delta\theta_1 \leq \delta\theta_1^* \triangleq \frac{A}{4} \quad , \quad \delta\theta_2 \leq \delta\theta_2^* \triangleq \frac{B}{4} \tag{6.7}$$

The lower bound $\underline{\mathbb{X}}$ can always be improved in expense of computational time by reducing the value of ε. Fig. 6.4(a) compares the previous result in Fig. (6.2) where ε was $\frac{\pi}{1800}$ with the one in Fig. 6.4(b) where ε is $\frac{\pi}{3600}$. It can be seen that a finer bisection resolution improves the lower bound $\underline{\mathbb{X}}$ towards the Monte Carlo result. The

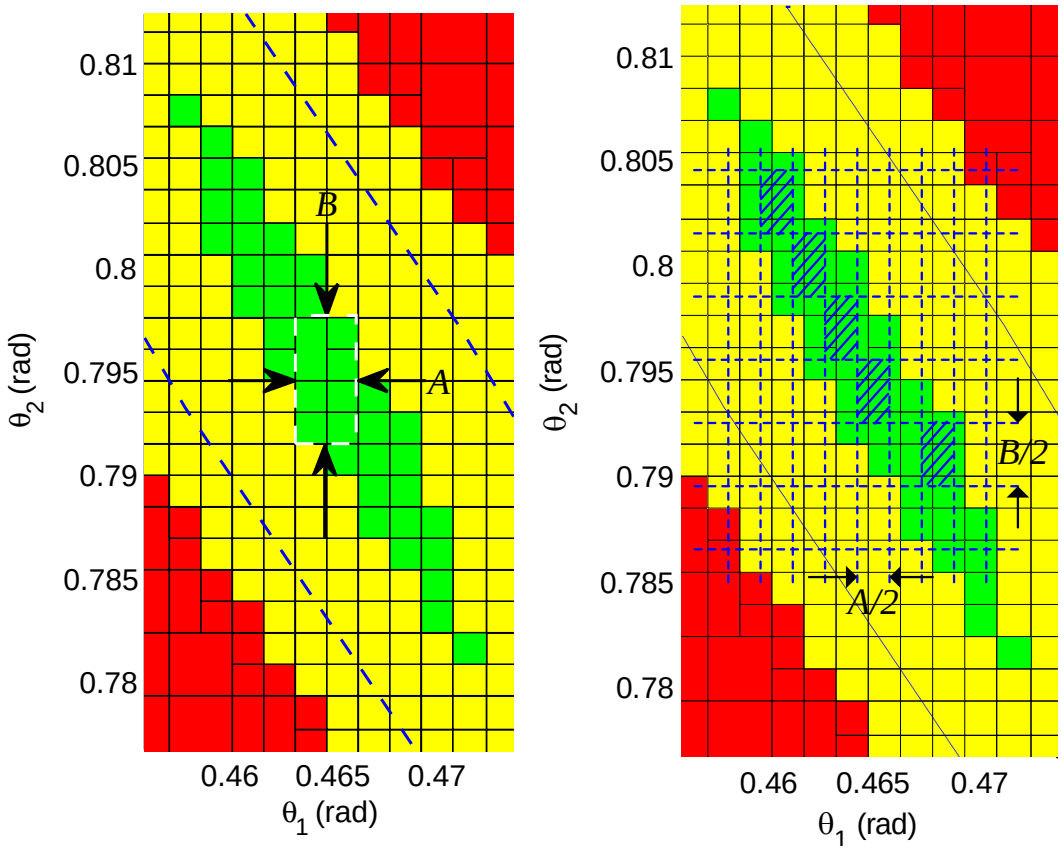

Figure 6.3. (a) Largest interval enclosed by the lower bound (b) An arbitrarily positioned grid of addressable intervals.

amount of improvement in this case is from $(A, B) = (\frac{\pi}{900}, \frac{\pi}{450})$ to $(A, B) = (\frac{7\pi}{3600}, \frac{\pi}{400})$ which means that the $\delta\theta_1^*$ and $\delta\theta_2^*$ are now 0.0875deg and 0.1125deg, respectively. The total number of subpavings processed in this case is 57590 which is significantly higher than the previous value 7018. Indeed, SIVIA terminates after generating less than $(\frac{width([\mathbf{x_0}])}{\varepsilon} + 1)^n$ bisections while the computing time increases exponentially with the dimension of $[\mathbf{x}]$ [104]. However, using bisections is one of the most basic techniques of interval analysis in terms of computational efficiency. There are efficient solvers that combine use of bisections, contractors, inclusion tests, and local optimization procedures to reduce the computational complexity to polynomial order [92]. Appli-

cation of these solvers to the inverse kinematics problem is not covered here but will be addressed in the future.

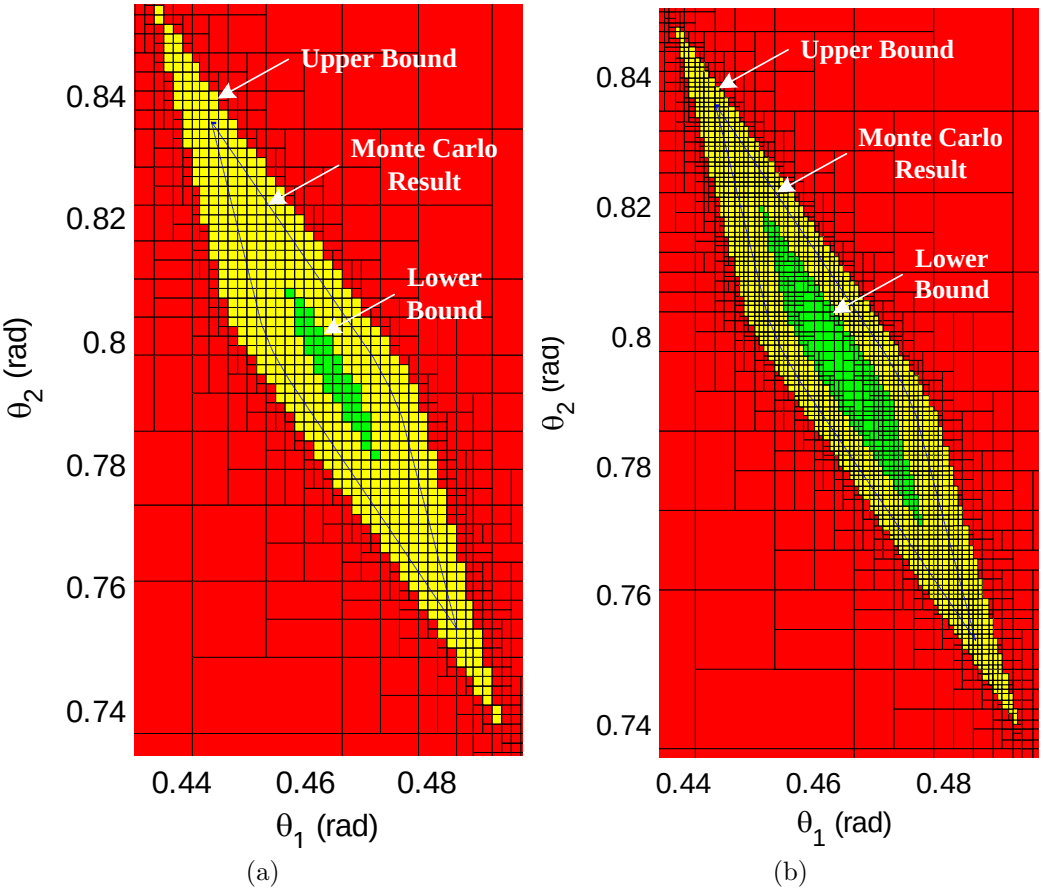

Figure 6.4. Upper and lower bounds found via SIVIA and set image found via Monte Carlo for (a) $\varepsilon = \frac{\pi}{1800}$ (b) $\varepsilon = \frac{\pi}{3600}$.

6.3.2 *Allocation of Mechanism Tolerances in a 3-DOF Precision Stage*

In this part, we will demonstrate how the presented method can also be used to allocate tolerances to the mechanical design of a 3-DOF PPR manipulator as in Fig. 6.5 such that a given end-effector precision can be achieved. For clarity, we will focus only on some of the parametric uncertainties of the manipulator such as prismatic

joint axes and rotary joint position vectors. The presented method will enable us to bound the allowable misalignment in these vectors. We assume that $[v_x]$, $[v_y]$, and $[q]$ have small error terms as shown in (6.8) denoted by $[\delta v_y]$ for the misalignment of $[v_x]$ along y-axis, $[\delta v_x]$ for the misalignment of $[v_y]$ along x-axis, and $[\delta q]$ for the misalignment of $[q]$ along x and y axes. In a practical scenario, for instance, these terms can represent the errors introduced into the geometry of the manipulator during its manufacturing or assembly.

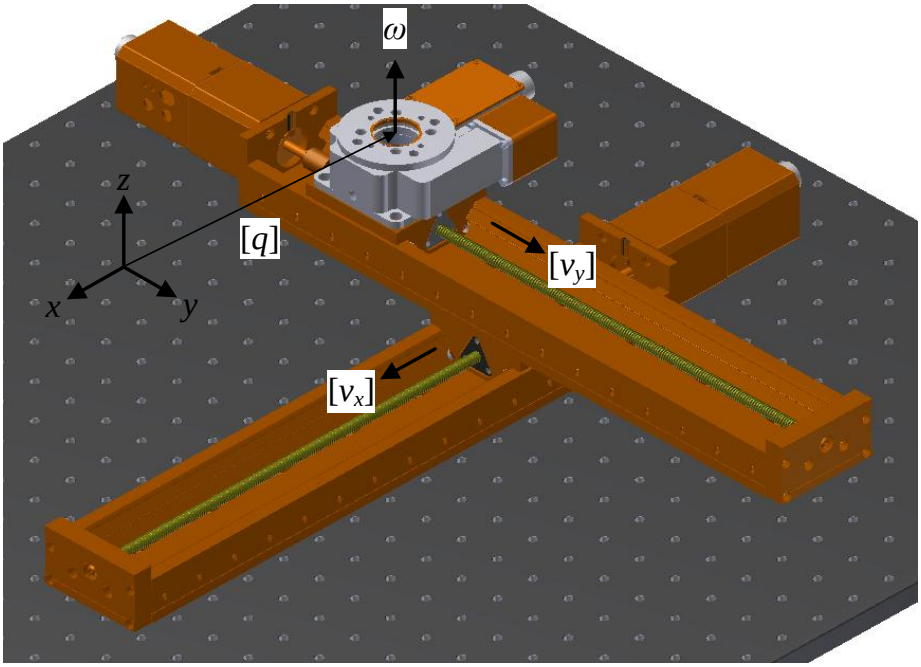

Figure 6.5. 3D model of a 3-DOF PPR precision motion stage.

$$[v_x] = \begin{pmatrix} 1 \\ [\delta v_y] \\ 0 \end{pmatrix} \quad [v_y] = \begin{pmatrix} [\delta v_x] \\ 1 \\ 0 \end{pmatrix} \quad [q] = \begin{pmatrix} [\delta q] \\ [\delta q] \\ 0 \end{pmatrix} \tag{6.8}$$

The objective in this simulation is to find how large $[\delta v_y]$, $[\delta v_x]$, $[\delta q_x]$, and $[\delta q_y]$ can be for a given stage positioning precision. For example, assume a configuration attached to the rotary stage needs to be driven from an initial pose p_i to a final pose p_f through the manipulator transformation that can be described as

$$[p_f] = \begin{pmatrix} I & d_x[v_x] \\ 0 & 1 \end{pmatrix} \begin{pmatrix} I & d_y[v_y] \\ 0 & 1 \end{pmatrix} \begin{pmatrix} e^{\hat{\omega}\theta} & (I - e^{\hat{\omega}\theta})[q] \\ 0 & 1 \end{pmatrix} p_i \tag{6.9}$$

where d_x, d_y, and θ are the desired displacements of the axes. We chose the initial end-effector position to be $(10\text{mm}, 0\text{mm}, 0\,\text{deg})$ and final joint position to be $(200\text{mm}, 400\text{mm}, 45\,\text{deg})$. Then, we solve for $[\delta v_y]$, $[\delta v_x]$, and $[\delta q]$ that guarantee a maximum deviation of 30μm from the desired final position. Fig. 6.6(a) shows the lower bound solution of this simulation. Similar to the previous case, the largest interval box that can be fit into the lower bound has approximate dimensions of (60,140,13) μm. Then, the allowable maximum uncertainty in the axes vectors can be expressed as

$$\begin{aligned} [\delta v_x] &= [-30, 30]\mu m \\ [\delta v_y] &= [-70, 70]\mu m \\ [\delta q] &= [-6.5, 6.5]\mu m \end{aligned} \quad . \tag{6.10}$$

Fig. 6.6(b) shows the distribution of end-effector position by sampling the intervals in (6.10) using Monte Carlo method. It can be seen that the results all lie inside the allowed boundary for final end-effector position hence (6.10) is a guaranteed tolerance allocation. It can also be seen in (6.10) that the amount of allowable uncertainty is different for different parameters. This depends on the given initial and final positions, desired stage positioning precision, and the kinematic design. Hence, the result can also be used to do sensitivity analysis to find out which parameter is likely to cause more deviation at the end-effector.

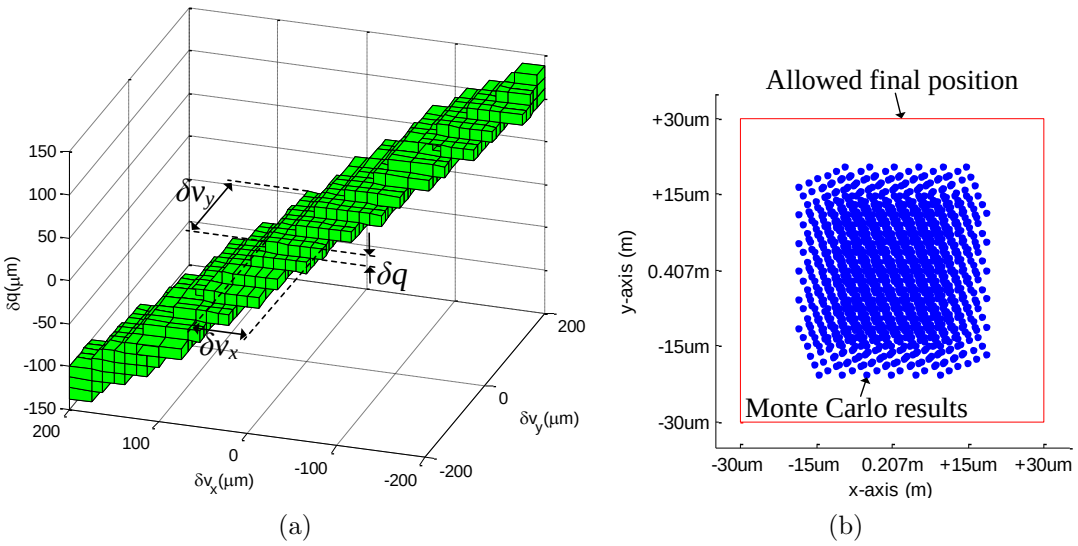

(a) (b)

Figure 6.6. (a) Bounding of error terms $[\delta v_y]$, $[\delta v_x]$, and $[\delta q]$ (b) End-effector position by Monte Carlo sampling of (6.10).

6.3.3 *Synthesis of Joint Sensor Resolutions for a 6-DOF Robot*

We consider the Puma 560 robot in Fig. 6.7 as a general example. The robot is shown in a zero-reference position with the joint axis vectors and positions denoted respectively by ω_i and q_i, $i = 1, \ldots, 6$. Table 6.2 gives the values of these parameters based on [32, p. 51]. In this simulation, we find the required joint sensor resolutions for a given task-space accuracy such as $100\mu m$. Since it is the first three joints that primarily determine the location of the end-effector in this type of a robot, we consider the required resolution for θ_1, θ_2, and θ_3.

We choose 27 nominal joint positions and find the required joint angle resolutions for an end-effector accuracy of less than $100\mu m$. The simulation result in Fig. 6.8 shows the manipulator links (blue lines) and the 27 task-space positions where green boxes represent the relative size of allowable joint uncertainties for the particular position. In order to make the boxes visible in the graph, their side lengths are magnified by a constant K that is 5×10^5 in this case. The found values of the

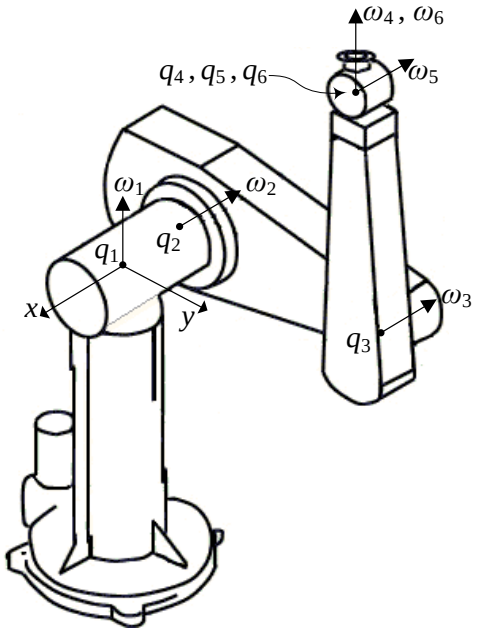

Figure 6.7. Puma 560 robot parameters in zero reference position.

allowable joint sensor errors for each task position are shown in Table 6.3 with $\delta\theta_1$, $\delta\theta_2$, and $\delta\theta_3$. If all joints can be addressed with an associated error less than $\pm\delta\theta_i$, then the end-effector can be position in the desired location with an accuracy less than $100\mu m$. Therefore, the required joint sensor resolution is given by $2 \times \delta\theta_i$. For instance, for joint position no. 20, the required sensor resolutions are 0.01, 0.01, and

Table 6.2. Joint vectors and positions of Puma 560

Joint	ω_x	ω_y	ω_z	q_x (mm)	q_y (mm)	q_z (mm)
1	0	0	1	0	0	0
2	-1	0	0	-149.09	0	0
3	-1	0	0	-149.09	431.85	0
4	0	0	1	-149.09	411.52	433
5	-1	0	0	-149.09	411.52	433
6	0	0	1	-149.09	411.52	433

0.005 degrees for axes 1 to 3, respectively. This requires 35986 counts per revolution for joint axis 1-2, and 71972 counts per revolution for joint axis 3.

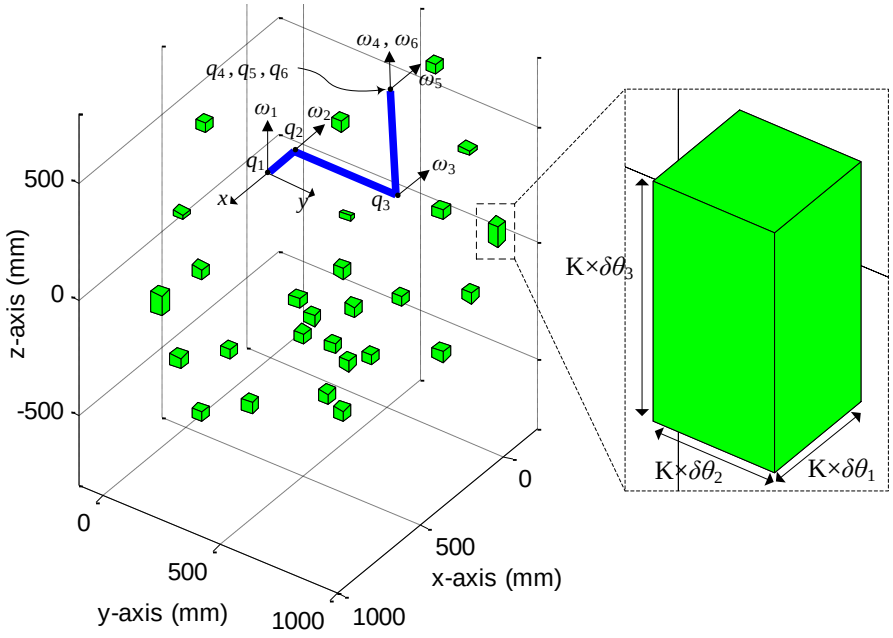

Figure 6.8. Joint error tolerances $\delta\theta_1$, $\delta\theta_2$, and $\delta\theta_3$ for various task-space positions.

6.4 Chapter Conclusions

In this chapter, we proposed a methodology for solving manipulator design problems with precision bounds. The simulation results show that the proposed method is effective in determining the level of precision needed in the design of a manipulator for a given end-effector precision. Solution of the inverse kinematics problem using interval analysis not only provides the range of joint space variables for a desired end-effector position but also allows calculation of the maximum allowable uncertainty in the joint sensor (encoder) feedback and the mechanism geometry tolerances. Therefore, the method can be used as a design aid in robotic applications that involve designing, building, or choosing individual axes of a multi-degree-of-freedom

manipulator. Since we use standard interval analysis tools such as SIVIA algorithm, our approach can easily be applied to any kinematic configuration. Future work will include using heuristics to speed up the computational efficiency of the algorithm and exercising this method on the design of a modular microassembly robot.

Table 6.3. Joint positions and the required joint sensor resolutions for an accuracy less than $100\mu m$

No	θ_1	θ_2	θ_3	$\delta\theta_1$ (mrad)	$\delta\theta_2$ (mrad)	$\delta\theta_3$ (mrad)
1	0	$-\frac{\pi}{4}$	$\frac{\pi}{2}$	0.0873	0.0873	0.0873
2	0	$-\frac{\pi}{4}$	$\frac{3\pi}{4}$	0.0873	0.0873	0.0436
3	0	$-\frac{\pi}{4}$	π	0.0873	0.0873	0.0873
4	0	0	$\frac{\pi}{2}$	0.0873	0.0873	0.1745
5	0	0	$\frac{3\pi}{4}$	0.0873	0.0873	0.0873
6	0	0	π	0.0873	0.0873	0.0873
7	0	$\frac{\pi}{4}$	$\frac{\pi}{2}$	0.0873	0.0873	0.0873
8	0	$\frac{\pi}{4}$	$\frac{3\pi}{4}$	0.0873	0.0873	0.0873
9	0	$\frac{\pi}{4}$	π	0.0873	0.0873	0.0873
10	$-\frac{\pi}{4}$	$-\frac{\pi}{4}$	$\frac{\pi}{2}$	0.0873	0.0873	0.0873
11	$-\frac{\pi}{4}$	$-\frac{\pi}{4}$	$\frac{3\pi}{4}$	0.0436	0.0873	0.0436
12	$-\frac{\pi}{4}$	$-\frac{\pi}{4}$	π	0.0873	0.0873	0.0873
13	$-\frac{\pi}{4}$	0	$\frac{\pi}{2}$	0.0873	0.0873	0.0873
14	$-\frac{\pi}{4}$	0	$\frac{3\pi}{4}$	0.0873	0.0873	0.0873
15	$-\frac{\pi}{4}$	0	π	0.0873	0.0873	0.0873
16	$-\frac{\pi}{4}$	$\frac{\pi}{4}$	$\frac{\pi}{2}$	0.0873	0.0873	0.0873
17	$-\frac{\pi}{4}$	$\frac{\pi}{4}$	$\frac{3\pi}{4}$	0.0873	0.0873	0.0873
18	$-\frac{\pi}{4}$	$\frac{\pi}{4}$	π	0.0873	0.0873	0.0873
19	$-\frac{\pi}{2}$	$-\frac{\pi}{4}$	$\frac{\pi}{2}$	0.0873	0.0873	0.0873
20	$-\frac{\pi}{2}$	$-\frac{\pi}{4}$	$\frac{3\pi}{4}$	0.0873	0.0873	0.0436
21	$-\frac{\pi}{2}$	$-\frac{\pi}{4}$	π	0.0873	0.0873	0.0873
22	$-\frac{\pi}{2}$	0	$\frac{\pi}{2}$	0.0873	0.0873	0.1745
23	$-\frac{\pi}{2}$	0	$\frac{3\pi}{4}$	0.0873	0.0873	0.0873
24	$-\frac{\pi}{2}$	0	π	0.0873	0.0873	0.0873
25	$-\frac{\pi}{2}$	$\frac{\pi}{4}$	$\frac{\pi}{2}$	0.0873	0.0873	0.0873
26	$-\frac{\pi}{2}$	$\frac{\pi}{4}$	$\frac{3\pi}{4}$	0.0873	0.0873	0.0873
27	$-\frac{\pi}{2}$	$\frac{\pi}{4}$	π	0.0873	0.0873	0.0873

CHAPTER 7

MOBILITY ANALYSIS AND CONTROL DESIGN FOR MICRO-AGENT SYSTEMS

We have been working on three different remote powering and control schemes that can be referred to as laser, vibration, and magnetic actuation. All three methods can be useful in controlled environmental settings for microassembly and micromanipulation purposes. Magnetic actuation, on the other hand, is particularly favorable for biomedical applications [47,105]. This chapter will mostly discuss laser-driven micro-agents as we have focused on that method the most. However, we had performed initial experiments with the other two types of micro-agents and we will present those results too. We propose to use pulsed laser as a source of energy and means of control for untethered micro-agents equipped with thermal microactuators. Achieving desired robotic operation with available controls in the laser signal is a challenge that requires concurrent design of micro-agent actuators with the spatial and temporal variables of the laser pulse. One approach can be via using spatial variables of the laser such as scan position and number of simultaneous spots. By scanning with the laser spot or using multiple lasers, multiple actuators of a micro-agent can be driven independently and simultaneously. This, however, requires a finely focused beam and fast scanning of multiple actuators which in turn requires a complex feedback control scheme. Alternatively, the temporal variables of a laser beam such as pulse frequency and duty cycle can be coupled by design to different modes of operation of the micro-agent so that multiple degrees of freedom can be driven with a single laser spot. In this case, the structural design of the micro-agent plays a critical role. We

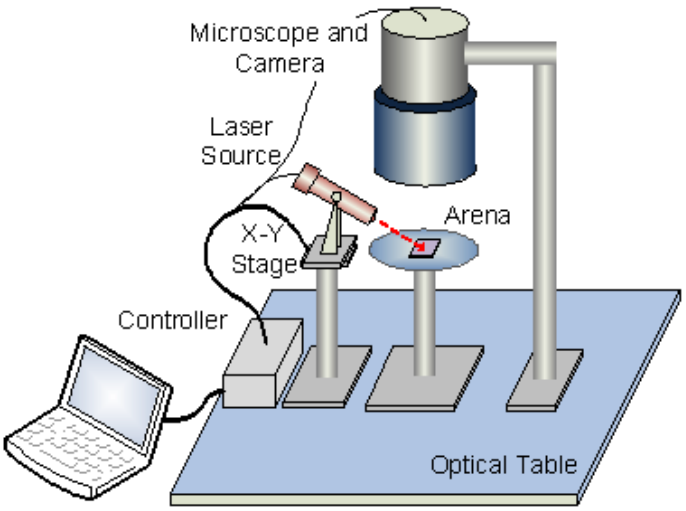

Figure 7.1. A typical remote power delivery and control system.

present micro-agent designs for generating stick-and-slip motion under pulsed laser excitation. A photo-thermal dynamic model of laser heat generation is developed and is used in the prediction of motion. It is shown through simulations that an appropriate selection of laser parameters along with a corresponding mechanical design can generate appropriate stick and slip motions resulting in 3-DOF (planar) operation for the micro-agent. Also, initial experiments on some micro-agent designs confirm generation of predicted type of stick-slip motion.

7.1 A Typical Micro-Agent System Description

A typical micro-agent control system can be depicted as in Fig. 7.1. For such as system, a basic control structure is given Fig. 7.2 where the flows of signals are indicated with arrows. We propose to address different degrees of freedom of a micro-agent by coupling its actuators with the spatial and temporal variables of an input power source such as frequency, amplitude, and directed power spot.

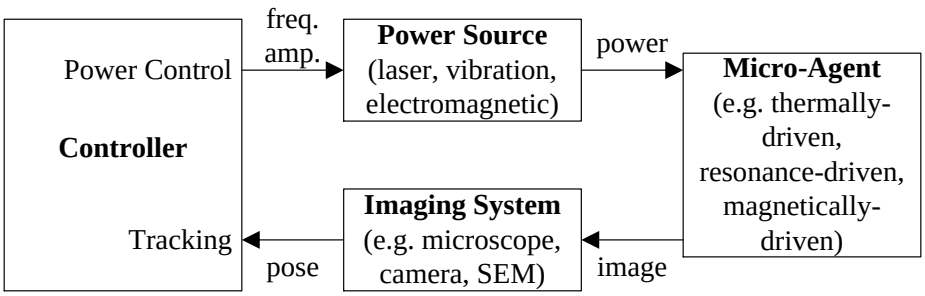

Figure 7.2. Remote powered micro-agent control system block diagram.

7.2 Laser-Actuated Micro-Agents: Initial Ideas

Our initial investigation on laser power delivery was focused on using a scanning laser spot to address simultaneously multiple actuators of a micro-agent. We proposed and evaluated two micro-agent designs, each equipped with thermal actuators of type either (pseudo) bimorph (hot/cold arm) or chevron (bent-beam). Due to the different powering method than the conventional means of Joule heating, the designs for these actuators were revised to attain optimal speed performance. We used parametric simulations in SUGAR [106] to determine the optimal values for the physical geometries of the two actuator designs. In this part, we provide the model details and analysis results for two micro-agents with different types of thermal actuators, namely the (pseudo) bimorph and chevron actuators. The electrothermal counterparts of such actuators have been thoroughly studied over the past couple of decades and the corresponding designs have matured [107, 108]. The analysis here is similar to the previous studies, but we do not use a current loop in the microstructures. As a reference point to our designs, we begin with conventional thermal actuator designs and change their dimensional parameters to arrive at a conclusion about the way they can be modified to maximize the actuation. This analysis uses the beam temperature as the input, rather than the actual laser power. As will be made clear in a later section of this chapter, this modeling approach is reasonable because actuator motion

is directly related to the temperature change caused by the laser irradiance. The following presentation of the micro-agent designs are based on the size constraints determined by NIST for the Mobile Microrobotics Challenge 2010 [109].

7.2.1 *Micro-Agent Mobility with Thermal Bimorph Actuators*

The basic design for the micro-agent with thermal bimorph actuators consists of four legs connected to a rectangular body as in Fig. 7.3. The principle of operation of the micro-agent with bimorph actuator legs is stick-and-slip motion. Heating the thin beam of the legs alternately and letting them cool down at the same time results in a forward motion gait pattern as shown in Fig. 7.3. Assuming that the heating and cooling rates of a leg are similar, the forward motion gait requires 4 simultaneous laser spots (or a very fast scanning laser) so that a leg that is heated and moved forward is kept there until all the remaining legs are heated as well and they cool at the same time to have a total step forward. Otherwise, if there is a single laser spot and if a leg that is heated and moved forward is left off the spot to heat the next leg, then the first leg is dragged back by the body due to premature cooling and its insufficiency to propel the whole body alone. The turning motion of the micro-agent can be obtained similarly by only heating the legs on one side as shown in Fig. 7.4.

7.2.2 *Micro-Agent Mobility with Chevron Actuators*

The chevron type actuators are known for their large output displacements and forces [108]. The design with chevron actuators here is inspired by the work in [110] along with some changes to the geometry as in Fig. 7.5. The principle of operation is again stick-and-slip motion. In this case, the micro-agent is composed of three feet, two of which being identical and different that the other in size (i.e. foot area). The larger foot, Foot A, is bigger than Foot B (1 or 2) and smaller than two times the size

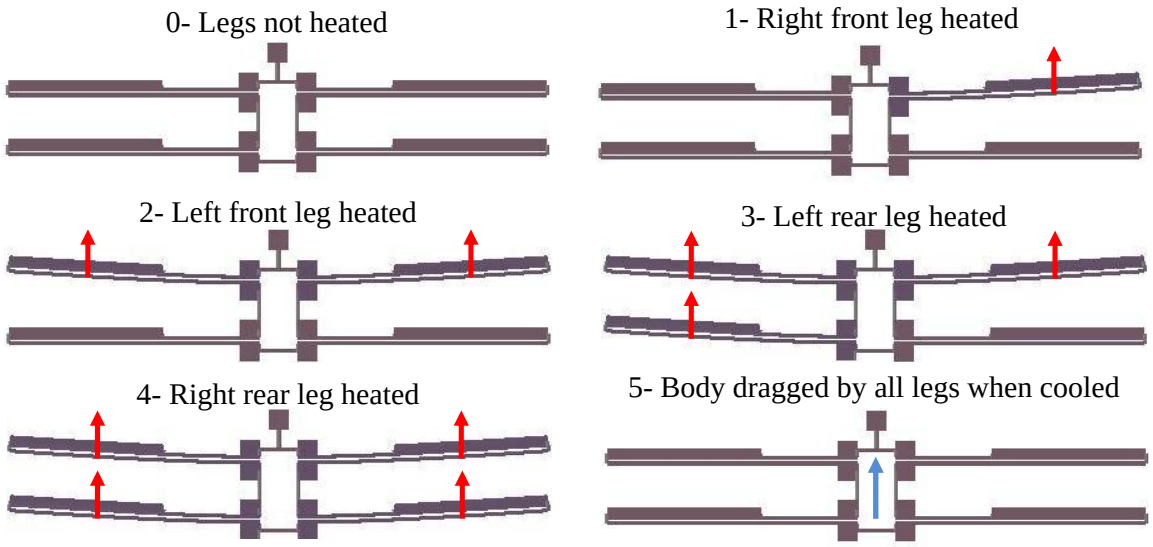

Figure 7.3. Forward motion gait of bimorph legged robot.

of Foot B. Mathematically, $2 \times mass(B) > mass(A) > mass(B)$. This is required to obtain the stick-slip motion shown in Fig. 7.6 and Fig. 7.7.

The forward motion gait of the micro-agent requires two simultaneous laser spots to heat both actuators simultaneously and let them cool down one by one. The principle is that, once again, two feet Bs can push foot A forward and a single foot B can be dragged by the cooling actuator that is connected to the larger total structure of feet A and B as in Fig. 7.6. Similarly a turning moment can be generated by simultaneous heating and cooling of two feet Bs as shown in Fig. 7.7. The operation in this case can explained as that after a single foot B is pushed backward by heating its actuator, letting it cool down and simultaneously heating the other actuator causes a moment around the center of the foot A.

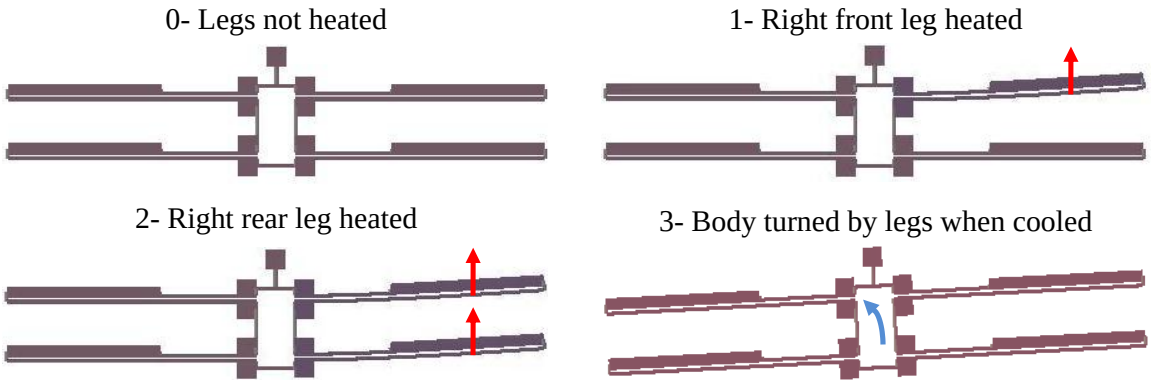

Figure 7.4. Turning gait of bimorph legged robot.

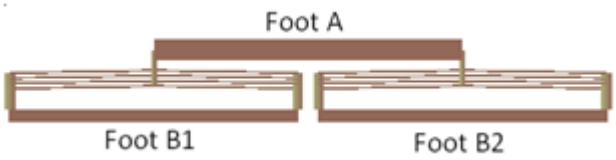

Figure 7.5. Three-feet micro-agent design.

7.3 Simulations of Thermal Micro-Actuators with Input Heat Spot

The dimensions of the two thermal actuators are optimized through simulations in order to obtain the maximum deflection, which is assumed to provide the highest speed for the micro-agents. Since this kind of an analysis requires a lot of simulation runs, SUGAR ([106]) is selected as the simulation tool, as it provides fast, yet sufficiently accurate nodal analysis. The steady-state responses of microactuators are individually analyzed with respect to applied input temperature at certain spots of the actuator beams. The assumption here is that the input laser power creates a temperature distribution around the laser spot and that can be approximated by the average temperature along the silicon beam subject to the laser. Actually, the distribution along the beam is typically similar to the one observed when is it heated by electric current [84] if the laser spot is on the center of the beam. Also, the level of

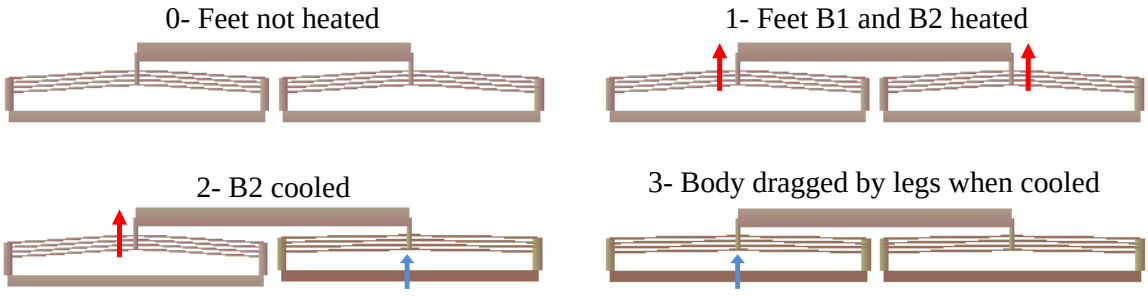

Figure 7.6. Forward motion gait of chevron feet robot.

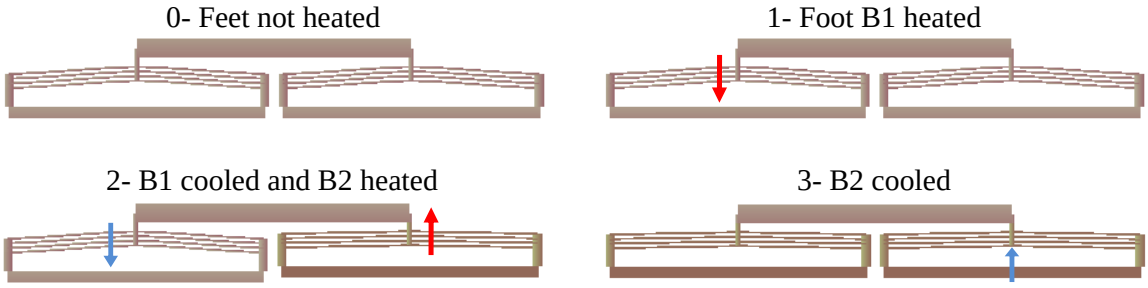

Figure 7.7. Forward motion gait of chevron feet robot.

the average temperature can be controlled because it is a function of the input laser power.

7.3.1 *Simulation of the Pseudo Bimorph Micro-Actuator*

There are some model parameters that need to be determined for the optimal performance of the bimorph actuator. Basically, the parameters are related with the physical dimensions of the bimorph. Fig. 7.8 shows these parameters pictorially. Determination of these parameters optimizing the actuator deflection (and hence the micro-agent speed) will be made by simulations. Table 7.1 lists the input parameters to the SUGAR model of the leg. We assume that the temperature of the thin beam (hot beam) is 4 times that of the thick and short beams (cold beams) due to thermal

conduction of the material and effect of nearby laser spot on those beams. Since the total width of the robot is limited to $600\mu m$, a single leg can be selected as $260\mu m$ long.

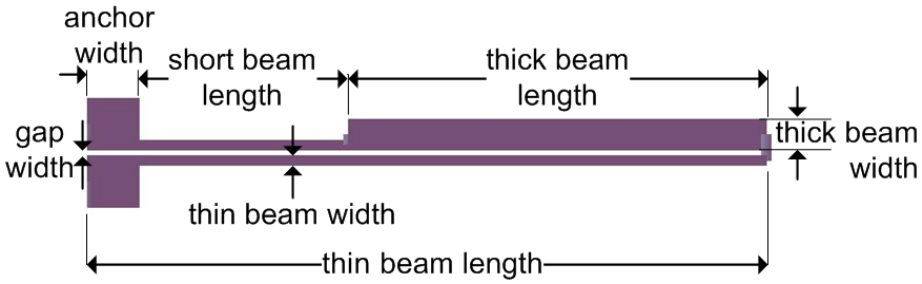

Figure 7.8. Model parameters of the bimorph actuator.

Table 7.1. Model parameters of the bimorph actuator

Parameter	Unit	Description
w-anchor	m	Width of the leg anchor
l-short	m	Length of the short beam
l-thick	m	Length of the thick beam
w-thick	m	Width of the thick beam
l-leg	m	Length of the leg (or thin beam)
w-thin	m	Width of the thin beam
w-gap	m	Width of the gap between beams
T-low	°C	Temperature of the thick and short beams
T-high	°C	Temperature of the thin beam

Figure 7.9a shows the variation of the deflection with respect to the width of the hot beam for the set of other parameters fixed. We conclude that the best result is obtained for 11m hot beam width. For the width of the gap between the hot and cold beams, the simulation results show that the smaller the gap the higher the deflection as in Fig. 7.9b. However, the process advice for minimum space is $2.5\mu m$

or above. Also, decreasing the gap width results in increased heat transfer through it, promoting temperature balance between the two arms. This effect is, however, dominant below $2\mu m$ [107].

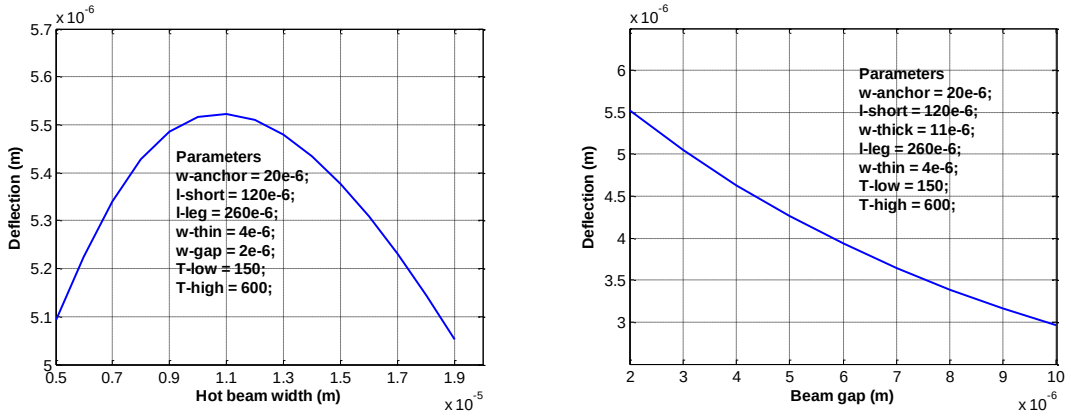

(a) (b)

Figure 7.9. (a) Deflection at the leg tip vs hot beam width (b) Deflection at the leg tip vs beam gap width.

The length of the short beam is also a parameter that we can optimize as shown by Fig. 7.10a, where the best value is found to be $100\mu m$. Note that this result is different than the optimal length of the short beam in electro-thermal bimorph actuators [107]. The reason is that the current flowing through the beams heats up the short beam more than the thick beam because its width is also small like the thin beam.

The width of the thin beam effects the deflection almost linearly toward the process limit as shown in Fig. 7.10b. It is not only the process that limits the minimum width of the thin beam but also the concerns on the stiffness of the beam and the efficiency of laser spot in heating it. First, a very thin beam might reduce the stiffness of the leg and result in out-of-plane buckling while being heated. Second, if

the laser spot will heat the beam by being directly shined onto it, the width of the beam would reduce the amount of power transferred if it becomes less than the laser focus diameter.

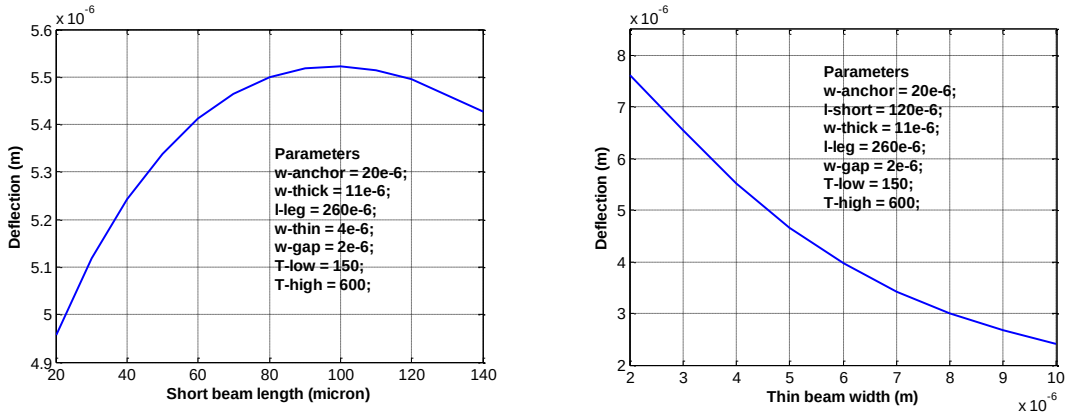

(a) (b)

Figure 7.10. (a) Deflection at the leg tip vs short beam length (b) Deflection at the leg tip vs thin beam width.

Finally, the forces that can be obtained by the optimal leg design are also investigated. We identify two types of forces that the bimorph actuator can generate. One is the force generated when it is heated up, referred to as the heating force. The other is the force that it generates in the other direction while cooling, referred to as the cooling force. The measurement of these forces at the tip of the leg is done in the simulation environment using an opposite, external balancing force input as shown in Fig. 7.11a. The force that can cancel the deflection of the tip at a certain temperature of the hot beam is assumed as the heating force at that temperature. Similarly, the force that can generate the same deflection at zero temperature as the deflection obtained under a certain temperature is assumed as the cooling force at

that temperature. We found out that the heating and cooling forces are slightly different as shown in Fig. 7.11b.

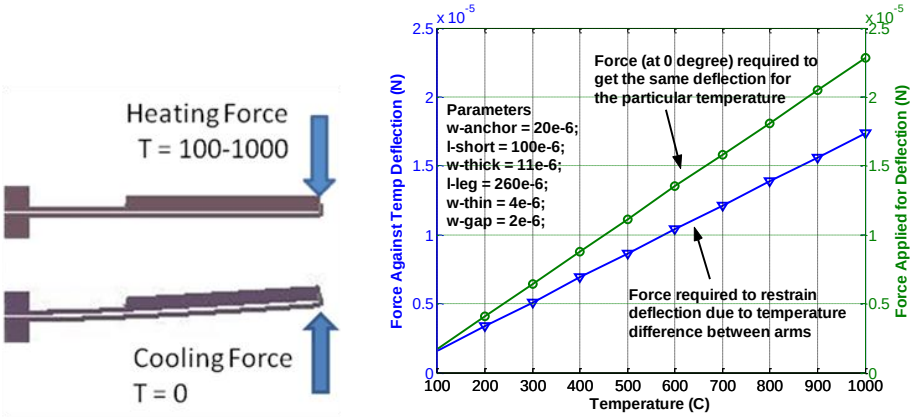

(a) (b)

Figure 7.11. (a) Heating and cooling forces of the bent-beam leg (b) Forces applied against and for deflection of the bimorph actuator.

7.3.2 *Simulation of the Chevron Micro-Actuator*

The basic parameters involved in the geometric model of the chevron actuator as in Fig. 7.12 are identified as in Table 7.2. Determination of these parameters will be made by simulations in SUGAR with the objective of maximizing the deflection at the tip of the actuator.

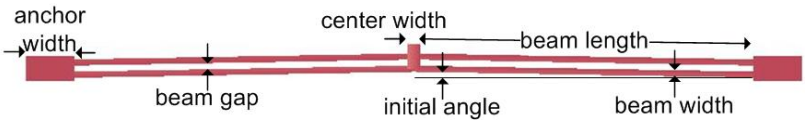

Figure 7.12. Model parameters of the chevron actuator.

Table 7.2. Model parameters of the chevron actuator

Parameter	Unit	Description
w-anchor	m	Width of the beam anchor
angle-Zero	rad	Initial angle of the beams
l-beam	m	Length of the beams
w-gap	m	Width of the gap between beams
T	°C	Temperature of the beams

Fig. 7.13a shows the deflection of the tip at 600 degrees (a typical value) versus the initial angle of the beams for three different beam widths. Relating this result with the result in Fig. 7.13b, where the deflection increases with decreasing beam width, we can conclude that the smallest beam width is limited with the process and that the best initial beam angle is around 1 degree.

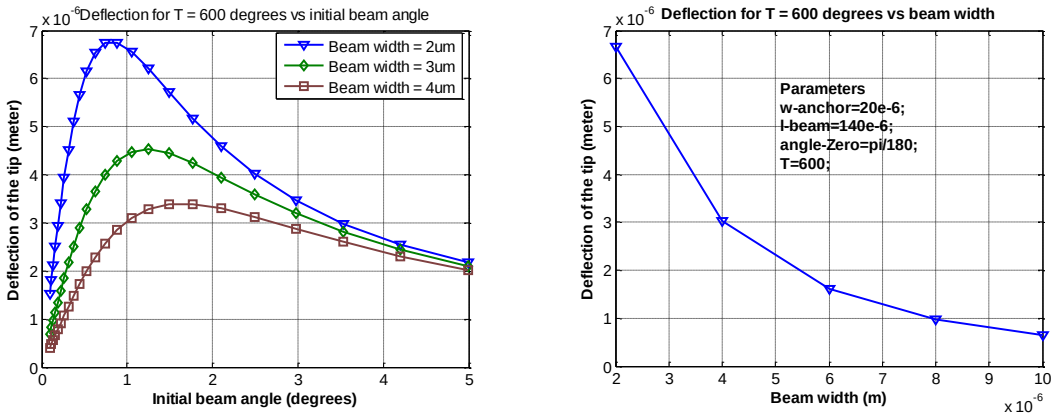

(a) (b)

Figure 7.13. (a) Deflection vs initial beam angle (b) Deflection vs beam width.

The force output of the chevron actuator is measured by using the external force method as shown in Fig. 7.14a. The force output of the actuator at the tip is linearly increasing with the temperature as seen in Fig. 7.14b. Similarly, the force

can be increased by increasing the number of beams in the actuator as shown in Fig. 7.15.

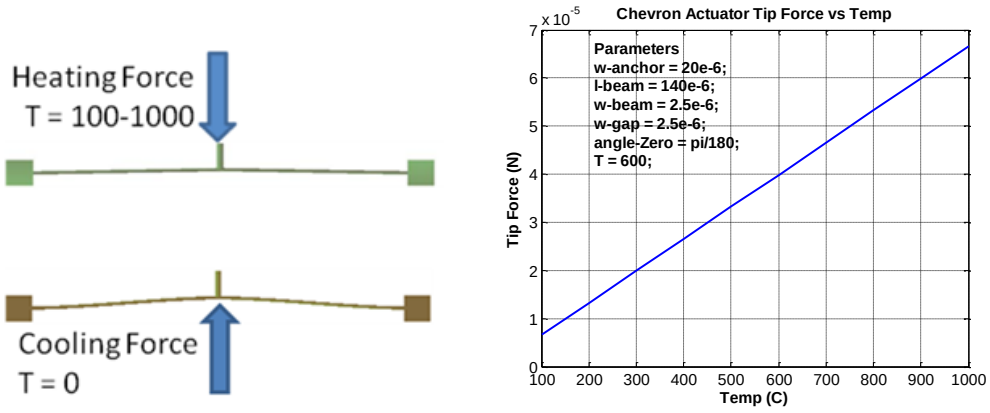

(a) (b)

Figure 7.14. (a) Heating and cooling forces (b) Tip force vs temperature.

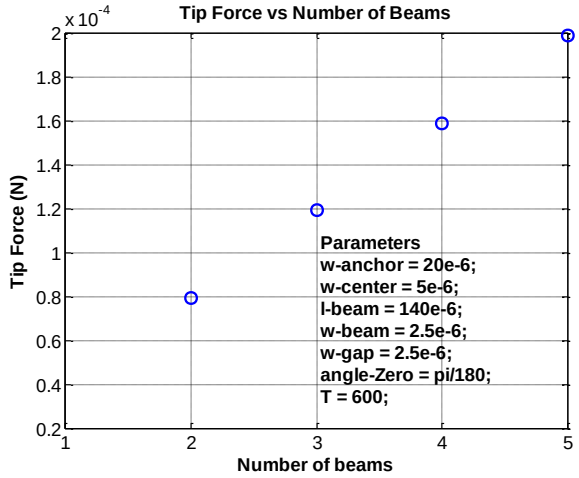

Figure 7.15. Tip force vs number of beams for the chevron actuator.

7.3.3 *Comparison of Bimorph and Chevron Micro-Actuators*

Deflection and force output characteristics of the two actuators and the possible speeds of the two micro-agent designs are compared. For the particular dimensions chosen as given in Table 7.3, Fig. 7.16a shows that the two actuators can achieve almost the same deflection . The force outputs of the two actuators are compared in Fig. 7.16b. It can be seen that the chevron type actuator provides considerably higher force output even with a single beam.

Table 7.3. Model parameter values of bimorph and chevron actuators

Bimorph	Value	Chevron	Value
w-anchor	$20\mu m$	w-anchor	$20\mu m$
l-short	$100\mu m$	angle-Zero	1°
l-thick	$140\mu m$	l-beam	$140\mu m$
w-thick	$11\mu m$	w-gap	$2.5\mu m$
l-leg	$260\mu m$		
w-thin	$4\mu m$		
w-gap	$2\mu m$		
T-low	$T_{low} = T_{high}/4$		

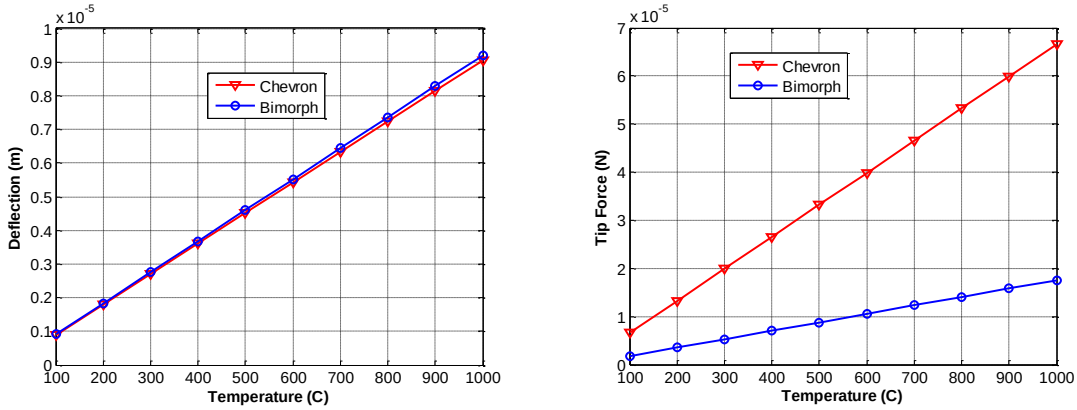

(a) (b)

Figure 7.16. Comparison of bimorph and chevron actuators (a) Deflection (b) Force.

7.4 Laser Experiments on a Chevron Micro-Actuator

In order to demonstrate the feasibility of using focused laser to power thermal microactuators, we conducted an initial experiment on a chevron type thermal actuator fabricated by DRIE on SOI wafers. We used the diode laser system (Coherent Quattro FAP™) and the setup shown in Fig. 7.17. It has 810nm wavelength with a 1mm spot size and can be dialed up to 12W. We attached the fiber coupled laser delivery optics to a 3-axis (XYZ) motion stage and positioned the laser spot over the center of the actuator shown in Fig. 7.18. It should be noted that the actuator is much larger than the MUMPS versions discussed in the previous sections.

The laser was aimed at the center of the actuator to allow symmetrical heating of the beams as shown in Fig. 7.19a. When the laser is turned on and off with a period of 1s and varying duty cycles between 3ms to 400ms, at power outputs below half of the hazardous level (e.g. the laser power melting the beams), the actuator was observed to shuttle with a varying maximum tip deflection Fig. 7.19b.

The result shown in Fig. 7.20 indicates the measured change of deflection with varying laser power duty cycle at two output power levels. Since the actual output power effectively transferred to the actuator depends on the surface conditions and is difficult to measure, the plot is given with reference to the power level that is observed to cause melting in the silicon beams. That level is designated by 10PmW where P is an undetermined factor less than 120 the maximum output power setting of the laser. Figure 48 shows that the actuator can be driven by laser up to its maximum deflection ($46.7\mu m$) without damaging it. $46.7\mu m$ is also very close to the maximum deflection when the actuator is powered by electrical current. Another important observation is that the maximum deflection is achieved at around 50ms of duty cycle regardless of the power level used. This shows that the steady-state deflection is achieved in

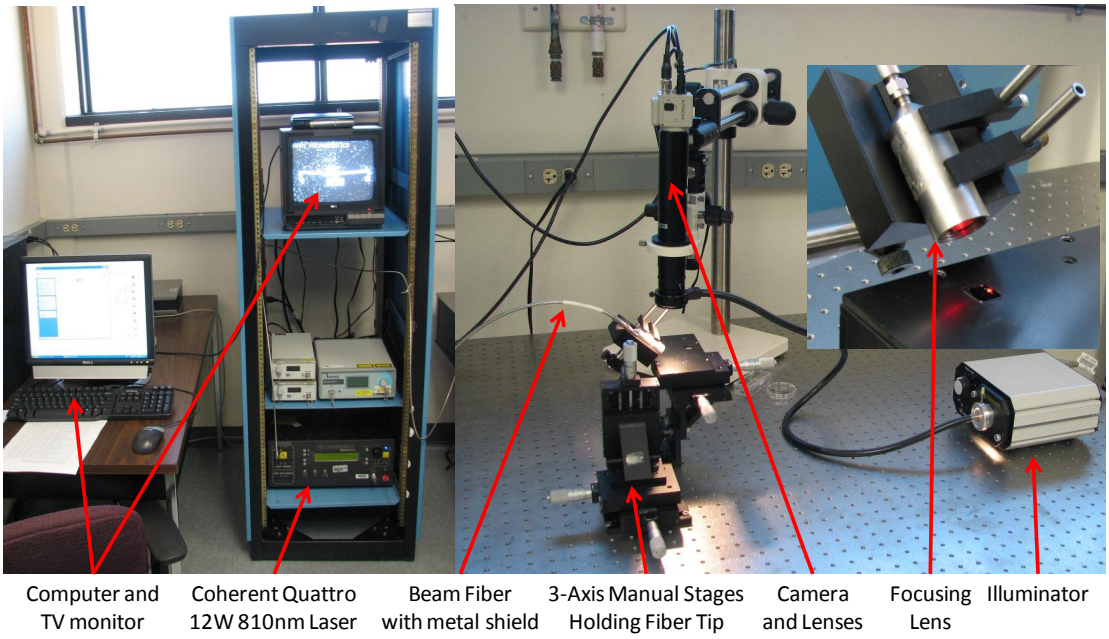

Figure 7.17. System for micro-actuator laser powering experiments.

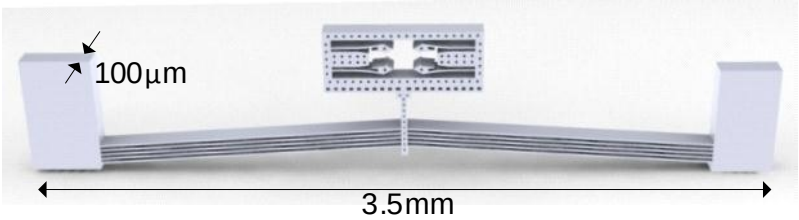

Figure 7.18. CAD drawing of the chevron actuator used in laser experiments.

about 100ms. Then, we can conclude that this thermal system has a time constant of about 20ms.

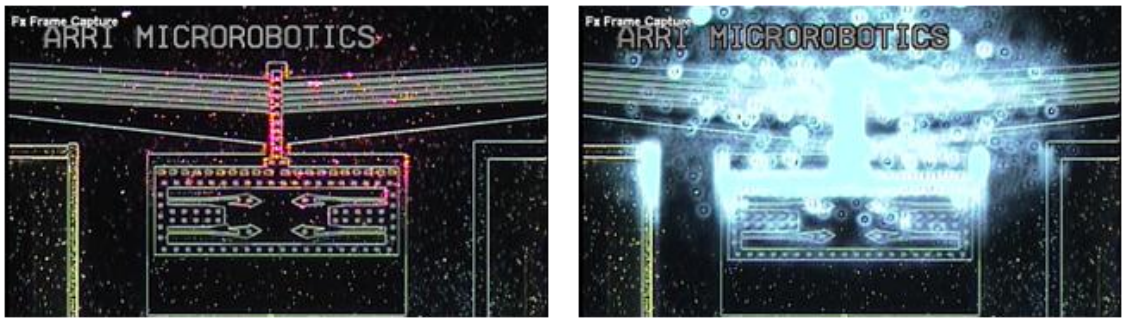

(a) (b)

Figure 7.19. (a) Red aiming beam centered on the actuator (b) Laser spot on the center of the actuator.

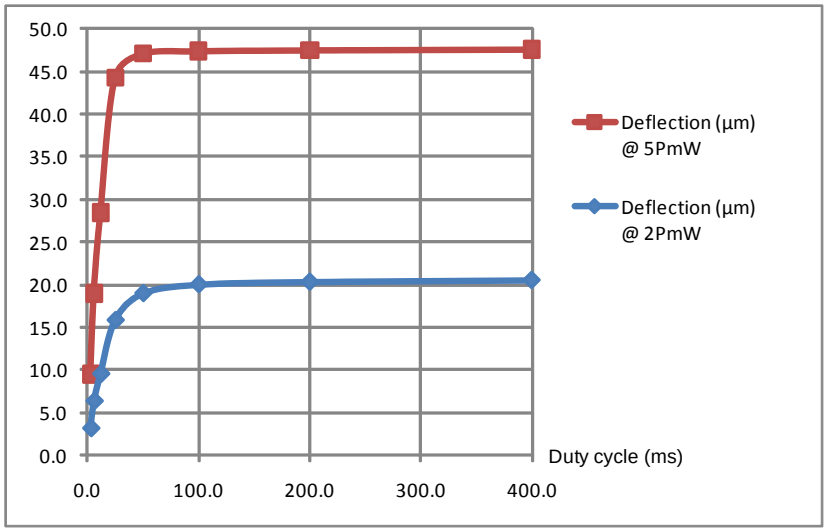

Figure 7.20. Measured deflection vs duty cycle at two power levels in reference to 10PmW (melting power).

7.5 3-DOF Mobility Using a Single Laser Spot

The drawback of the designs discussed earlier is the need to use multiple laser spots or to adaptively focus a single laser beam onto different (moving) robot legs, leading to a complex power and control delivery setup. In this part, instead of using multiple laser spots to thermally control the motion of multiple robot legs, we propose

to address different degrees of freedom (DOF) of a micro-agent using a designed coupling between the actuators of the agent and the temporal variables of the input laser such as frequency, pulse duty cycle, and intensity. In this way, a single laser spot that covers the whole body of the robot can be used to control its locomotion up to the designed degrees of freedom.

7.5.1 *Principle of Operation*

The micro-agent consists of an untethered chevron (i.e. bent-beam) microactuator that provides stick-and-slip motion under pulsed laser excitation. This $2\frac{1}{2}$D geometry can be fabricated using PolyMUMPS or SOI DRIE processes. As shown in the left of Fig. 7.21 (not to scale), the structure stands on a dimple and two feet over the substrate. This can be considered as a 3-point contact configuration. The chevron beams are attached to the body frame and shuttle, which is further connected to the legs and feet. The robot is driven by a laser beam of spot size greater than the size of the actuator. When the beams are heated, the expansion of the beams retracts the legs toward the body frame because the beams are initially bent toward right as in the left image in Fig. 7.21. One side of the body frame is coated with gold (Au-Cr film) to cause asymmetric heating of the actuators by laser, as the gold coating has high reflectivity. The other side is designed with a lower thermal resistance through to the substrate to cause asymmetric cooling. These two structural asymmetries create the differential dynamics of the expansion of the beams on each side of the shuttle and provide the rotational degree of freedom.

Figure 7.22 illustrates the operation of the locomotion mechanism from side view where the micro-agent is modeled as a double-mass-spring system. Since the beams are pre-bent toward the interior of the frame, their expansion shortens the total length of the micro-agent. Hence, when the laser turns on, it heats up the

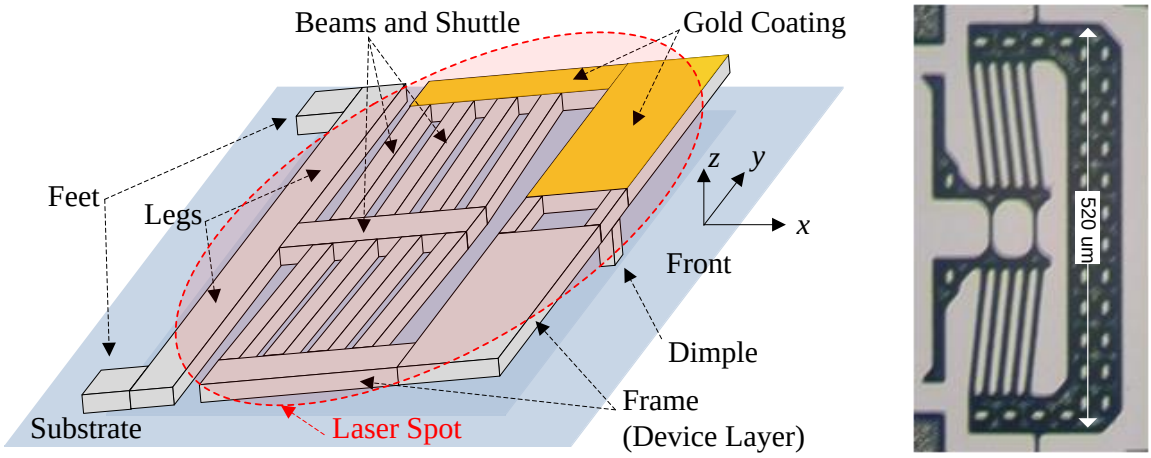

Figure 7.21. A sketch (left) and a microscope image from top of the fabricated 3-DOF micro-agent (right).

chevron beams which in turn pull the shuttle inward and retract the foot causing it to slip over the surface. The contraction of the micro-agent body in the heating cycle is represented by a shrinking spring in Fig. 7.22.

During the cooling cycle, the accumulated heat is dissipated through conduction to the substrate. Recovery of beams causes elongation of the micro-agent and sliding of the dimple forward, resulting in a net displacement. At each pulse of the laser, the micro-agent takes a step that is a proportional to the linear deflection of the actuator. Depending on the frequency of laser pulse, robot dynamics, and friction conditions, the effective step length changes.

Conventional chevron actuators are meant to provide linear motion. Due to the symmetry of the actuator geometry, the thermal expansion of the beams is symmetrical, and, as a result, the motion of the center shuttle is linear. In order to provide a rotational degree of freedom to the micro-agent, we propose a novel method of creating an asymmetry between the beams of the chevron actuator on each side of the

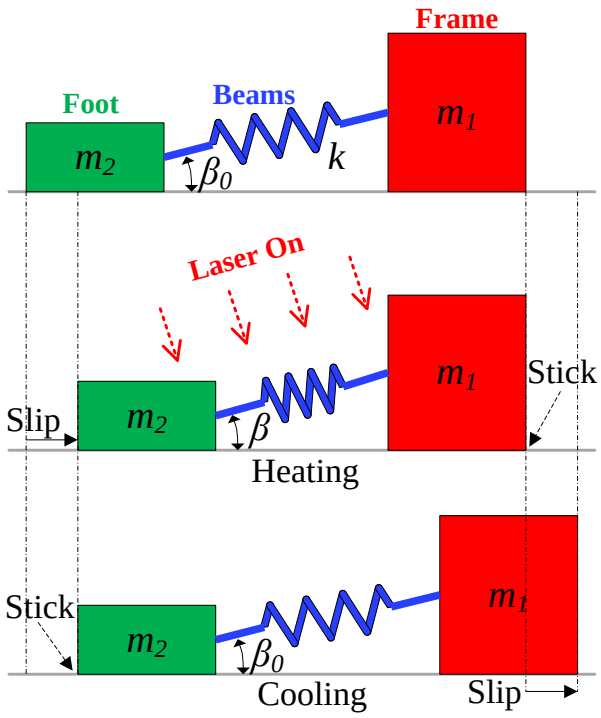

Figure 7.22. Stick-slip cycles of the micro-agent (side view).

shuttle. While the details of this frequency control method will be explained in Section IV, let us assume that we can differentially heat up the beams on different sides of the shuttle. This case is illustrated in Fig. 7.23 where from an initial temperature T0 the beams on the lower side are heated to T1 (red) and those on the upper side to T2 (orange) with a hypothetical thermal isolation along the center. The shuttle is designed to allow differential expansion of beams asymmetrically, which, in turn cause robot rotation while moving forward at the same time like a nonholonomic vehicle.

7.5.2 *Photo-Thermo-Mechanical Model*

The model of the micro-agent involves two main parts as shown in Fig. 7.24. The first one is the photo-thermal model which formulates the thermal dynamics of the micro-agent structure under laser irradiance G. Its output is the temperature

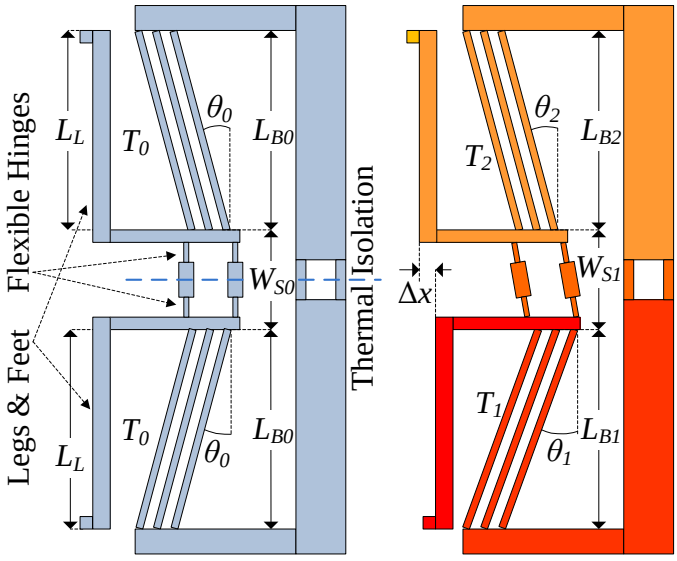

Figure 7.23. Differential heating of chevron beams causing rotational acceleration.

distribution T over the limbs of the micro-agent. Next, the thermo-mechanical model calculates mechanical response of the micro-agent due to thermal expansion.

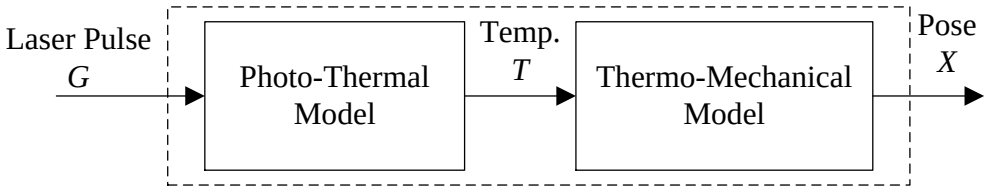

Figure 7.24. Mathematical model of the micro-agent.

7.5.3 *Photo-Thermal Model*

Generation of heat via a laser beam can be modeled using the photo-thermal model presented here. Understanding the factors affecting temperature distribution across micro-agent limbs is critical when designing its geometry so that desired mobility can be obtained. Depending on the optical properties of the illuminated material, the amount of power contained in an incident beam of light with irradiance $G\,(W/m^2)$

is partly absorbed (G_{abs}), reflected (G_{ref}), and transmitted (G_{tra}) [111]. According to Beers law [112], intensity of light that is not reflected exponentially decays while penetrating through a medium such that:

$$G_{tra} = (G - G_{ref})e^{-\alpha z} \tag{7.1}$$

where α is the absorption coefficient (m^{-1}) of the material and z is the distance into the medium. Since $G_{abs} + G_{ref} + G_{tra} = G$, the absorbed power is:

$$G_{abs} = (G - G_{ref})(1 - e^{-\alpha z}) \tag{7.2}$$

In order to visualize the heat generation profile, consider a laser source with 800nm monochromatic beam and $1\mathrm{MW/m}^2$ irradiance directed on an intrinsic silicon sample at 300°K. For this case, reflectivity of silicon is known to be around 0.3 and absorption coefficient to be $10^5\mathrm{m}^{-1}$ [113]. Based on equation (7.2), Fig. 7.25 shows that 95% of the volumetric heat generation takes place within the first 30 μm of the depth of silicon. Therefore, since the thickness of the micro-agent is 10 μm, then the vertical gradient of the temperature can be neglected. This approximation is valid if the Biot number of the structure is less than 0.1 [111]. For the micro-agent shown in Fig. 7.25, the Biot number can be calculated using equation (7.3) where h is the heat transfer coefficient, L_c is the characteristic length (thickness), and k_{Si}, k_{air} are the thermal conductivity of Si and air, respectively.

$$Bi \triangleq \frac{hL_c}{k_{Si}}, \quad h \approx \frac{k_{air}}{\delta z} \tag{7.3}$$

The characteristic length of the micro-agent structure is 10 μm. The heat transfer coefficient h is dominated by the heat exchange between the microstructure and the substrate as the temperature gradient through the thin film of air is relatively

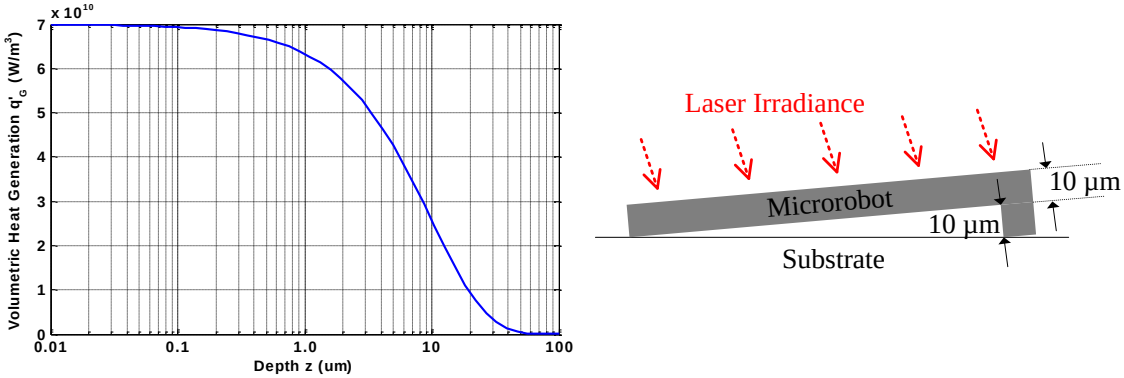

Figure 7.25. Heat generation through Si under laser irradiance.

very high. Therefore, it acts like a conductor and the heat transfer coefficient is given by $\frac{k_{air}}{\delta z}$. If we take an average of 5 μm for δz and use the conductivity constants for $k_{Si} = 130$ W/m.K, $k_{air} = 0.026$ W/m.K [111] we can find the Biot number as 4×10^{-4}, which is well below 0.1. Then, it can be reasonably assumed for the micro-agent that the absorbed laser radiation creates an average volumetric heat generation Q_L through the depth H of the microstructure given by (7.4), reducing the problem geometry to a plane.

$$Q_L = \frac{\delta G_{abs}}{\delta z} \approx \frac{G_{abs}(H)}{H} = (G - G_{ref})\frac{(1 - e^{-\alpha H})}{H} \tag{7.4}$$

In order to make the problem analytically tractable, we use the concept of control volume depicted in Fig. 7.26 in which temperature distribution is assumed to be uniform. Then, certain parts of the micro-agent can be lumped and modeled approximately as control volumes. The Fourier law of conduction given in (39) governs heat flow in solids and provides a quantitative way to predict the temperature distribution over an interconnected system of volume elements [113].

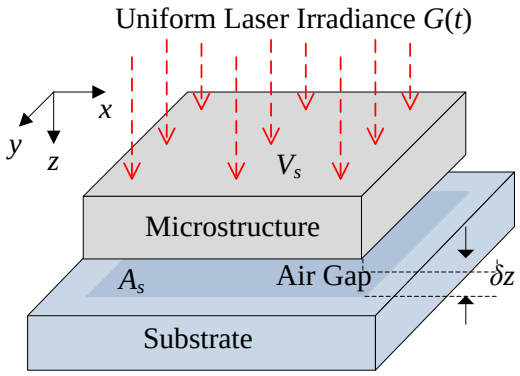

Figure 7.26. Heat transfer control volume.

$$\nabla \cdot (k\nabla T) + Q_L = \rho c_v (\frac{\partial T}{\partial t}) \tag{7.5}$$

In equation (7.5), k is the thermal conductivity (W/m.K), ρ is the density (kg/m^3), and c_v is the specific heat (J/kg.K) of the material. The effect of volumetric heat generation due to laser is contained in the input Q_L (W/m^3). Among the forms of heat loss, radiation and free convection were shown to be negligible when compared to conduction for a thermal microactuator [114]. Since the micro-agent stands on its dimple and foot and there is a very thin air gap underlying it, the heat loss is mostly due to the heat flow through the bottom surface of the structure as well as through the contact points [115].

The general boundary condition for convective heat transfer is given by Newton law of cooling, and depends on the difference between T, the control volume temperature (K), and the temperature at the far ambient T (assumed to be the constant substrate temperature) as in (7.6) [112].

$$q_{conv} = (T - T_\infty) k_{air} \frac{A_e}{\delta z} \tag{7.6}$$

where q_{conv} represents the convective heat loss through A_e, the effective area of the control volume. An adjustment is needed to find the effective area Ae through the dimensionless shape factor S that was empirically formulated by [115] such that

$$A_e = S\,A_s \quad S = \frac{H}{W}(\frac{2\delta z}{H} + 1) + 1 \tag{7.7}$$

where H and W are the thickness and width of the microstructure, respectively, and A_s is the differential surface patch facing the substrate. Similarly, the conductive heat transfer from control volume to its neighbors indexed with j is given by

$$q_{cond} = \sum_j (T - T_j) k_{Si} \frac{A_j}{\delta x_j} \tag{7.8}$$

where A_j is the contact area between the control volume and its neighbor j, δx_j is the mean distance between them, and k_{Si} is the thermal conductivity of Silicon.

We can use lumped approximations for certain sections of the micro-agent where the structure is likely to have uniform control volume parameters such as air gap. Assuming that the spatial temperature distribution and the heat transfer coefficient over each of these sections are constant, we can use the control volume representation in Fig. 7.26 and find a first order model for the corresponding heat-capacity system. Then, we connect each of these first-order systems to create a thermal network based on the electrical analogy as in Fig. 7.27 and 7.4 [113].

Table 7.4. Analogy between thermal and electrical systems

Thermal (unit)	Electrical (unit)
T Temperature (°K)	V Voltage (V)
q Heat transfer rate (W)	I Current (A)
R Thermal resistance (K/W)	R Resistance (Ω)
C Thermal capacitance (J/K)	C Capacitance (F)

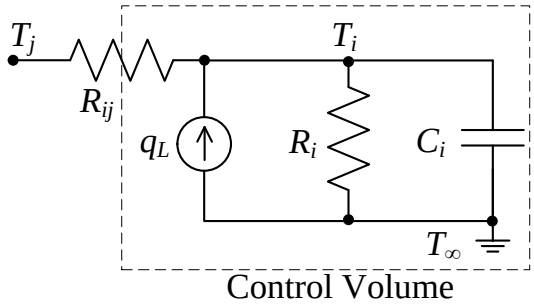

Figure 7.27. Electrical analog of the heat transfer control volume.

The current source in Fig. 7.4 corresponds to the total power injected into the control volume V_c by the laser beam. Throughout the control volume, the heat transfer coefficient ($h = \frac{k_{air}}{\delta z_{avg}}$) is assumed to be constant with δz_{avg} being the average value of the air film thickness underlying the control volume. The resistive element connected to the ground terminal, T, represent resistance to conduction to the substrate through the air film. On the other hand, that connected between T and T_j represents thermal resistance of the material to conduction as given in (7.9). Finally, the lumped dynamic model of the control volume can be written as in (7.10).

$$q_L = Q_L V_C\,, \quad R = \frac{\delta z}{k_{air} A_e}\,, \quad C = \rho c_v V_C\,, \quad R_j = \frac{\delta x_j}{k_{Si} A_j} \tag{7.9}$$

$$q_L - q_{conv} - q_{cond} = \rho c_v V_C \frac{\partial T}{\partial t} \tag{7.10}$$

Incorporating equations (7.6)-(7.10), we obtain (7.11). Obviously, this equation represents a first-order heat-capacity system with a time constant τ that is given as in (7.12). Consequently, the response of the temperature at each section of the micro-agent is governed by a time constant that depends on certain physical properties of that section.

$$\left(q_L + \frac{T_\infty}{R} + \sum_j \frac{T_j}{R_j}\right) = \left(\frac{1}{R} + \sum_j \frac{1}{R_j}\right) T + C\frac{\partial T}{\partial t} \tag{7.11}$$

$$\tau = R_{eq} C\,, \quad \frac{1}{R_{eq}} = \left(\frac{1}{R} + \sum_j \frac{1}{R_j}\right) \tag{7.12}$$

Based on the concept developed above, Fig. 7.28 shows the lumped partitioning of the micro-agent into an RC network analog. Each section is driven by a current source that represents the laser heat captured in the specific portion of the micro-agent.

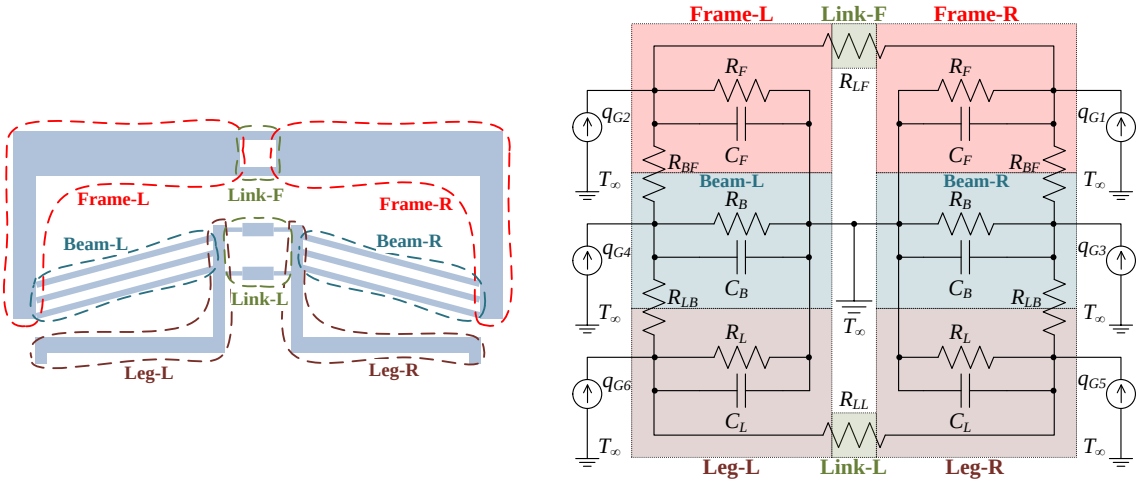

Figure 7.28. Lumped sections of the micro-agent (left) and thermal network equivalent of the lumped model (right).

7.5.4 *Thermo-Mechanical Model*

The stick-and-slip motion presented before depends on the asymmetry of friction forces due to the slight angle of the surface of the structure and the difference in the friction forces under the feet and the dimple. In the lumped model of the robot in Fig. 7.29, its total mass is split and concentrated at the two ends of its structure.

The frame and half of the beams are assumed to have a mass of m_1, while the feet, shuttle, and the other half of the beams are combined into m_2. The two masses are connected with a massless actuator producing a force F_a and opposing the static friction forces F_{si} $(i = 1, .., 4)$ due to gravitation g and downward pulling adhesion forces for the respective masses F_{hj} $(j = 1, 2)$.

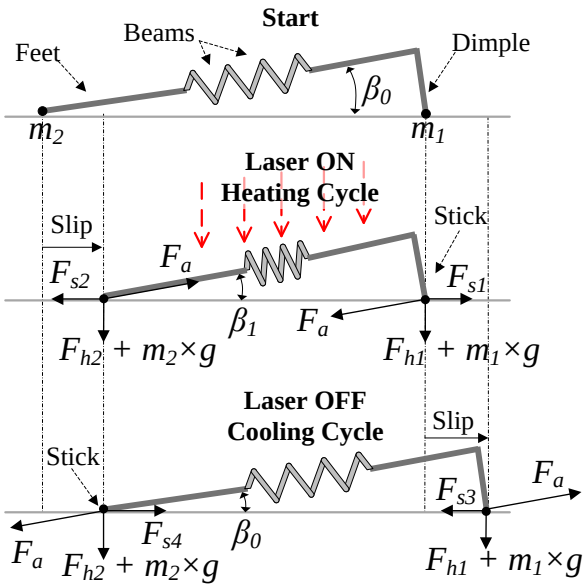

Figure 7.29. Stick-slip cycles of the micro-agent and forces acting at the interface with the substrate (side view).

For the micro-agent to move as in Fig. 7.29, the actuation force should alternately overcome friction such that the friction force under the feet is smaller in the heating cycle whereas it is smaller under the dimple in the cooling cycle. The static friction forces F_s are given by:

$$
\begin{aligned}
F_{s1} &= \mu_s(F_{h1} + m_1 g + F_a \sin\beta_1) \\
F_{s2} &= \mu_s(F_{h2} + m_2 g - F_a \sin\beta_1) \\
F_{s3} &= \mu_s(F_{h1} + m_1 g - F_a \sin\beta_0) \\
F_{s4} &= \mu_s(F_{h2} + m_2 g + F_a \sin\beta_0)
\end{aligned}
\tag{7.13}
$$

where μ_s is the coefficient of static friction, F_{hi} $(i = 1, 2)$ is the adhesion force for the respective mass, and β_0 and β_1 are the tilt angles of the robot surface for the rest and contracted states, respectively. If

$$
F_{s1} > F_{s2} \quad , \quad F_{s4} > F_{s3} \tag{7.14}
$$

then the robot will move as depicted in Fig. 7.29. Assuming that the change in tilt angle is small and hence $\sin\beta_1 \approx \sin\beta_0$, the conditions in (7.14) become

$$
F_a > \frac{1}{2\sin\beta}\Big(|F_{h1} - F_{h2} + (m_1 - m_2)g|\Big) \tag{7.15}
$$

Therefore, a good design choice is to make

$$
|F_{h1} - F_{h2} + (m_1 - m_2)g| = 0 \tag{7.16}
$$

so that whenever F_a is large enough to overcome the smaller of the friction forces, it automatically satisfies (7.15) resulting in the stick-slip motion. Then, the corresponding masses undergo the following accelerations:

$$
\begin{aligned}
m_1\ddot{x_1} &= F_a \cos\beta_0 - \mu_d(F_{h1} + m_1 g - F_a \sin\beta_0) \\
m_2\ddot{x_2} &= F_a \cos\beta_1 - \mu_d(F_{h2} + m_2 g - F_a \sin\beta_1)
\end{aligned}
\tag{7.17}
$$

where μ_d is the coefficient of dynamic friction and x is the position along the horizontal axis.

The force required to suppress the deflection of a chevron actuator [108] can be written as

$$F_a = k\Delta x\,, \quad k = \frac{2NA_BE\sin^2\theta}{L_B}\,, \quad \Delta x = (d_{\Delta T} + l - l_0) \tag{7.18}$$

where k is the stiffness of actuator beams and Δx is the difference between current and maximum displacement of the beams. N is the number of beams, A_B is the cross sectional area of a beam, E is the Youngs modulus, θ is the bending angle after deflection, L_B is the projected length of the beam, $d_{\Delta T}$ is the deflection of the actuator due to temperature change without external force applied, l_0 is the rest length of the micro-agent from its feet to dimple, and l is the instantaneous length of the micro-agent when the beams are at temperature T. This force can be taken as the instantaneous force generated by the actuator. Deflection can be approximated by

$$d_{\Delta T} = L_B\tan\theta - L_{B0}\tan\theta_0 \tag{7.19}$$

where θ_0 is the initial bending angle. We can calculate the bending angle after deflection as

$$\theta = \cos^{-1}\left(\frac{\cos\theta_0}{1+\alpha_e\Delta T}\right) \tag{7.20}$$

where α_e is the coefficient of thermal expansion and ΔT is the temperature change.

Finally, the net torque and the resulting rotational acceleration can be written as:

$$I\dot{\omega} = \Big((F_{a1} - F_{a2})\cos\beta_1 - F_s\Big)(L_L + 0.5W_{s1}) \tag{7.21}$$

with F_s being the total friction force, I and ω the moment of inertia and angular velocity of the micro-agent, respectively. It can be seen from equations (7.18) that the motion of the micro-agent is governed by the deflection of the actuator $d_{\Delta T}$ which in turn is driven by the temperature change ΔT caused by laser heating.

7.5.5 *Simulations of the 3-DOF Laser-Driven Micro-Agent*

We implemented the photo-thermo-mechanical model in the previous section in MATLAB and carried out simulations to validate the theoretical conjectures. Table 7.5 lists the constant values used in these simulations.

Table 7.5. Values of some constants used in the simulations

Constant	Quantity/Name	Value/Unit
E	Youngs modulus of PolySi	169×109 N/m^2
H	Thickness	1.5×10^{-6} m
L_B	Beam length, leg length	200×10^{-6} m
T_∞	Temperature at far ambient	300 K
c_v	Si specific heat	700 J/kg.K
k_{air}	Air thermal conductivity	0.026 W/m.K
k_{Si}	Si thermal conductivity	130 W/m.K
Ref	Si reflectivity	0.3
	Si absorption coefficient	10^5 m^{-1}
α_e	Si coefficient of thermal expansion	2.6×10^{-6} K^{-1}
	Angle of surface inclination	0.0375 rad
θ_0	Initial bending angle	0.0175 rad
ρ	Si density	2330 kg/m^3

1-DOF Mobility with Symmetrical Expansion

When the parameters involved in the photo-thermo-mechanical model of the micro-agent are symmetrically selected, the mobility of the robot reduces to 1. A typical result showing the heating and cooling cycles of the beams and the respective change in the position is shown in Fig. 7.30. In this simulation, the laser pulse

is at 2ms period, 50% duty cycle, and 0.4W/mm^2 power. The position change is measured at the dimple, hence it takes place in the cooling cycle. The thermal network model suggests that the steady state temperature increases linearly with the input power. However, the maximum velocity of the micro-agent is limited by the maximum temperature that the material can withstand.

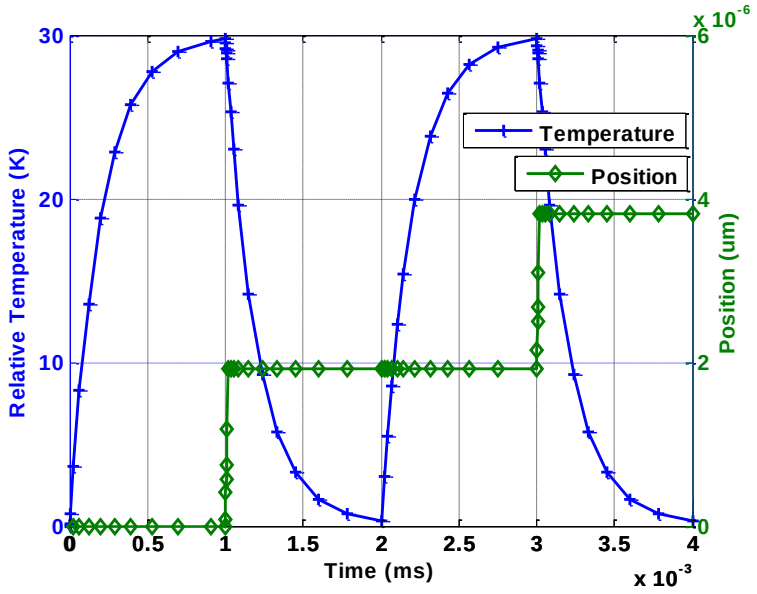

Figure 7.30. Micro-agent position vs beam temperature change generated by laser pulse.

With the same simulation settings (the laser pulse at 2ms period, 50% duty cycle, and 0.4W/mm^2 power) Fig. 7.31 shows the average velocity versus frequency relationship in which the peak is attained at around 1100 Hz for the particular geometry. This shows that there is an inverse relationship between frequency and actuator deflection as expected from the thermal-capacity nature of the system. Also, there is a directly proportional relationship between pulse frequency and micro-agent ve-

locity. Therefore, the combined effect of the two relationships results in a band-pass frequency response as in Fig. 7.31.

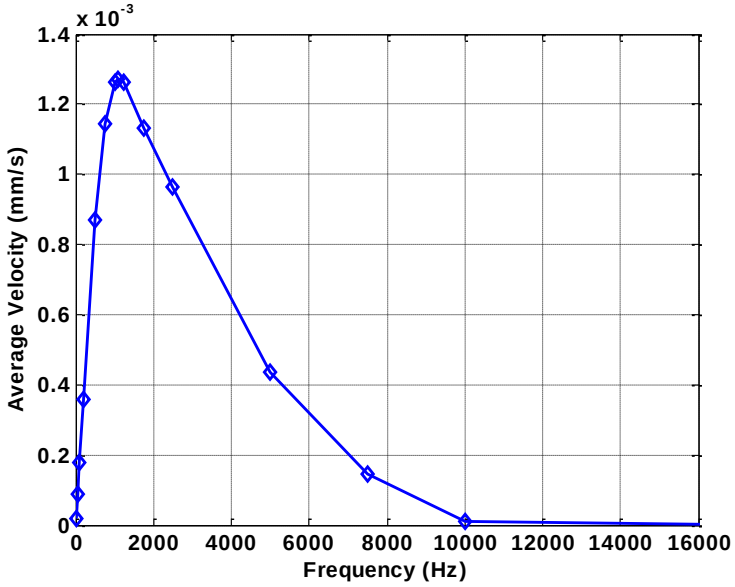

Figure 7.31. Laser pulse frequency response of the micro-agent velocity.

Figure 7.32 shows the change of average velocity with duty cycle (at 2ms pulse period and 0.4W/mm^2 power level) and reveals the fact that, although the average power transferred to the beams increases with the duty cycle, the actuator deflection decreases when the duty cycle moves away from 50%. This again reveals the fact that the beams have to cool down sufficiently to generate effective shuttle motion.

Finally, Fig. 7.33 shows the relationship between velocity and input laser power at (at 2ms pulse period and 50% duty cycle). Laser power is related to temperature via the photo-thermal model in (7.11). Change in temperature of the actuator beams, in turn, affect the geometry of the micro-agent through (7.20) which then generates the actuator force in (7.18).

3-DOF Mobility with Asymmetrical Expansion

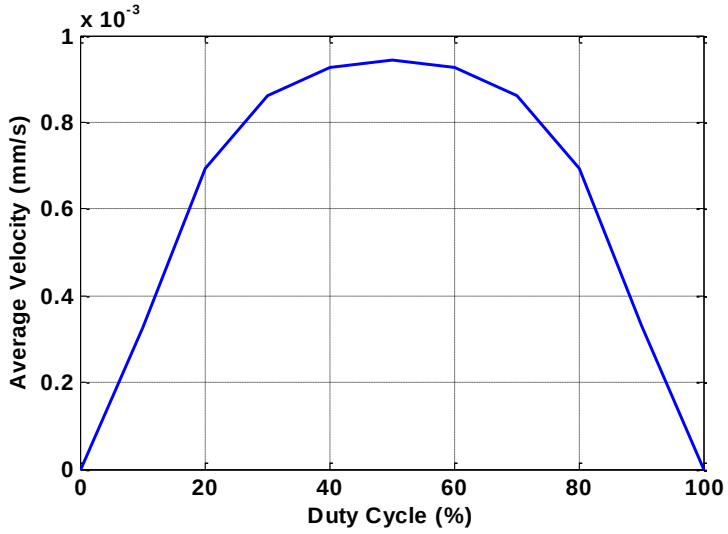

Figure 7.32. Change of average velocity of with laser pulse duty cycle.

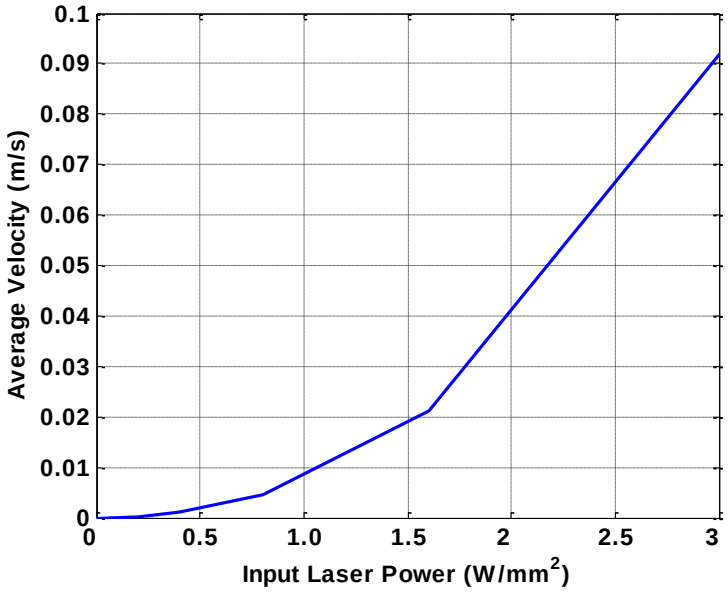

Figure 7.33. Change of average velocity with input laser power.

Asymmetrical design of any parameter that goes into the formulation of the model of the micro-agent has the potential to create rotational motion on the plane.

However, the point is to be able to control the rotation using the temporal variables of the laser source such as frequency.

The previous results showed that the velocity of the micro-agent depends on three important temporal variables of the input source, namely frequency, amplitude, and the duty cycle. Depending on the structural asymmetry that can be created in the micro-agent design, those temporal variables of the input signal can be used to control the rotational degree of freedom of the robot. For instance, frequency can be used to control the rotational motion such that different intervals of frequencies can put the actuator into differential expansion mode.

Figure 7.31 shows that a micro-agent with a particular actuator structure has a laser frequency at which its velocity is maximum. Then, if the time constant of the lumped actuator beams on the right can be made different than those on the left, the operation frequency becomes an addressing mechanism of individual beam sets. Therefore, the velocity characteristic of a micro-agent due to the leg on one side can be made different than that on the other side as in Fig. 7.34, where τ_1 and τ_2 are the different time constants of the beam sets on two sides of the actuator. The figure on the right of Fig. 7.34 should be interpreted as follows: If the actuator of the micro-agent was designed with a thermal time constant of τ_1, then let say the frequency response would be like the solid line with f_1 peak frequency. A different micro-agent design with τ_2 that is less than τ_1 would result in the dashed response with a peak frequency of f_2 that is also greater than f_1. Now, if these two cases are asymmetrically present in an actuator as in the right figure in Fig. 7.34, then the frequency of the laser pulse becomes an addressing mechanism to excite one leg of the micro-agent more than the other, resulting in rotational motion.

Since deflection depends on temperature, force depends on deflection, and in turn velocity depends on force, changing the thermal time constant of one side of the

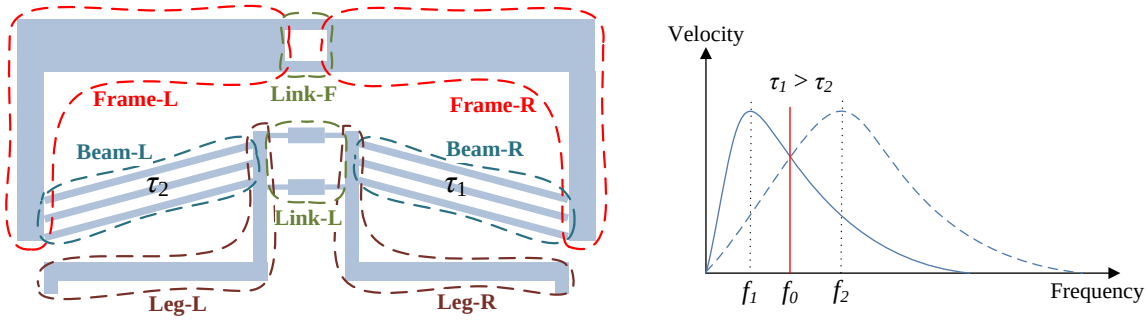

Figure 7.34. Thermal asymmetry of the right and left actuator beam sets enables differential velocity response.

actuator creates differential expansion behavior. From (7.9) and (7.11), changing the time constant is possible by changing h, the heat transfer coefficient that depends on the air film thickness δz. This requires a consideration in the fabrication process. For example with PolyMUMPS, part of a device can be created in Poly-1 and the rest in Poly-2 so that the film thinkness below the two parts are different, hence the heat transfer coefficients.

One side effect of designing the micro-agent such that the heat transfer coefficient h is different on the right and left beam sets is that the maximum temperature swing becomes less on the side that has higher h. This is because of the increased heat transfer to the substrate. In order to balance the maximum temperature swing, part of the micro-agent frame on the side with smaller h can be coated with gold so that the high reflectivity of gold results in lower heat generation on that side. This balances the maximum temperature swing of the two sides, providing equal left and right turning velocities.

Simulations show that when the heat transfer coefficient of the beams on the right side of the micro-agent is reduced by 10% and Frame-L is coated with gold, the frequency response of the angular velocity of the micro-agent becomes as in Fig.

7.35. The crossover frequency is determined to be 1202 Hz, at which the angular velocity is zero and the turning direction changes. Figure 7.36 gives the trajectories of the micro-agent on the X-Y plane for several input frequencies. Simulation results suggest that the agent can be controlled on the plane with various translational and rotational speeds that are nonholonomically constrained such that the rotational and translational velocities are coupled while backward motion is not possible. This constraint comes as a tradeoff of the particular design in favor of using only one laser spot. In summary, the reduced heat transfer coefficient on one side of the robot results in different time constants, making the micro-agent legs addressable by the laser pulse frequency.

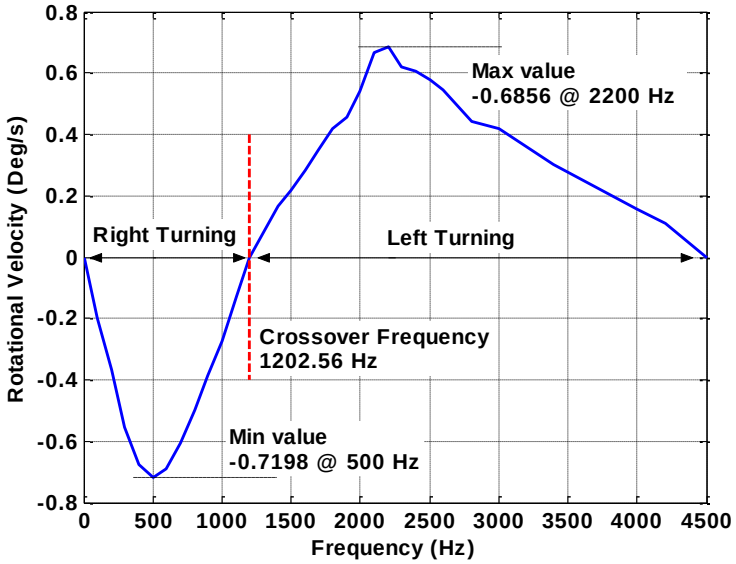

Figure 7.35. Frequency response of the rotational velocity of the micro-agent.

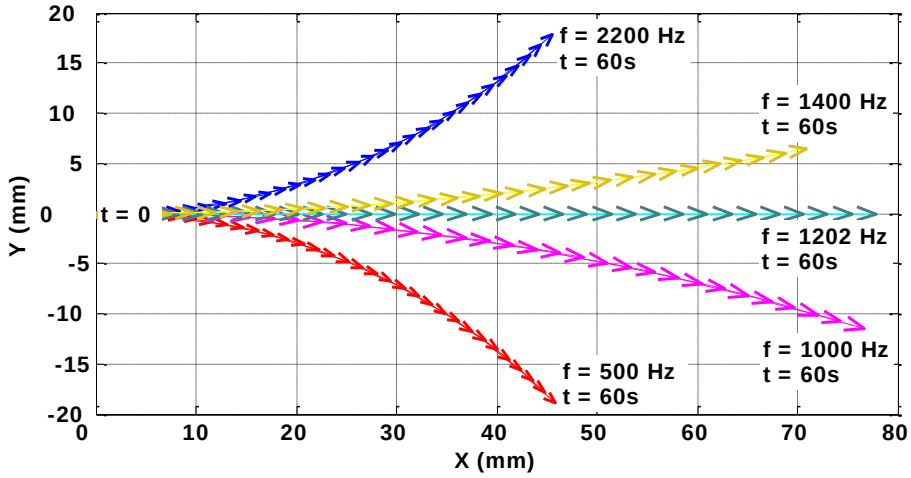

Figure 7.36. Trajectory of the micro-agent on the X-Y plane vs pulse frequency.

7.6 Experiments on a Laser-Driven Micro-Agent

We fabricated various micro-agent geometries to partly test the stick-and-slip motion idea presented in section (7.5). Figure 7.37 shows the CAD design of a die mask containing various laser-driven micro-agent designs. The fabrication process used is Silicon-On-Insulator (SOI) processing as will be explained in the next chapter. This process allows MEMS device fabrication on a single structural Silicon layer. Hence, the dimple structure of the micro-agent design in Fig. 7.21 is separately fabricated on the same wafer and assembled on to the micro-agent frame via a micro-assembly process explained in the next chapter.

Initially, we tested the micro-agents without a dimple attached. Observations showed that there was no motion at all. This is expected because the structure of the agent is planar and it only generates in-plane motion which cannot propel itself as it is parallel to the underlying surface. Then, the dimple assembled micro-agents were tested on a silicon die. We observed motion in the form of in-place rotation and slight translation that occurred intermittently during the test. We continued the test by increasing the power level until the micro-agents were significantly damaged

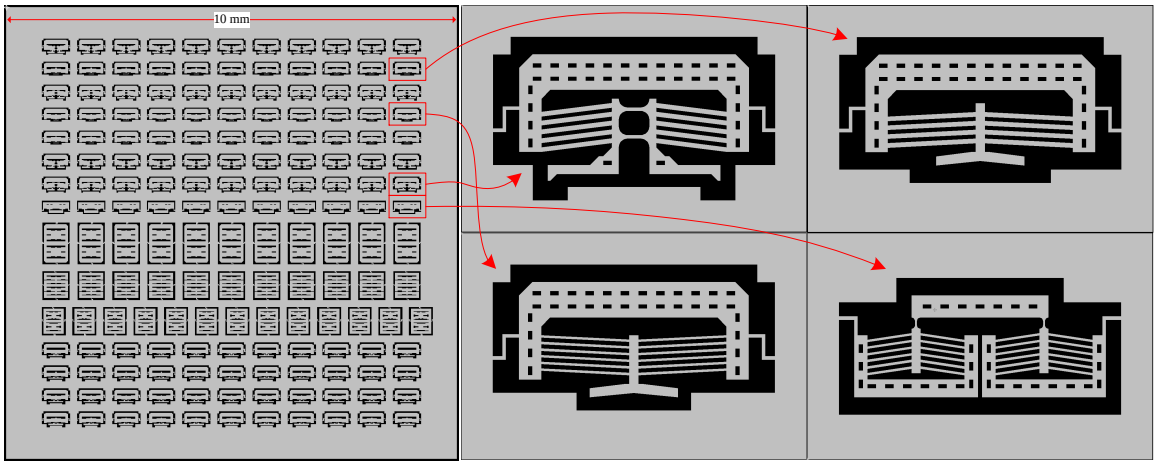

Figure 7.37. CAD design of the die mask with various laser-driven micro-agents (left) and a closed up view of four micro-agents (right).

by the laser heat. The observed motion was repeatable and indicative of a possibly predictable mechanism of locomotion. Figure 7.38 shows the initial and final positions of a micro-agent for the same input excitation. The similarity of the final position and the appearance of the motion suggest that the response of the micro-agent may have a characterizable nature.

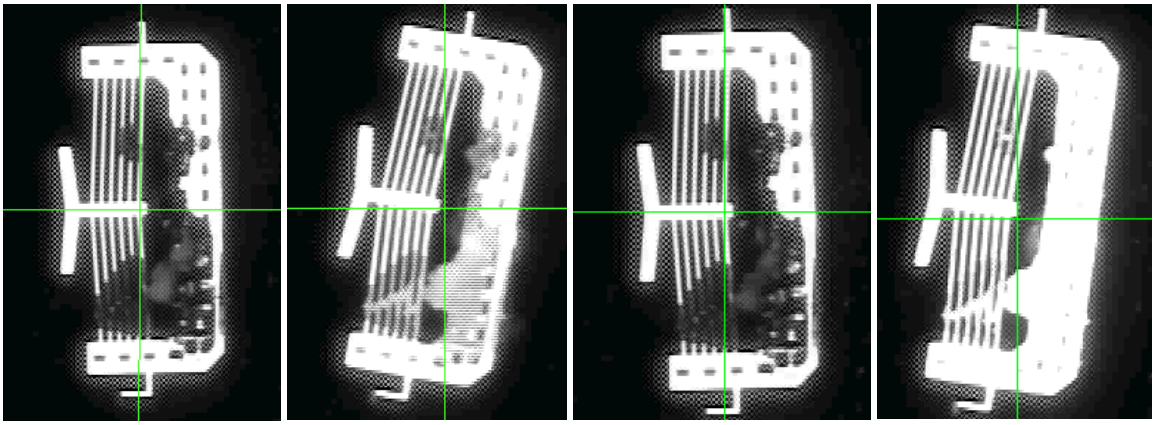

(a) 1st initial position (b) 1st final position (c) 2nd initial position (d) 2nd final position

Figure 7.38. Laser driving test results on an assembled micro-agent.

Another observation in this experiments is shown in Fig. 7.39. Excessive laser power melts the Silicon structure of the micro-agent. After the melting, we poked the agent with a micromanipulator needle and observed that it was stuck to the surface. Applying some force kicked off the agent that left behind the tips of the feet. These pieces of the feet were found to be fused to the Aluminium coated glass substrate. This indicates that there was a significant amount of heat transfer from the micro-agent body to the substrate via these contact points. The same fusing did not take place for the dimple but it left a noticeable foggy residue.

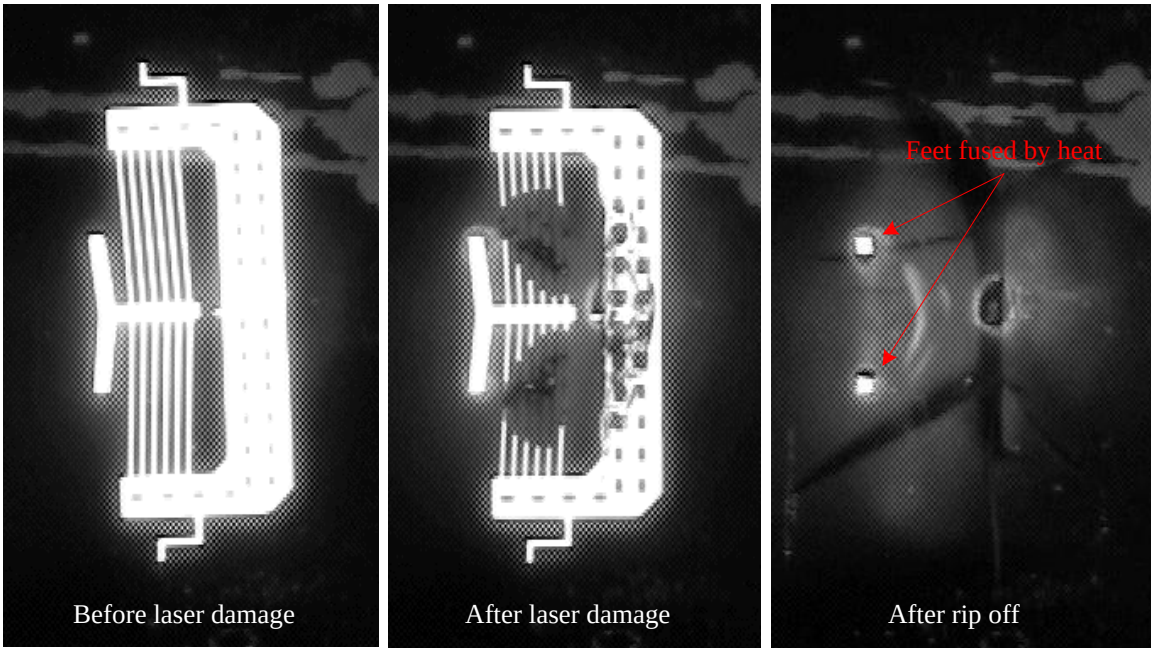

Figure 7.39. Excessive laser heat causing melting of micro-agent.

7.7 Experiments on Other Micro-Agent Control Methods

We also evaluated the potential of other power delivery and control methods such as vibration and magnetic fields. Some preliminary experimental results are presented in the following parts.

7.7.1 *Vibration-Driven Micro-Agents*

Mechanical systems have resonant modes at certain frequencies that result in significant amounts of deformation in their structures. This phenomenon has be made use of in various macro and micro scale applications as discussed in chapter 2.2. The idea of vibrating a surface to induce motion on an agent on top of it is conceptually simple but theoretically very cumbersome. The control variable in this method is the frequency of the vibration. The geometry of the agent can be designed in such a way that it resonates at certain distinct frequencies in a predetermined way. A desired type of motion can be expected to emerge from the resonance of the agent. However, the response of the agent to a vibration excitation depends not only on its geometry but also very much on the environmental conditions which are difficult to control in micro-scale.

Initially, we performed modal analysis in MATLAB/SUGAR to find out the geometries that produce distinct resonance modes. It has been observed that mass-spring like geometries in micro-scale can generate 1st and 2nd modal swings at reasonable frequency ranges such as 1-50 KHz. Figure 7.40 shows the CAD design of a die mask containing various vibration-driven micro-agent designs with such mass-spring like features. For a micro-scale serpentine leg structure as shown in Fig. 7.41, the first two modal frequencies were found to be 18284 Hz and 20521 Hz.

We had done automated tests with various different micro-agent designs and collected the frequency response data of their mobility. The automated test system is

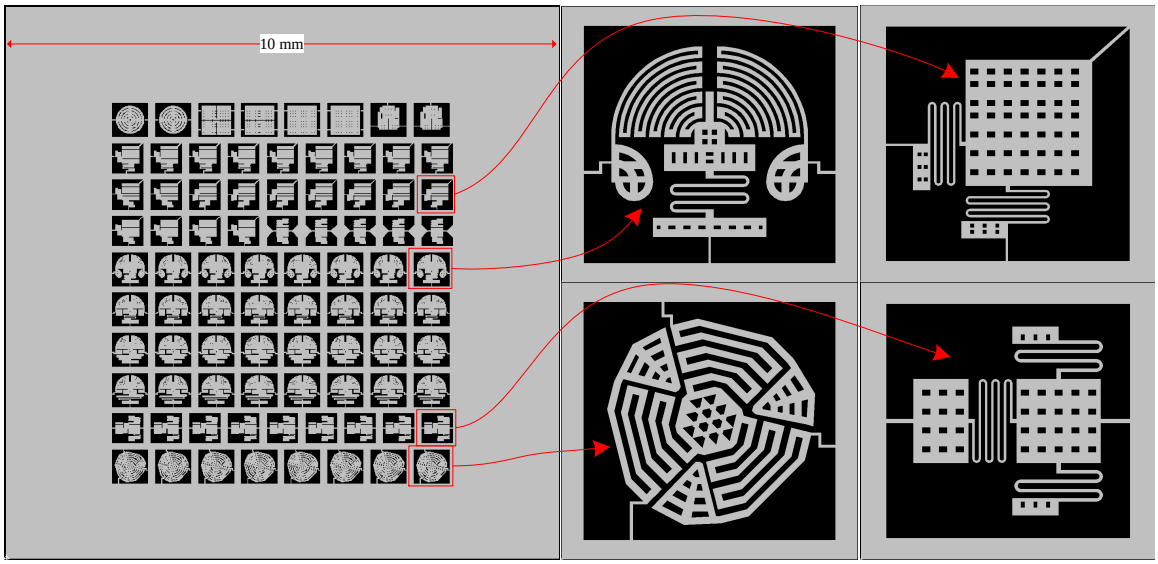

Figure 7.40. CAD design of the die mask containing various vibration-driven micro-agents (left) and a closed up view of four micro-agents (right).

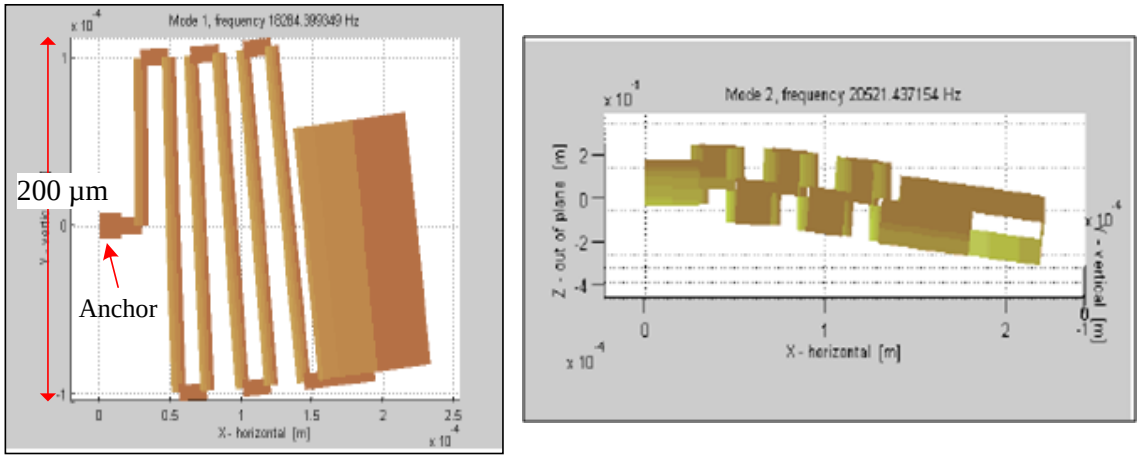

(a) 1st mode (lateral) at 18284 Hz

(b) 2nd mode (vertical) at 20521Hz

Figure 7.41. Modal analysis result in MATLAB/SUGAR for a mass-spring like micro leg structure.

shown in Fig. 7.42 where a piezoelectric (PZT) actuator is used to convert a square wave signal into vibration. The arena of the micro-agent is squeezed between the PZT actuator and a solid surface. The controller of the system sweeps through a user

defined range of frequencies incrementally and captures the motion of the micro-agent with a smart camera that is programmed to process the image and send its pose and velocity data back to the controller for logging. Figure 7.43 shows a snapshot of the video stream captured by the smart camera at 60 fps and processed in real-time. The image processing program running in the smart camera detect the micro-agent in its arena as shown in Fig. 7.43 and calculates its current position and orientation based on a predefined image template.

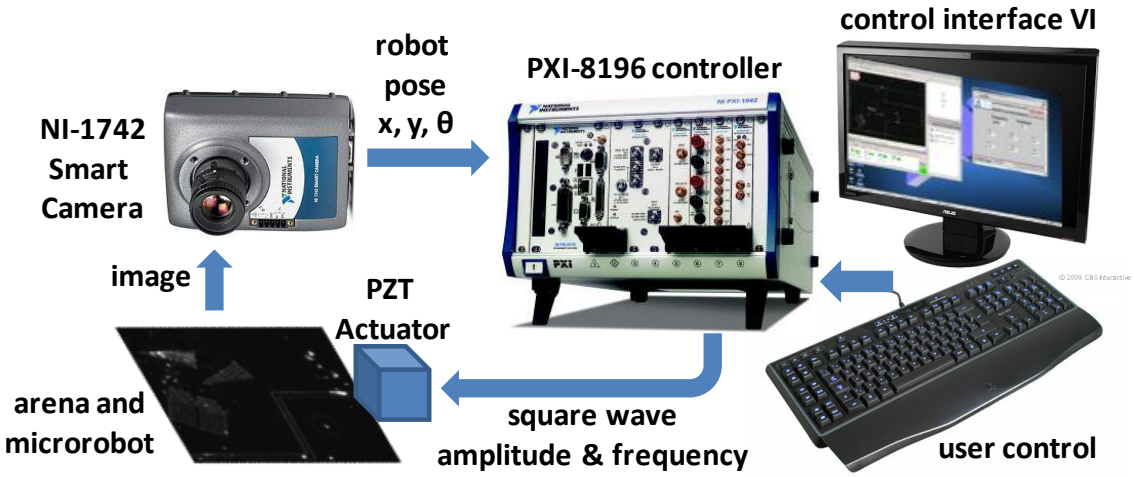

Figure 7.42. Vibration-driven micro-agent control system.

The test results presented in Fig. 7.44 and Fig. 7.45 shows the distinct frequencies at which the motion of the micro-agent peaks. While some of the frequencies such as 3700 Hz seem to be equally effective in generating both translational and rotational motion, some of them such as 10300 Hz generate more rotational motion than translational.

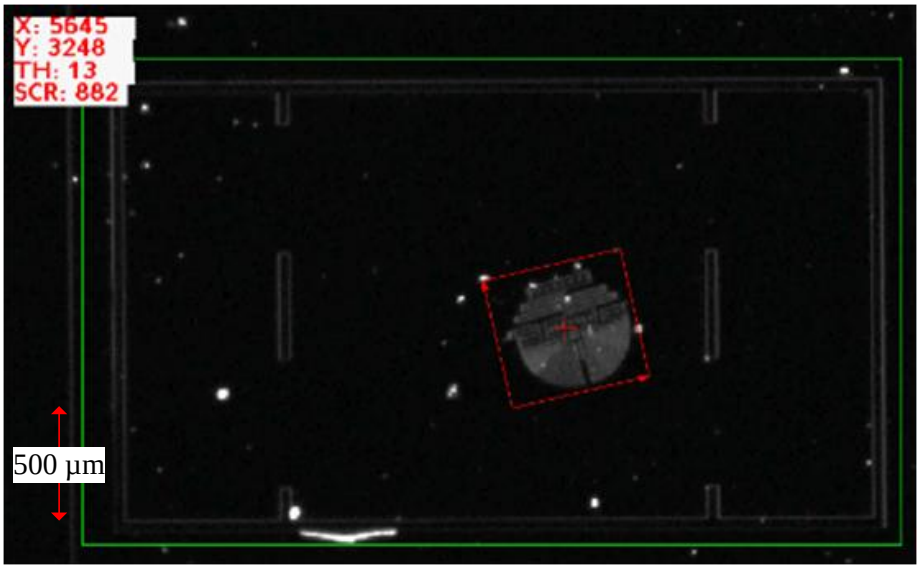

Figure 7.43. A vibration-driven micro-agent under automated test.

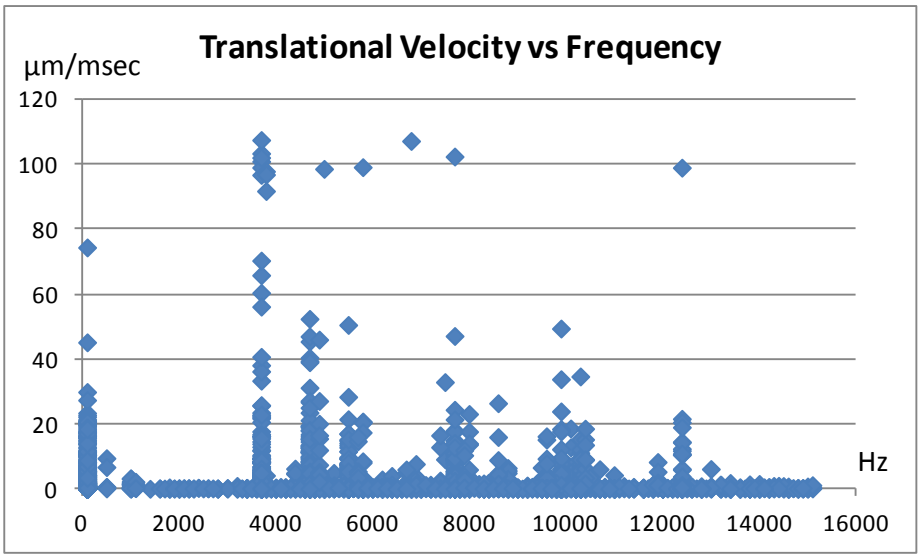

Figure 7.44. Micro-agent translational velocity vs applied vibration frequency.

7.7.2 *A Control System for Magnetic Micro-Agent Driving*

Magnetically driven micro-agents are easier to control in many respects than any other method due to the well defined nature of interaction between magnetic bodies. Hence, this method has found predominant interest by the participants of the NIST

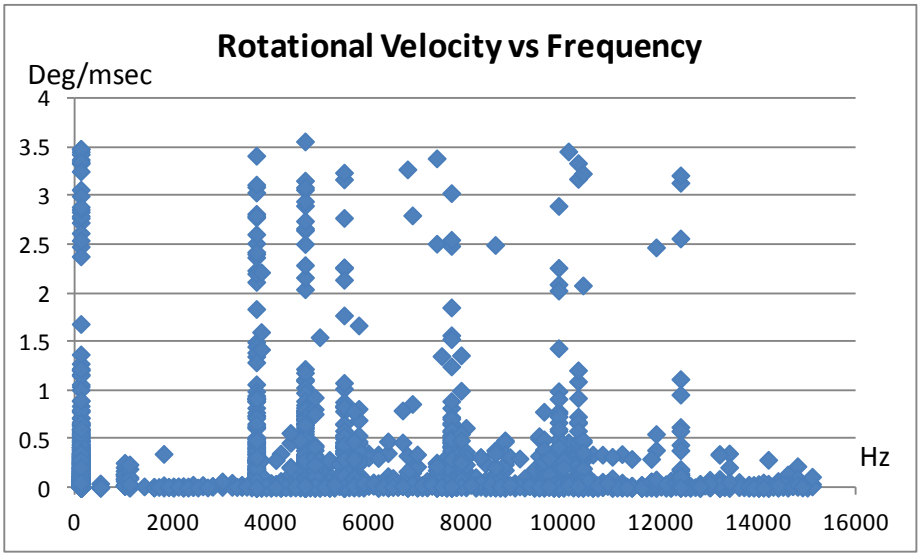

Figure 7.45. Micro-agent rotational velocity vs applied vibration frequency.

Mobile Microrobotics Challenge so far [109]. We participated in this challenge with a magnetically controlled micro-agent in 2012. We designed the system shown in Fig. 7.46. The Silicon arena die is held by a lab jack above an $xy\theta$ manipulator. The manipulator's end-effector is a driver magnet attached to the tip of a metal pin. The arena is positioned sufficiently close to this driver magnet from above such that their magnetic attraction can be used to control the position of the micro-agent by controlling the driver magnet position via the motorized $xy\theta$ manipulator.

Figure 7.47 shows magnified pictures of the arena, the micro-agent, and the driver magnet. The micro-agent is a cube of $500\mu m$ side length made of Neodymium (Nd2Fe14B) which is a rare-earth permanent magnet, an alloy of Neodymium, Iron, and Boron. Similarly, the driver magnet is also the same type of permanent magnet with a cylindrical shape (1.5 mm diameter and 1 mm height). These magnets are commercially available.

The mobility of the micro-agent on the arena surface can be controlled with the system shown in Fig. 7.48 in two modes of operation. One is the vertical arrangement

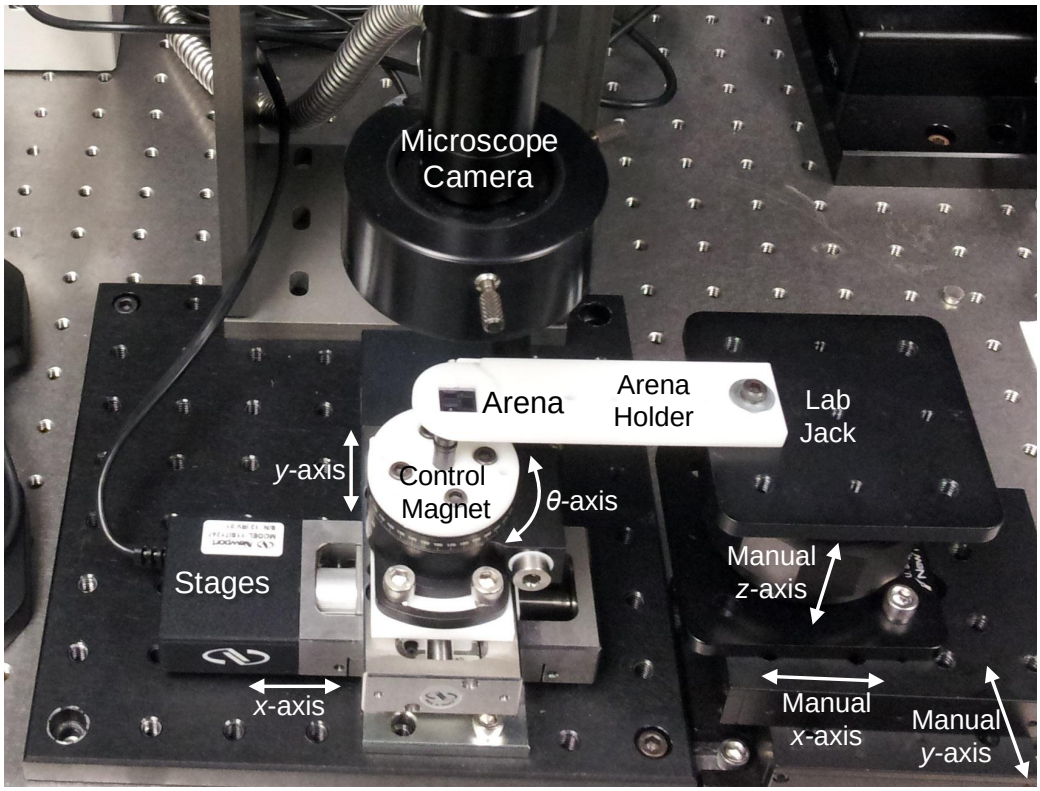

Figure 7.46. Control system for magnetically-driven micro-agent.

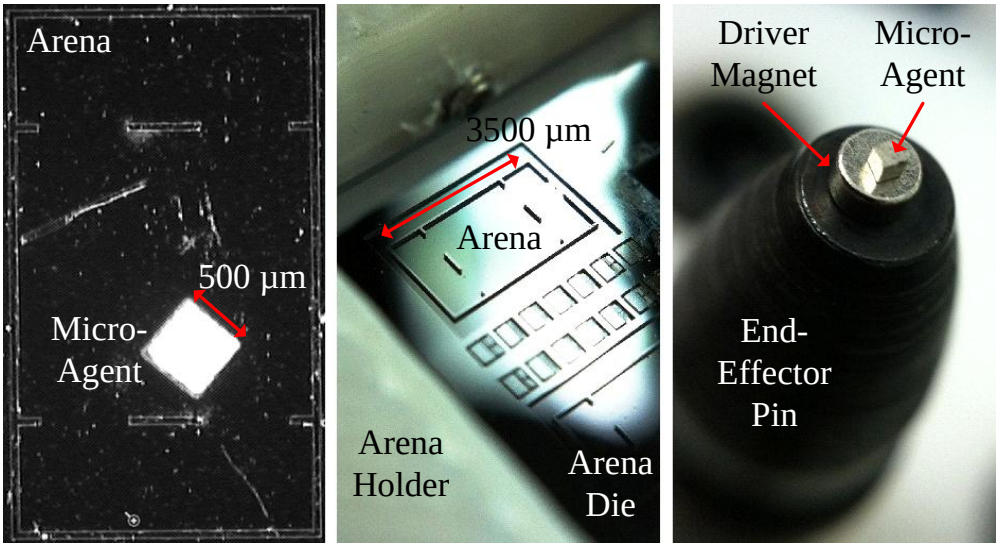

Figure 7.47. Magnetically-driven micro-agent.

of the poles of the two magnetic bodies. In this case the driver magnet can control the position of the agent with 2 degrees of freedom: x and y positions. The magnetic attraction between two bodies drags the micro-agent towards the centerline of the driver magnet. This attraction also results in friction between the micro-agent and the arena surface. Rotation of the driver magnet by the θ-axis of the manipulator does not induce rotation in the micro-agent because the magnetic axes are aligned with the axis of rotation. An exception to this is when the driver magnet is attached to the pin eccentrically by an offset from its rotation center. In this case, however, rotation of the θ-axis results in circular displacement of the driver magnet around the rotation center, inducing both translational and rotational motion in the micro-agent that is not easily controllable.

The other arrangement is the horizontal alignment of the poles as in Fig. 7.48. In addition to xy motion, in this case, the θ-axis can generate rotational motion in the micro-agent. Also, the friction experienced by the micro-agent is less in this case due to the reduced vertical pulling force of the driver magnet. However, there is also a couple of drawbacks with this arrangement. One is that a significant portion of the magnetic fields emanating from the driver magnet close onto itself without intercepting the micro-agent, reducing the overall effect of the driver magnet. The other problem is that the micro-agent tends to snap to one of two magnetic minima which occur towards the north and south edge of the driver magnet over the arena. Hence, the micro-agent experiences occasional jumps from one minimum to the other during its motion.

7.8 Chapter Conclusions

In this chapter, we proposed a novel stick and slip micro-agent actuated via laser heating with a single spot. The robot gait is accomplished by differential thermal ex-

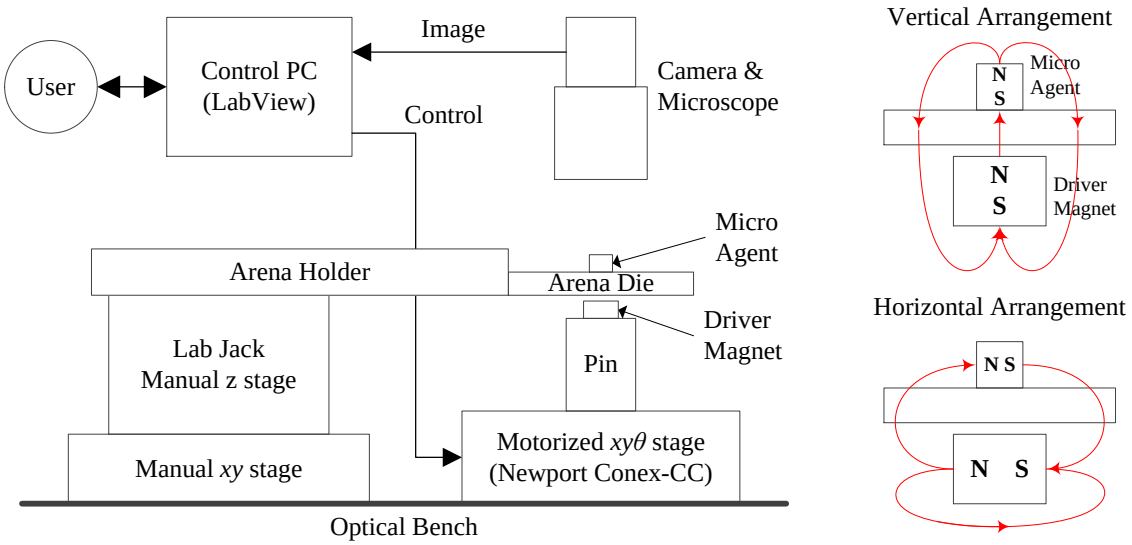

Figure 7.48. Control system digram for magnetically-driven micro-agent.

pansion, and uses the laser power, pulse frequency, and duty cycle as control inputs. A photo-thermo-mechanical model for the micro-agent was formulated and simulated, with results indicating turn controllability, as well as anticipated forward velocities in the order of mm/sec. Although the simulation results presented in this chapter are based on several simplifying assumptions of the physical operation conditions, such as absorption of laser by the actuators, friction forces, and frequency response characteristics, we can still conclude that the laser powered micro-agents can be controlled with a single laser beam, and can be competitive alternatives to electrostatically or electromagnetically actuated micro-agents in controlled environments such as the Microrobotics Challenge of NIST. Preliminary experiments confirm that the thermal power delivery method by focused laser leads to similar actuator responses as the electrothermal method in terms of the actuator deflection and frequency response.

CHAPTER 8

FABRICATION AND ASSEMBLY OF MICRO-AGENTS

The Silicon micro-agents, arenas, and micro-parts presented in the previous chapter were fabricated using standard Silicon-On-Insulator (SOI) MEMS processing techniques [116, 117]. Figure 8.1 shows a picture of the lithography mask design layout made for 4" SOI wafer processing. This mask design contains 52 dies of size 10mm×10mm and various designs of laser and vibration driven micro-agents, NIST Mobile Microrobotics Challenge arenas [109], micro-parts such as dimples and some assembly parts, test dies with miscellaneous micro-actuators and micro-structures. Four of those 52 dies are zoomed on the right of Fig. 8.1. There are 11 different dies on this mask design so there is at least two copies of each die type on the mask. This is done in order to increase the chances of fabricating usable dies of a certain type if one part of the wafer becomes defected during fabrication or post-processing.

The fabrication of micro-agents and arenas were targeted towards participation in NIST Mobile Microrobotics Challenge in 2011 and 2012 [109, 118] held as part of the IEEE International Conference on Robotics and Automation (ICRA). The author has led the UTA Microrobotics Team in May 9-14, 2011, Shanghai, China and in May 14-18, Saint Paul, Minnesota. Information about the challenge rules can be found in Appendix E.

Figure 8.2 shows SEM images of some of the fabricated micro-agents. As per NIST rules, each micro-agent is less than 600 μm in length. The fabrication of micro-agents involves several steps of processes in a cleanroom with Silicon micromachining tools. After that, some of the micro-agents are also assembled with additional features

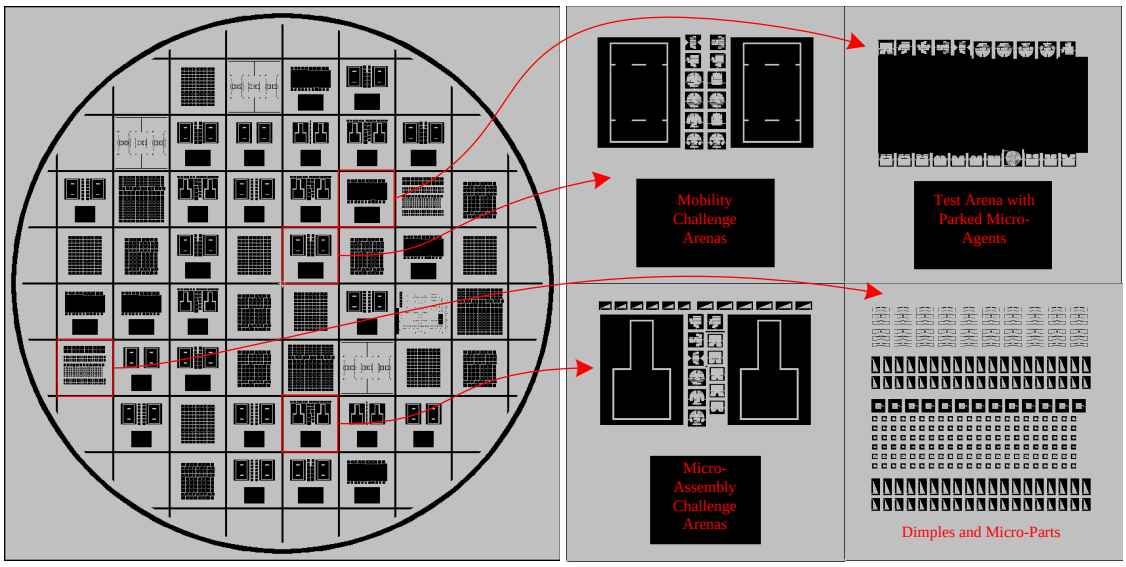

Figure 8.1. Lithography mask design layout for 4" SOI wafer and some of the dies on it.

using a microassembly system. The steps of micro-agent fabrication and assembly are listed in Table 8.1 and are illustrated in Fig. 8.3. We have carried out the micro-fabrication processes at UTA Nano Fabrication Facility and UT-Dallas Cleanroom Laboratory. The microassembly processes, on the other hand, have been done at the Research Institute of UTA using the station we developed as shown in Fig. 8.4. More details on the fabrication processes can be found in Appendix C.

The system shown in Fig. 8.4 is composed of motorized/manual precision stages, microscope cameras, instrumentation and control hardware, and micromanipulators such as vacuum tweezer, microgripper, and needle micromanipulator. These manipulators are used to handle microparts for assembly and testing. The system also includes a high power (12 W) laser source that is used for contactless manipulation such as detethering of parts and curing thermal adhesives as well as delivering power to laser-driven microactuators and mobile micro-agents.

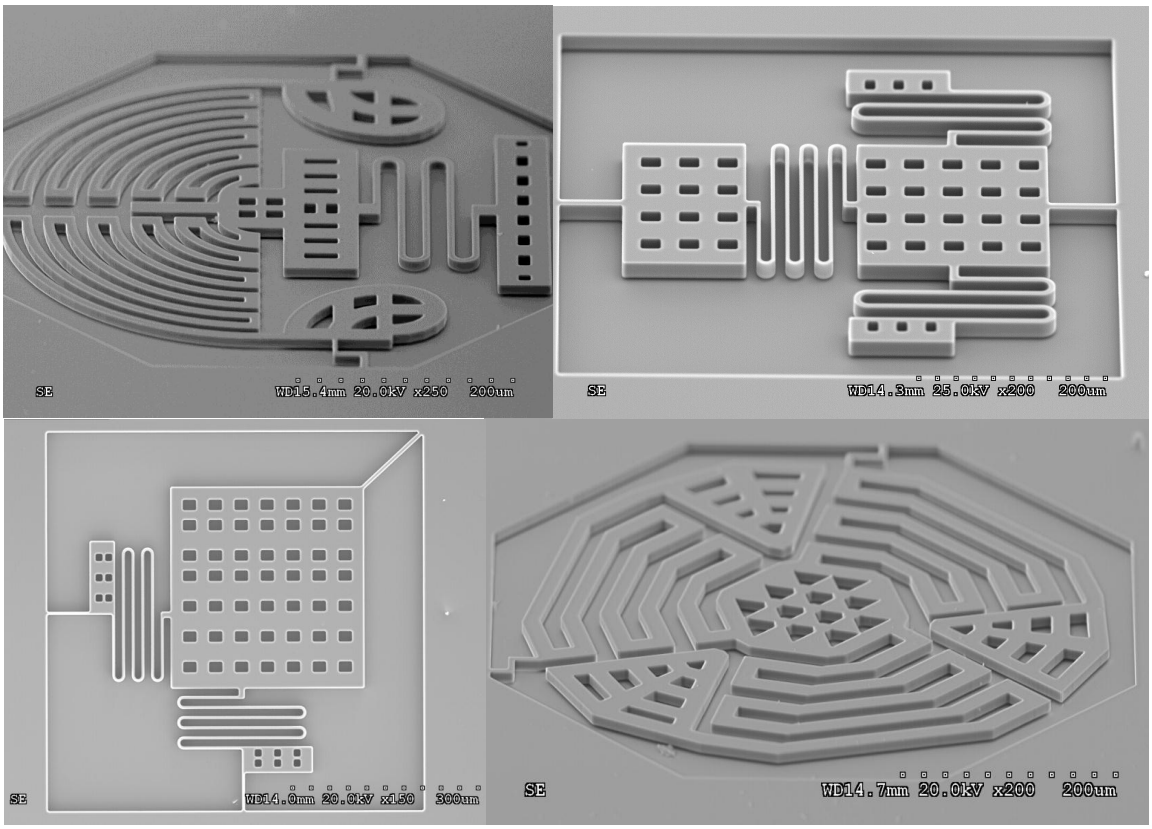

Figure 8.2. SEM images of some of the fabricated micro-agents.

8.1 Laser-Driven Micro-Agent Dimple Assembly

Assembling a micro-agent for laser-driving experiments is a 3-step process:

- Spreading adhesive on the dimple location of the micro-agent frame
- Gripping the dimple and placing it on the micro-agent
- Curing the adhesive

The first step requires using a micromanipulator needle to spread epoxy on the micro-agent. Figure 8.5 shows how this step is performed. Figure 8.6 shows how a dimple is gripped with a microgripper. Placement of the dimple on the micro-agent is relatively simpler and only requires precise alignment of the two as shown in Fig. 8.7.

Table 8.1. Micro-agent fabrication and assembly process steps

Process Name	Step No	Steps
Lithography	1-8	Wafer cleaning, priming, spin coating, soft bake, exposure, develop, hard bake
Etching	9-11	Deep reactive ion etching, resist removal
Release	12	Timed release with hydrofluoric acid
Drying	13	Super critical point drying with LCO2 purge
Dicing	14	Singulation of dies with dicing saw
Microassembly	15-16	Adhesive dispensing, dimple pickup and placement, adhesive curing

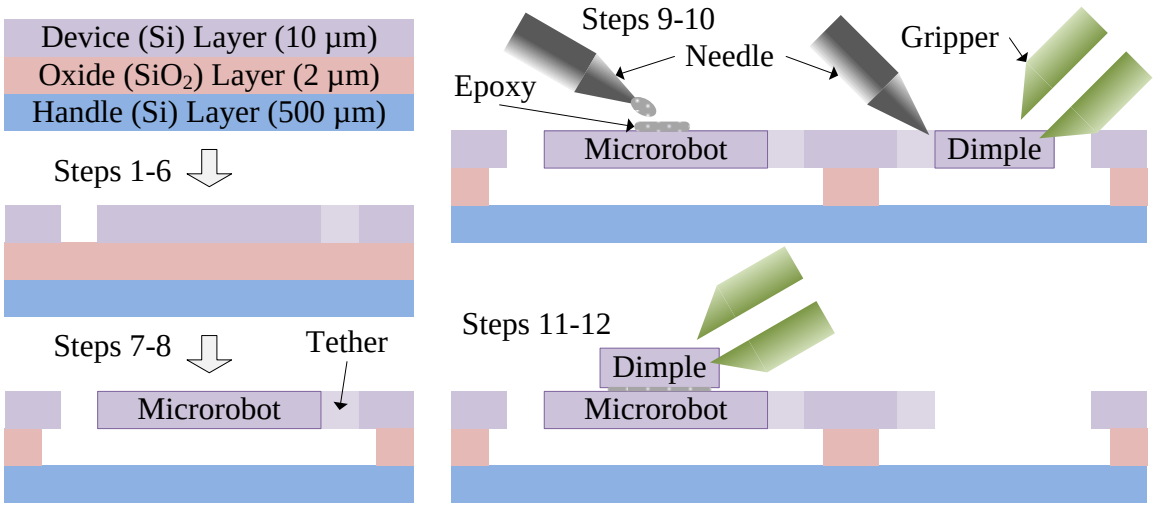

Figure 8.3. SOI micro-agent fabrication and microassembly processes (not to scale).

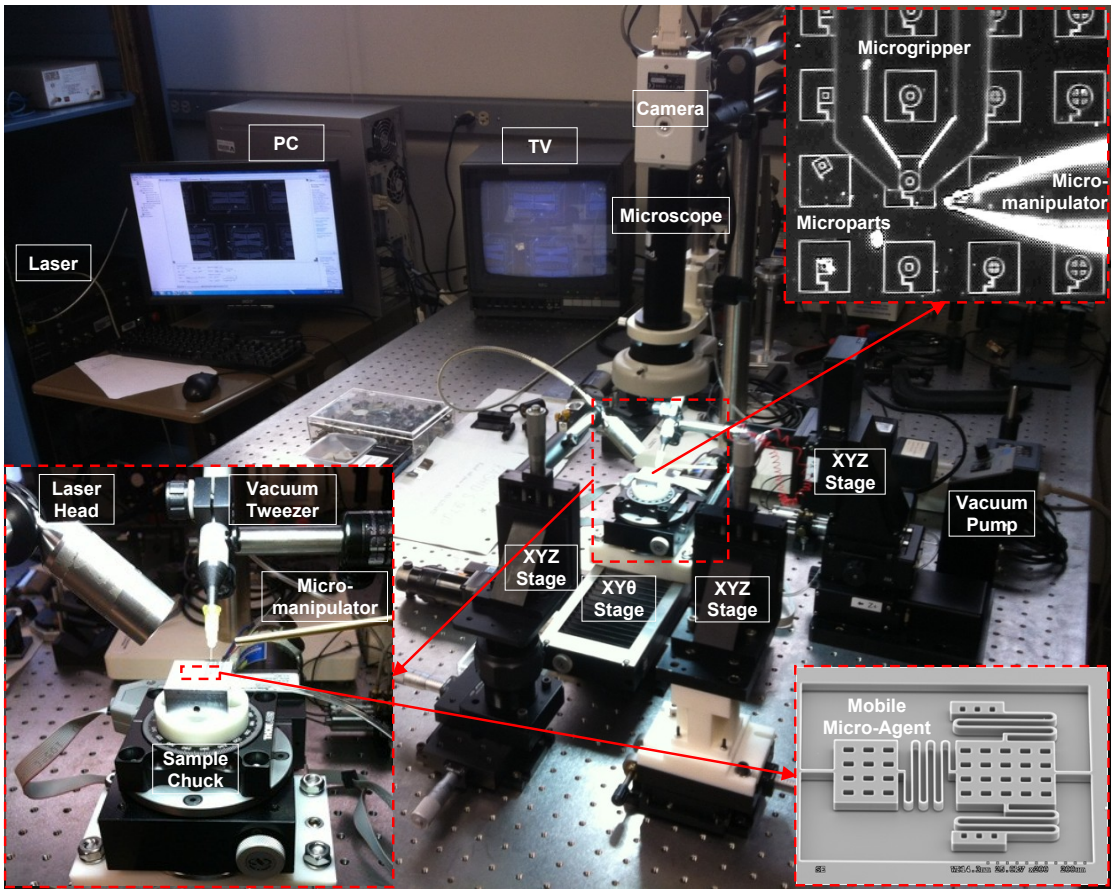

Figure 8.4. Developed system for microassembly and testing of micro-agents.

(a) Needle tip before

(b) Needle immersed in epoxy and moved 4-way

(c) Epoxy spread on the agent

Figure 8.5. Spreading epoxy on micro-agent for dimple assembly.

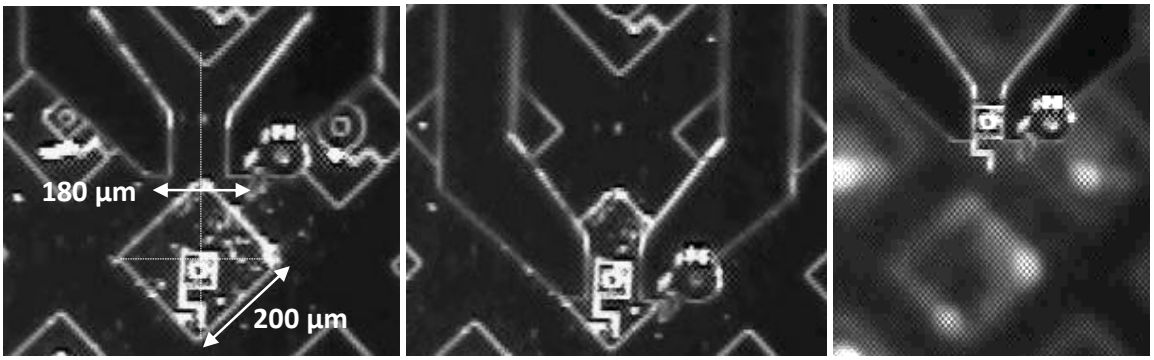

(a) Alignment of the dimple and gripper w.r.t. the die

(b) Alignment between gripper and dimple before gripping

(c) After gripping

Figure 8.6. Gripping a dimple using a microgripper.

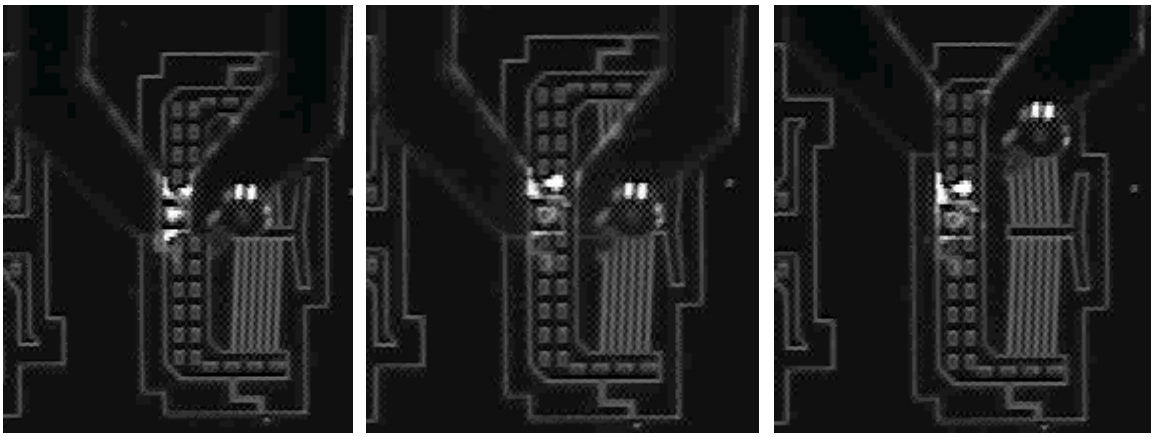

(a) Centering the dimple

(b) Opening the gripper

(c) Removing the gripper

Figure 8.7. Placing the dimple on the micro-agent.

CHAPTER 9

CONCLUSIONS AND FUTURE WORK

Promise of microrobotics is largely dependent on the possibility of automating the assembly and manipulation tasks as they are mostly serial processes. Automation, in turn, is highly dependent on the precision of the system. So far, the research in microrobotics has mostly focused on the success of tele-operated pilot implementations and hence has not revealed the importance of precision for mass micromanufacturing goals. In this thesis, we turn our attention to the eventual goal of microrobotics, which is micro/nano manufacturing and manipulation, and emphasize the importance of enabling automation via analyzing, designing, and controlling microrobotic systems from a precision point of view. Given the fact that higher precision comes with higher cost, we consider the associated budget as an important asset to be carefully allocated among various members of the system so that optimal performance is achieved. We realize that this consideration requires analytical, computational, and experimental tools in the disposal of the designer. Hence, we aim at providing such new tools.

As an analytical and computational tool, we propose a novel method to estimate uncertainty bounds for a microrobot end-effector position due to uncertainties in its physical structure. The approach models uncertainties as intervals and calculates the forward kinematics map using both analytical and computational tools of interval analysis. We extend the products of exponentials (POE) formulation of robot kinematics to intervals. We define interval functions that can take the uncertain POE parameters of a manipulator as input arguments and calculate the forward kinematics

map to produce an interval result. Simulation results verify that the estimated bounds are guaranteed by comparing them with Monte-Carlo simulations. The advantages of interval analysis over random sampling are found to be computational efficiency and capability to find closed interval expressions that guarantee bounding of results. Also, we propose a new method of precision design of microrobots by applying this interval formulation to the inverse kinematics problem, providing the bounds on the individual error terms of the microrobot for a given end-effector precision. Hence, custom design or configuration of a microrobotic system for a particular precision requirement can be done via this method. The contributions of this work consists of proven formulation of interval extension functions for the forward kinematics map of serial manipulators and applying this as a precision analysis and design methodology.

As for the microrobots employing untethered micro-agents, we address the mobility challenge and investigate an alternative power delivery and actuation scheme using pulsed laser. We analyze the relationships between the design of the micro-agent, the control of the power source, and the dynamical behavior of the agent on the task-space. Preliminary experiments on thermal microactuators confirm that the power delivery by focused laser can lead to desirable and predicted response in terms of the amplitude and frequency response. Then, we present a novel micro-agent design that can achieve three degrees of freedom on planar surfaces via stick-and-slip motion. We develop a photo-thermo-mechanical model and analyze the mobility of the micro-agent with respect to the mechanical design and the frequency and other temporal variables of the pulsed laser. Simulation results show that the mobility of the micro-agent can be controlled by properly choosing the design parameters.

9.1 Future Work

The directions in which this research can be advanced further are pointed out as follows:

1. The POE formulation of robot kinematics is a complete model from kinematic calibration perspective [32,95,119]. However, it only covers a subset of all possible uncertainties involved in a robotic system. For instance, it does not include non-geometric factors such as backlash, eccentricity, loading, and thermal expansion. Furthermore, robotic systems are composed not only of a manipulator but also some external sensors, fixtures, tools, and so on. For example, most microrobotics setups employ microscope cameras for additional feedback from the workspace for closed-loop control. The limited resolution of such external sensors can also be modeled using intervals and incorporated into the precision analysis of the system. Robot controller performance also plays an important role in precisely moving the manipulator links in the workspace. Hence, control errors can be incorporated in the precision analysis in a similar way.
2. Our method can be applied to the identification and calibration problems. Given a measurement of the end-effector pose in terms of interval numbers, the inverse kinematics formulation can be used to find the allowable range of parameters values. Repeating this process for all measurement locations provides a set of intervals for each parameter of the kinematic model. Then, the intersection of the intervals is a set that gives the range of the corresponding real parameter value. For parallel robots, a similar idea was implemented in [120] to find the least squares solution of a calibration problem.
3. Formulation of the robot kinematics using interval analysis and POE method has been done for serial manipulators in our work. It can easily be extended to the POE formulation of parallel robots. Parallel robots have been studied using

intervals analysis by J. P. Merlet [76, 121, 122] for optimal design, singularity detection, and forward kinematics formulation. However, intervals have not been extended to the POE formulation of parallel robots.

4. We have been building a new microassembly system at the Research Institute of UTA as shown in Fig. 9.1 and 9.2 to perform further experimental demonstrations of the methodology presented in this thesis. The system includes 15 motorized axes split into a sample stage and 2 manipulators. Also, there are two microscope cameras for visual feedback from top and side of the workspace. A computer system consisting of an operator workstation and a motion driver is used to control the operation of the system. More information about the configuration of this system is given in Appendix F.

Figure 9.1. The implementation platform: NEXuS Microassembly System, UTA Research Institute.

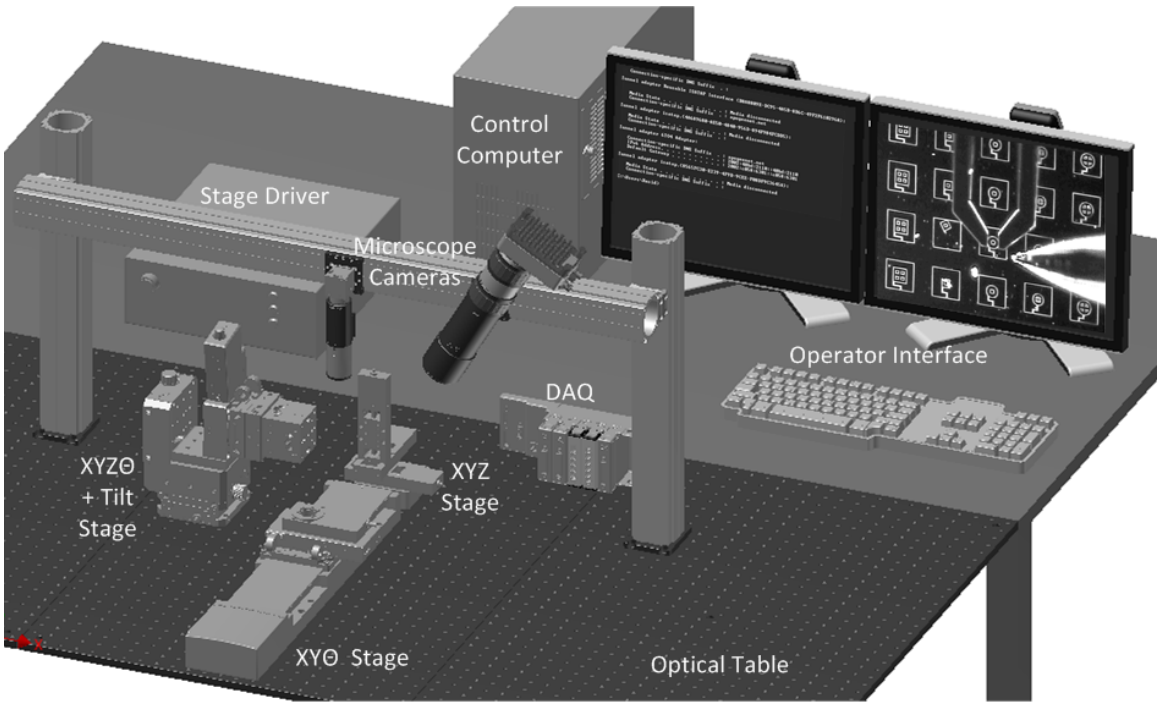

Figure 9.2. NEXuS Microassembly System CAD design.

APPENDIX A

NODAL ANALYSIS AND SIMULATION OF MEMS IN SUGAR

SUGAR is a nodal analysis toolbox for MATLAB that allows quick simulations of MEMS design ideas. It is similar to SPICE in terms of its netlist-based device specification and nodal simulation method. Bending of 2D and 3D beams, electrostatic interactions, and circuit elements can be modeled via a netlist description and simulated through numerical analysis of coupled systems of built-in differential equations. It can do static, steady-state, and modal analysis and extends to transient analysis. We used SUGAR 2.0 in our simulations [123] of the micro-actuator and micro-agent studies presented in section 7.3.

A.1 Modeling and Analysis of Pseudo Bimorph Micro-Actuator in SUGAR

We presented the results of our simulations of the pseudo bimorph micro-actuator in part 7.3.1. Here, we provide the details about the simulation netlist and MATLAB scripts that we used to perform the simulations. The nodal description of the bimorph actuator is shown in Fig. A.1 where each node is shown with a dot and the links connecting these nodes is shown with a line. The netlist file called 'leg.net' describing this nodal structure of the actuator is called from a MATLAB script as in Table A.1. The corresponding parametric subnet listing is given in Table A.2.

The parametric analysis of the actuator deflection can be done as in the MATLAB script in Table A.3 where the temperature parameter is swept from 100 to 1000 degrees Celsius and the deflection of the tip of the actuator (node c) is measured and plotted with respect to temperature.

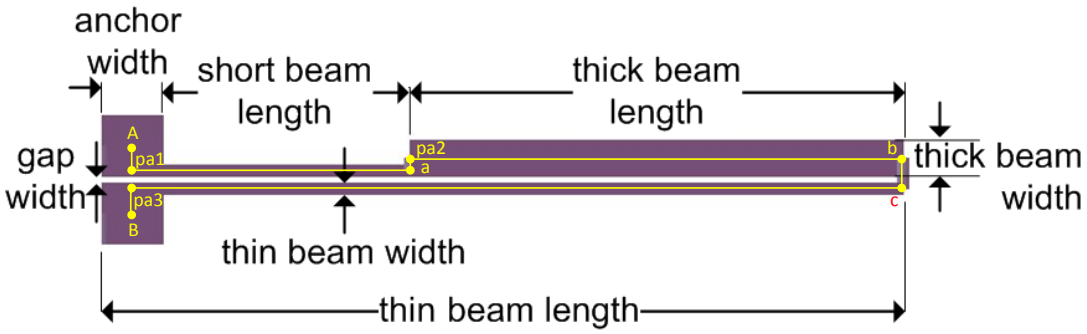

Figure A.1. Nodal description of the bimorph actuator.

Table A.1. MATLAB script calling the bimorph actuator netlist file

```
params.w_anchor = 20e-6;
params.l_short = 120e-6;
params.w_thick = 11e-6;
params.l_leg = 260e-6;
params.w_thin = 4e-6;
params.w_gap = 2e-6;
params.T_high = 600;
params.T_low = params.T_high/4;
params.F_tip = 0;
net = cho_load('leg.net', params);
q = cho_dc(net);
cho_display(net, q);
```

Table A.2. Netlist description of the bimorph actuator

```
subnet legSubnet    [A B c]          [wanchor=* lleg=* lshort=* wthin=* wthick=* wgap=*
                                     oxh=* oyh=* ozh=* Tlow=* Thigh=* force=*]
[
anchor              parent [A]       [l=wanchor w=wanchor ox=oxh oy=oyh oz=ozh]
pre_arm1 beam3d     parent [A pa1]   [l=wanchor/2-wthin/2 w=wthin T=Tlow ox=oxh
                                     oy=oyh oz=-pi/2+ozh]
short_arm beam3d    parent [pa1 a]   [l=lshort w=4u T=Tlow ox=oxh oy=oyh oz=ozh]
pre_arm2 beam3d     parent [a pa2]   [l=wthick/2-wthin/2 w=wthin T=Tlow ox=oxh
                                     oy=oyh oz=pi/2+ozh]
thick_arm beam3d    parent [pa2 b]   [l=lleg-lshort w=wthick T=Tlow ox=oxh oy=oyh oz=ozh]
bridge beam3d       parent [b c]     [l=wthick/2+wgap+wthin/2 w=wthin T=Thigh ox=oxh
                                     oy=oyh oz=-pi/2+ozh]
thin_arm beam3d     parent [c pa3]   [l=lleg w=wthin T=Thigh ox=oxh oy=oyh oz=-pi+ozh]
pre_arm3 beam3d     parent [pa3 B]   [l=wanchor/2-wthin/2 w=wthin T=Tlow ox=oxh
                                     oy=oyh oz=-pi/2+ozh]
anchor              parent [B]       [l=wanchor w=wanchor ox=oxh oy=oyh oz=ozh]
f3d *               [c]              [F=force oz=pi/2]
]
```

```
% leg.net
uses mumps.net
uses legSubnet.net

param w_anchor      param l_short    param w_thick
param l_leg         param w_thin     param w_gap
param T_low         param T_high     param F_tip

leg1 legSubnet      p1 [a b]         [wanchor=w_anchor lleg=l_leg lshort=l_short
                                     wthin=w_thin wthick=w_thick wgap=w_gap oxh=0
                                     oyh=0 ozh=0 Tlow=T_low Thigh=T_high force=F_tip]
```

Table A.3. MATLAB script sweeping the temperature and measuring tip deflection

```
params.w_anchor = 20e-6;
params.l_short = 120e-6;
params.w_thick = 11e-6;
params.l_leg = 260e-6;
params.w_thin = 4e-6;
params.w_gap = 2e-6;
params.F_tip = 0;

temp = [100 200 300 400 500 600 700 800 900 1000];
for i=1:10,
params.T_high = temp(i);
params.T_low = temp(i)/4;
net = cho_load('leg.net', params);
q = cho_dc(net);
defl(i) = cho_dq_view(q, net, 'c', 'y');
end plot(temp, defl);
xlabel('Temperature (C)');
ylabel('Deflection (m)');
grid on
```

A.2 Modeling and Analysis of Chevron Micro-Actuator in SUGAR

We presented the results of our simulations of the chevron micro-actuator in part 7.3.2. Here, we provide the details about the simulation netlist and MATLAB scripts that we used to perform the simulations. The nodal description of the chevron actuator is shown in Fig. A.2 where each node is shown with a dot and the links connecting these nodes is shown with a line. The netlist file called 'chevronMulti-Subnet.net' describing this nodal structure of the actuator is called from a MATLAB script as in Table A.4. The corresponding parametric subnet listing is given in Table A.5.

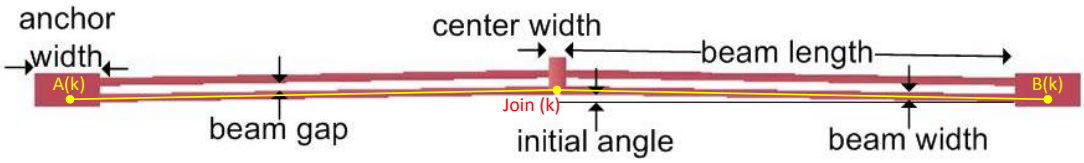

Figure A.2. Nodal description of the chevron actuator.

Table A.4. MATLAB script calling the bimorph actuator netlist file

```
params.w_anchor=10e-6;
params.w_center = 5e-6;
params.l_beam = 140e-6;
params.w_beam = 2.5e-6;
params.w_gap = 2.5e-6;
params.angle_Zero = pi/180;
params.ox_h = 0;
params.oy_h = 0;
params.oz_h = 0;
params.T_high = 0;
params.force = 0;
params.beamNum = 4;

net = cho_load('chevronActuator.net', params);
cho_display(net);
```

Table A.5. Netlist description of the chevron actuator

```
subnet chevronSubnet    [A B join]           [lbeam=* wbeam=* angleZero=* oxh=*
                                             oyh=* ozh=* Thigh=*]
[
left1 beam3d            parent [A join]      [l=lbeam w=wbeam T=Thigh ox=oxh
                                             oy=oyh oz=ozh+angleZero]
right1 beam3d           parent [join B]      [l=lbeam w=wbeam T=Thigh ox=oxh
                                             oy=oyh oz=ozh-angleZero]
]
```

```
% chevronActuator.net
uses mumps.net
uses chevronSubnet.net

param w_anchor          param w_center       param l_beam
param w_beam            param w_gap          param angle_Zero
param ox_h              param oy_h           param oz_h
param T_high            param force          param beamNum

for k=1:beamNum
[
anchor p1               [A(k)]               [w=(w_gap+w_beam) l=w_anchor oz=pi+oz_h]
anchor p1               [B(k)]               [w=(w_gap+w_beam) l=w_anchor oz=oz_h]
chevronSubnet p1        [A(k) B(k) join(k)]  [lbeam=l_beam wbeam=w_beam angleZero=angle_Zero
                                             oxh=ox_h oyh=oy_h ozh=oz_h Thigh=T_high]
]
for k=1:beamNum-1
[
beam3d p1               [join(k) join(k+1)]  [l=(w_gap+w_beam) w=w_center oz=pi/2+oz_h]
]
beam3d p1               [join(beamNum) tip]  [l=(w_gap+w_beam) w=w_center oz=pi/2+oz_h]

f3d *                   [tip]                [F=force oz=-pi/2+oz_h]
```

APPENDIX B

MICRO-AGENT SIMULATIONS IN MATLAB/SIMULINK

The MATLAB/Simulink model that we developed to simulate the laser-driven micro-agent presented in section 7.5 is explained here in this appendix. Figure B.1 shows the overall Simulink model diagram that basically implements the model of the thermal network in Fig. 7.28.

The lumped thermal masses in B.1 such as Frames L/R, Beam L/R, and Leg L/R are modeled using the control volume equations from 7.6 to 7.12 as in Fig. B.2.

Figures B.3 and B.4 show the details of the thermo-mechanical model presented in part 7.5.4.

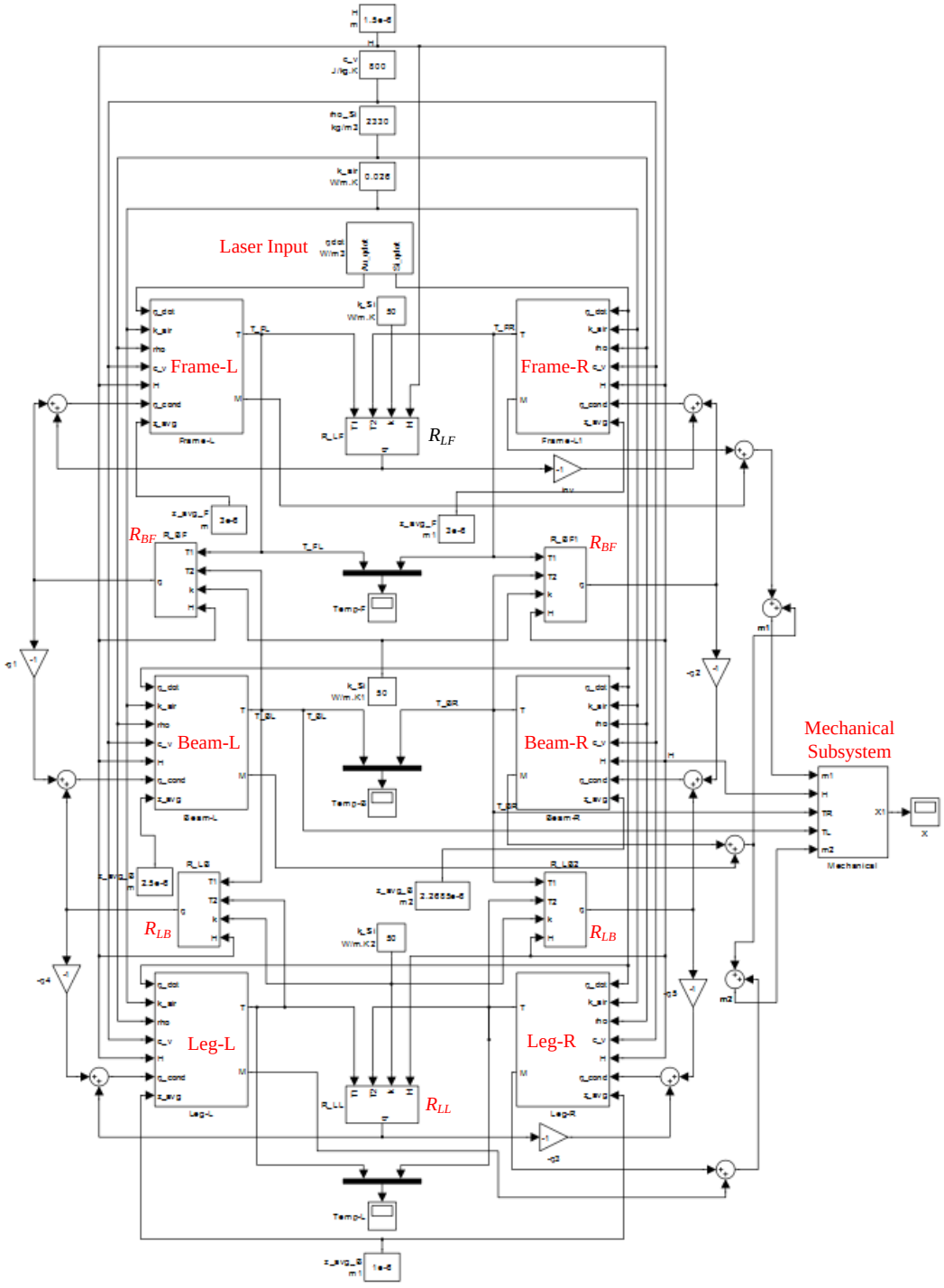

Figure B.1. Laser-driven micro-agent Simulink overall model.

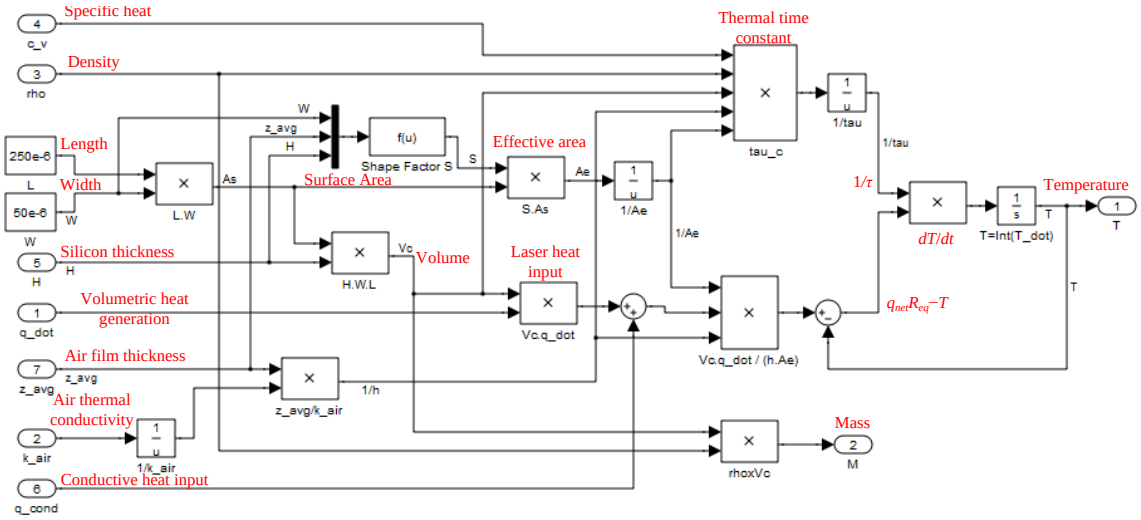

Figure B.2. Frame and beam: Control volume thermal model.

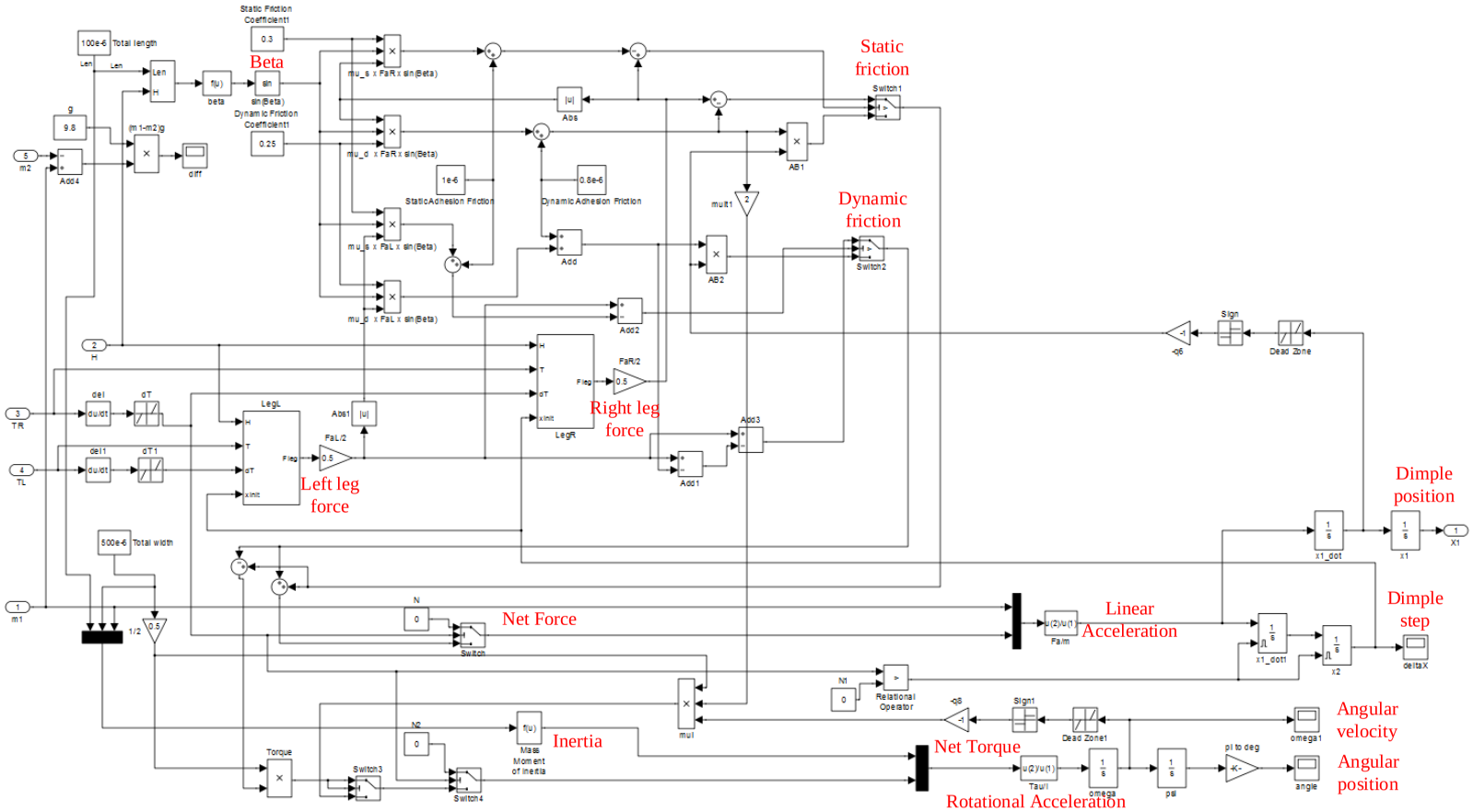

Figure B.3. Mechanical subsystem: Thermo-mechanical model.

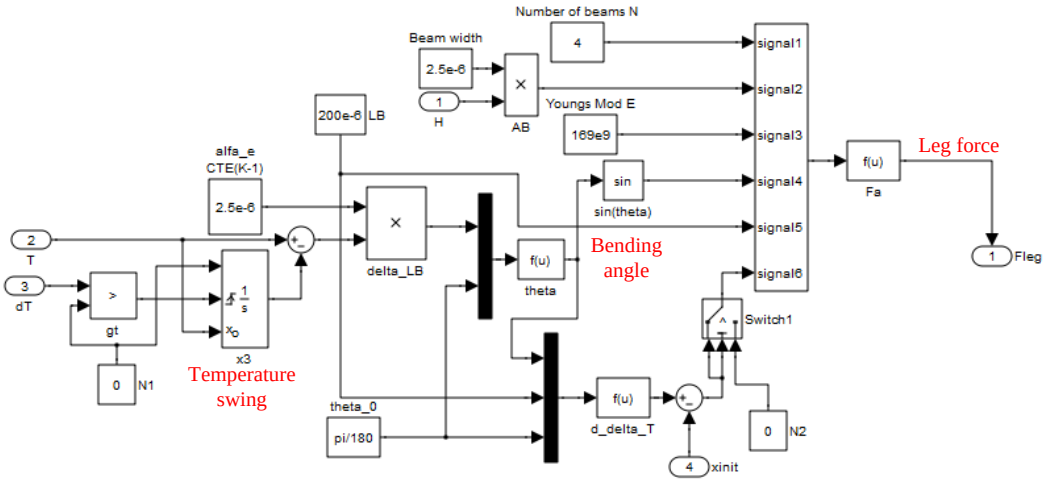

Figure B.4. Leg actuator thermo-mechanical model.

APPENDIX C

MICROFABRICATION RECIPE

Table C.1 shows the steps of the Silicon-On-Insulator (SOI) MEMS microfabrication process used in making micro-parts, micro-actuators, and micro-agents discussed earlier. Except for steps 10 and 12, all the processes can be carried out at UTA NanoFab facility. Step 12 is optional if wet resist removal is not sufficient.

Table C.1.

No	Step	Equipment	Recipe
1	Cleaning	Wet Bench	Acetone dip or pirahna H2SO4:H2O2/3:1 ratio, 90-110^o , 10min. DI rinse and N-blow
2	Priming	Spinner	MCC primer, ramp: 800 rpm/s, spin: 4000 rpm for 30 s
3	Primer Bake	Hot Plate	At 150^o for 3 min
4	Spin Coat	Spinner	SPR220-3, step 1 - ramp: 200 rpm/s spin: speed 800 rpm for 4s, step 2 - ramp: 800 rpm/s spin: speed 4000 rpm for 30 s
5	Soft Bake	Hot Plate	115^o for 90 s
6	Exposure	Aligner	For 8 s at 150 mJ/cm^2
7	PEB	Hot Plate	115^o for 90 s
8	Develop	Dev. Hood	60 s in MF-24A, 30 s in DI, rinse
9	Hard Bake	Hot Plate	115^o for 1 hour
10	Etch	DRIE	Deep silicon recipe
11	Stripping	Base Bench	Microposit 1165 bath: 5 min, rinse: 5 min
12	Stripping	Asher	200 mT with O2, 200 W, 30 min
13	Release	Acid Bench	step 1 - 49%HF dip, 2 um/min etch rate step 2 - DI water soak, 10 min step 3 - IPA soak until CPD
14	Drying	Super CPD	Regular process

APPENDIX D

MICRO-AGENT CONTROL INTERFACES IN LABVIEW

LabView has been used in controlling the micro-agent systems discussed in Chapter 7. We developed LabView programs to test and control them. Figure D.1 shows a snapshot of the LabView test program that performs an automated frequency sweep test for the vibration-driven micro-agent. The NI-1742 smart camera is used to track the micro-agent while this program records the applied vibration frequency, micro-agent pose, and velocity.

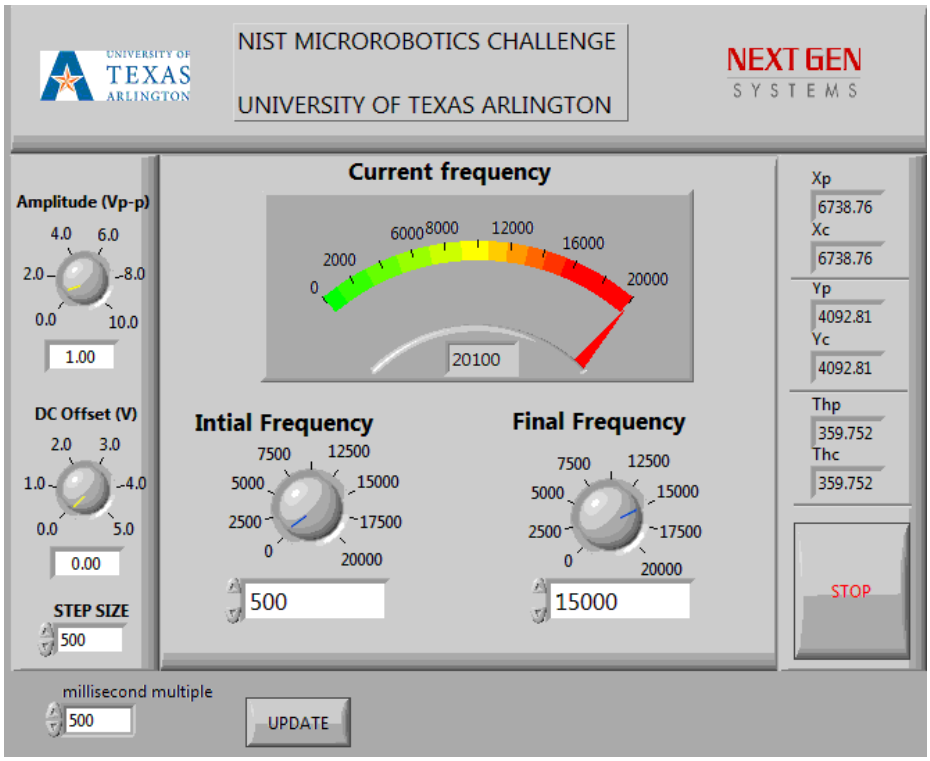

Figure D.1. LabView interface used to characterize the vibration-driven micro-agent.

Figure D.2 show the control program of the magnetically-driven micro-agent. The position of the driving magnet that is underlying the arena seen on the picture is shown with a small green square. The position of that magnet is know based on the stage encoder feedback and prior calibration with respect to the camera reference frame.

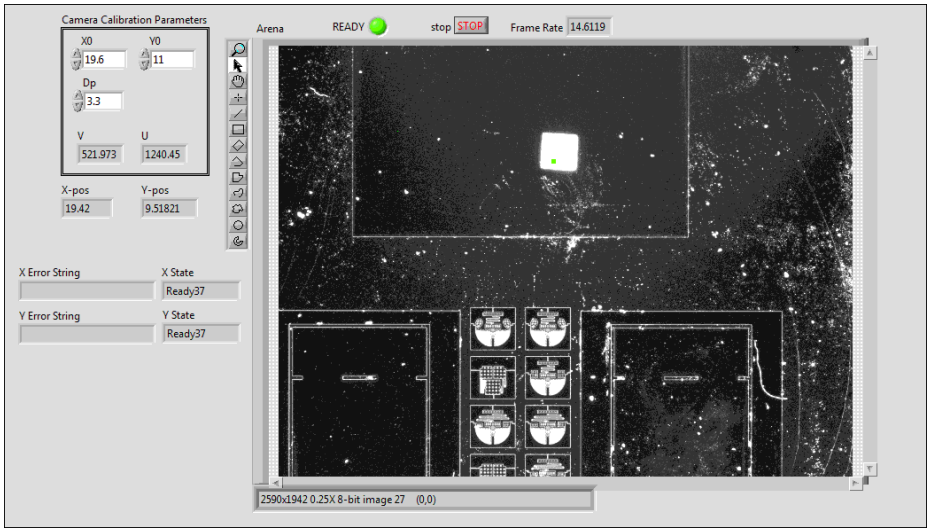

Figure D.2. LabView interface used to control the magnetically-driven micro-agent.

APPENDIX E

NIST MOBILE MICROROBOTICS CHALLENGE

Microrobots are envisaged to be useful in many future applications such as nanomanufacturing, in-vivo operations, exploration of small structures, as well as military surveillance. Recognizing the promise of this research, the National Institute of Standards and Technology (NIST) has started organizing the microrobotics challenge in 2007 in collaboration with the Institute of Electrical and Electronics Engineers (IEEE). The objective is to design devices of size in fractions of a millimeter such that they can be viewed under a microscope and operated by remote control to accomplish micromanipulation tasks across a 4 mm playing field.

NIST hosts several participant teams from universities all over the world each year at IEEE International Conference on Robotics and Automation (ICRA).In 2011, we participated in this challenge as the UTA MicroRobotics Team for the fist time. It was held in Shanghai, China during ICRA11, May 9-13, 2011. We also participated in 2012 challenge which was held in St. Paul, Minnesota during ICRA'12, May 14-18.

In the last two years, there had been two events in the challenge:

- Mobility: a micro-agent must navigate a prescribed course through a planar track in the fastest possible time.
- Microassembly: a micro-agent must assemble multiple micro-scale components in a narrow channel.

Each competing team must furnish its own micro-agents together with the equipment used to power, operate, and control them without tethers. The longest dimension of the micro-agents must be 500 μm or less. The mobility challenge requires a micro-agent to traverse a planar figure-8 course as fast as possible. The arena shown in Fig. E.1 marks the track via gates 1 to 4. The microassembly challenge requires a micro-agent to push and assemble triangular micro-scale parts in the corridor-like passage of the arena in Fig. E.2.

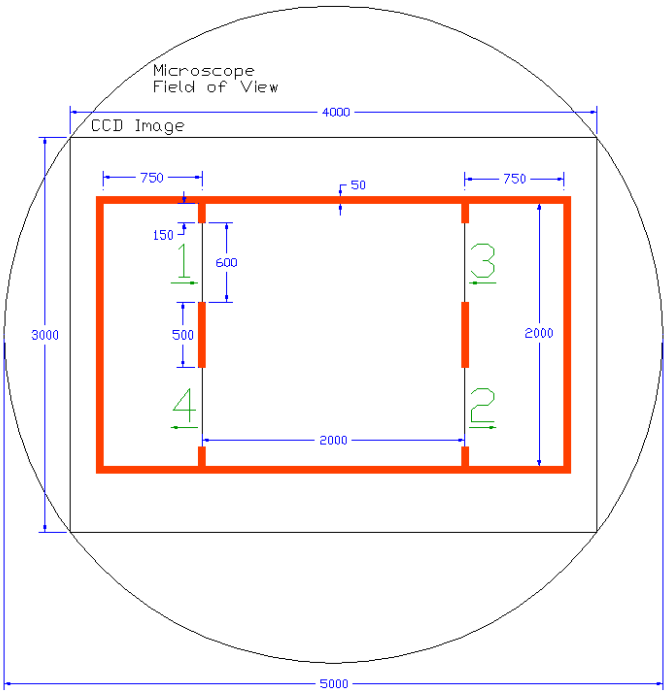

Figure E.1. Mobility challenge arena dimensions [118].

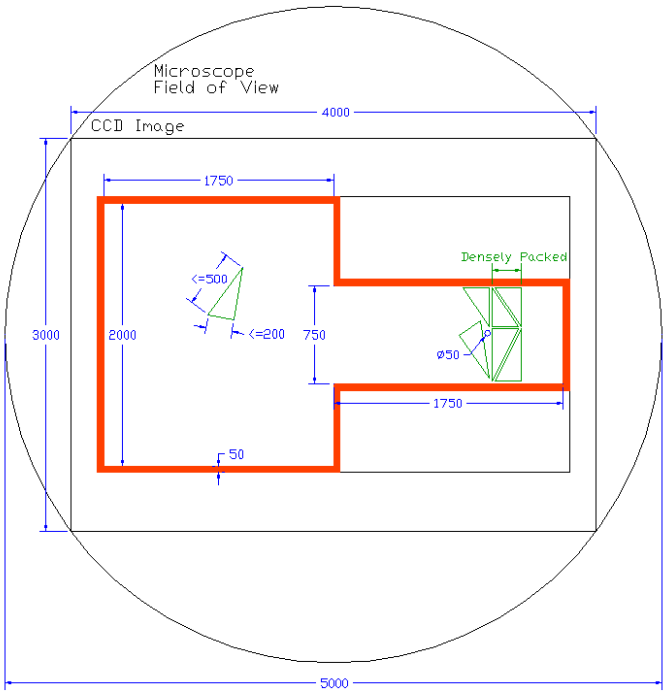

Figure E.2. Microassembly challenge arena dimensions [118].

APPENDIX F

NEXT GENERATION MICROASSEMBLY SYSTEM - NEXuS

Figure F.1 shows NEXuS system CAD design. It is basically composed of

- Stages: 15 axes of various motorized precision stages from Newport, Inc. The range of motion is from 250 mm to 25 mm and the resolution is from $1\mu m$ to $0.1\mu m$ in different stages.
- Stage Driver: A real-time 8-axis motion controller from Newport that can perform coordinated control of multiple stages.
- Cameras: Two cameras one of which is a real-time smart camera from National Instruments and the other one is a gigabit Ethernet camera from Basler Vision, AG. Both cameras are attached to microscopes from Edmund Optics with magnification up to 10.5X. Also, there are two illuminators with fiber coupled light guides and delivery rings.
- DAQ: A real-time CompactRIO data acquisition system from National Instruments with analog and digital I/O modules and a single axis motion control module.
- Computer and Interfaces: A high end computer system from Alienware, double monitors, and several interface devices such as keyboard, mouse, joystick, game controller, and a 4-DOF haptic device from Sensable.
- Micro-Tools: Micro-grippers and micro-force sensors from Femto-Tool and Kronex for micro-part gripping and micro-force sensing. Also, there are vacuum tweezers with 30-33 gauge tips from Nordson EFD.
- Dispenser: An auger dispenser from Nordson EFD for nanoliter scale epoxy dispensing.
- Fixture Frame: Construction rails from Thorlabs for precise mounting of optical components.

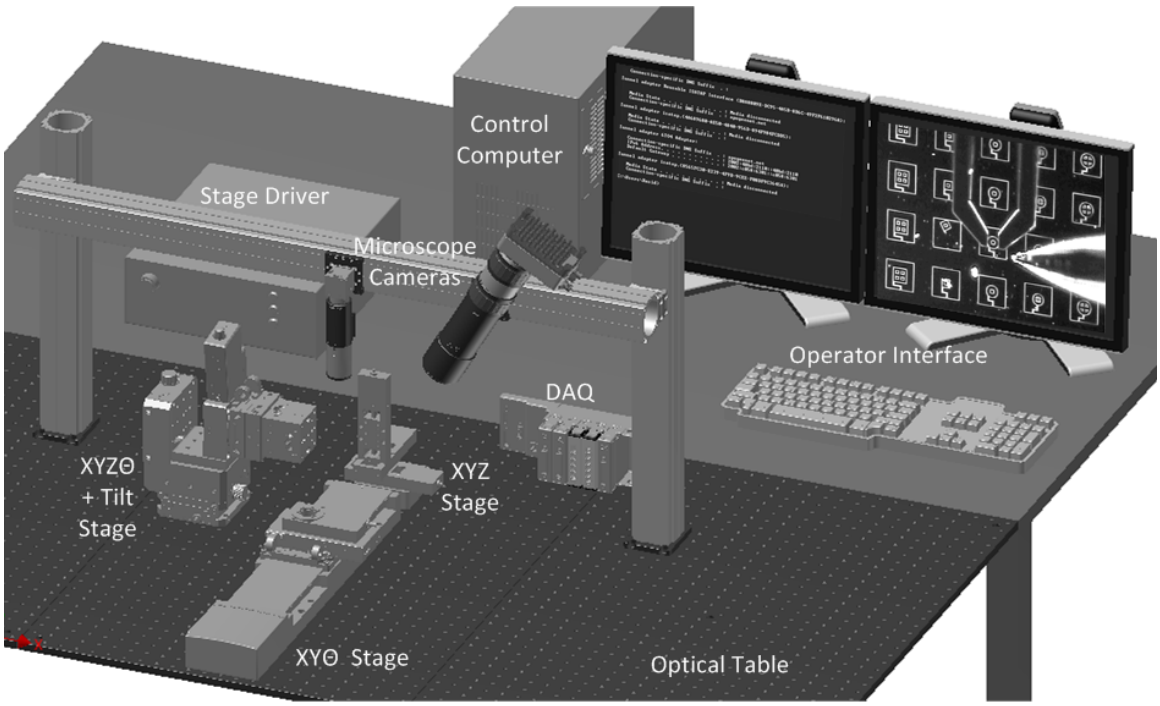

Figure F.1. NEXuS Microassembly System CAD design.

REFERENCES

[1] I. Hunter, S. Lafontaine, P. Nielsen, P. Hunter, and J. Hollerbach, "Manipulation and dynamic mechanical testing of microscopic objects using a tele-microrobot system," *IEEE Control Systems Magazine*, vol. 10, no. 2, pp. 3–9, feb. 1990.

[2] A. Codourey, W. Zesch, R. Buchh, and R. Siegwart, "High precision robots for automated handling of micro objects," Seminar on Handling and Assembly of Microparts,Inst. of Robotics, ETH-Zurich, Vienna, Tech. Rep., Nov. 1994.

[3] R. S. Fearing, "Micro-actuators for micro-robots and micro-sensors for micro-robots," in *Tutorial on MicroRobotic Principles and Applications, IEEE Int. Conf. Robotics and Automation*, May 1995.

[4] A. Sulzmann, J.-M. Breguet, and J. Jacot, "Microvision system (mvs): a 3d computer graphic-based microrobot telemanipulation and position feedback by vision," pp. 38–49, 1995.

[5] S. Johansson, "One approach towards the fabrication of a microrobot system," *Materials Science and Engineering: C*, vol. 2, no. 3, pp. 141 – 149, 1995.

[6] S. Fatikow, J. Seyfried, S. Fahlbusch, A. Buerkle, and F. Schmoeckel, "A flexible microrobot-based microassembly station," *Journal of Intelligent and Robotic Systems*, vol. 27, pp. 135–169, 2000.

[7] M. C. Carrozza, A. Eisinberg, A. Menciassi, D. Campolo, S. Micera, and P. Dario, "Towards a force-controlled microgripper for assembling biomedical microdevices," *Journal of Micromechanics and Microengineering*, vol. 10, no. 2, p. 271, 2000.

[8] Y. Bellouard, *Microrobotics: methods and applications*. CRC Press, 2010.

[9] (2012) Memscap mumps processes. [Online]. Available: http://www.memscap.com/products/mumps

[10] (2006) Sandia national labs summit process. [Online]. Available: http://mems.sandia.gov/tech-info/summit-v.html

[11] (2012) Microfabrica mica freeform process. [Online]. Available: http://www.microfabrica.com/

[12] M. Gauthier and S. Regnier, *Robotic Micro-Assembly*. Wiley-Sons, 2010.

[13] A. Das, D. Popa, J. Sin, and H. Stephanou, "Precision alignment and assembly of a fourier transform microspectrometer," *Journal of Micro - Nano Mechatronics*, vol. 5, pp. 15–28, 2009.

[14] M. Probst, R. B. C. Hrzeler, and B. J. Nelson, "A microassembly system for the flexible assembly of hybrid robotic mems devices," *International Journal of Optomechatronics*, vol. 3, no. 2, pp. 69–90, 2009.

[15] J. J. Abbott, Z. Nagy, F. Beyeler, and B. J. Nelson, "Robotics in the small, part i: Microbotics," *IEEE Robotics - Automation Magazine*, vol. 14, no. 2, pp. 92–103, 2007.

[16] R. S. Fearing, "Survey of sticking effects for micro parts handling," in *Proc. IEEE/RSJ International Conference on Intelligent Robots and Systems*, 1995.

[17] P. Lambert, *Capillary Forces in Microassembly: Modeling, Simulation, Experiments, and Case Study*. Springer, 2010.

[18] Q. Zhou, C. del Corral, P. J. Esteban, A. Aurelian, and H. N. Koivo, "Environmental influences on microassembly," in *Proc. IEEE/RSJ International Conference on Intelligent Robots and Systems*, 2002.

[19] M. Sitti, "Microscale and nanoscale robotics systems: grand challenges of robotics," *IEEE Robotics and Automation Magazine*, vol. 14, no. 1, pp. 53–60, 2007.

[20] S. J. Ralis, B. Vikramaditya, and B. J. Nelson, "Micropositioning of a weakly calibrated microassembly system using coarse-to-fine visual servoing strategies," *IEEE Transactions on Electronics Packaging Manufacturing*, vol. 23, no. 2, pp. 123–131, 2000.

[21] S. Fahlbusch and S. Fatikow, "Force sensing in microrobotic systems-an overview," *IEEE International Conference on Electronics, Circuits and Systems*, 1998.

[22] S. Fatikow, T. Wich, H. Hulsen, T. Sievers, and M. Jahnisch, "Microrobot system for automatic nanohandling inside a scanning electron microscope," *IEEE/ASME Transactions on Mechatronics*, vol. 12, no. 3, pp. 244–252, 2007.

[23] C. Clevy, C. D. C. L. Vy, M. Rakotondrabe, and N. Chaillet, *Signal Measurement and Estimation Techniques for Micro and Nanotechnology.* Springer, 2011.

[24] A. Sanchez-Salmeron, R. Lopez-Tarazon, R. Guzman-Diana, and C. Ricolfe-Viala, "Recent development in micro-handling systems for micro-manufacturing," *Journal of Materials Processing Technology*, vol. 167, no. 2-3, pp. 499 – 507, 2005.

[25] B. Greenway, "Robot accuracy," *Industrial Robot: An International Journal*, vol. 27, pp. 257–265, 2000.

[26] M. P. Groover, *Automation, Production Systems, and Computer-Integrated Manufacturing*, 3rd ed. Prentice Hall Press, 2007.

[27] S. Floyd, C. Pawashe, and M. Sitti, "An untethered magnetically actuated micro-robot capable of motion on arbitrary surfaces," in *Proc. 2008 IEEE In-*

ternational Conference on Robotics and Automation (ICRA), Pasadena, CA, May 2008, pp. 419–424.

[28] B. R. Donald, C. G. Levey, C. D. Mcgray, I. Paprotny, and D. Rus, "An untethered, electrostatic, globally controllable mems micro-robot," *Journal of Microelectromechanical Systems*, vol. 15, no. 1, pp. 1–15, 2006.

[29] S. Fatikow, T. Wich, C. Dahmen, M. Jahnisch, C. Stolle, and V. Eichhorn, "Nanohandling automation as an emerging industrial technology," *IEEE International Conference on Industrial Technology*, 2009.

[30] B. J. Nelson, I. K. Kaliakatsos, and J. J. Abbott, "Microrobots for minimally invasive medicine," *Annual Review of Biomedical Engineering*, vol. 12, no. 1, pp. 55–85, 2010.

[31] A. H. Slocum, *Precision Machine Design*. Dearborn, MI, USA: Society of Manufacturing Engineers, 1992.

[32] B. Mooring, Z. S. Roth, and M. R. Driels, *Fundamentals of Manipulator Calibration*. Wiley, 1991.

[33] B. Benhabib, R. Fenton, and A. Goldenberg, "Computer-aided joint error analysis of robots," *IEEE Journal of Robotics and Automation*, vol. 3, no. 4, pp. 317–322, Aug. 1987.

[34] J. Chen and L. Chao, "Positioning error analysis for robot manipulators with all rotary joints," *IEEE Journal of Robotics and Automation*, vol. 3, no. 6, pp. 539–545, Dec. 1987.

[35] Z. Huang, "Error analysis of position and orientation in robot manipulators," *Mechanism and Machine Theory*, vol. 22, no. 6, pp. 577–581, 1987.

[36] V. Kiridena and P. M. Ferreira, "Mapping the effects of positioning errors on the volumetric accuracy of five-axis cnc machine tools," *International Journal of Machine Tools and Manufacture*, vol. 33, no. 3, pp. 417–437, June 1993.

[37] P. Lin and K. Ehmann, "Direct volumetric error evaluation for multi-axis machines," *International Journal of Machine Tools and Manufacture*, vol. 33, no. 5, pp. 675–693, Oct. 1993.

[38] J. Mou, "A systematic approach to enhance machine tool accuracy for precision manufacturing," *International Journal of Machine Tools and Manufacture*, vol. 37, no. 5, pp. 669–685, May 1997.

[39] Y. Shin and Y. Wei, "A statistical analysis of positional errors of a multiaxis machine tool," *Precision Engineering*, vol. 14, no. 3, pp. 139–146, July 1992.

[40] J. Soons, F. Theuws, and P. Schellekens, "Modeling the errors of multi-axis machines: a general methodology," *Precision Engineering*, vol. 14, no. 1, pp. 5–19, Jan. 1992.

[41] R. N. Vaishnav and E. B. Magrab, "A general procedure to evaluate robot positioning errors," *International Journal of Robotics Research*, vol. 6, no. 59, pp. 59–74, Mar. 1987.

[42] K. W. Chase and A. R. Parkinson, "A survey of research in the application of tolerance analysis to design of mechanical assemblies," *Research in Engineering Design*, vol. 3, pp. 23–37, 1991.

[43] W. Wu and S. S. Rao, "Uncertainty analysis and allocation of joint tolerances in robot manipulators based on interval analysis," *Reliability Eng. and System Safety*, vol. 92, pp. 54–64, 2007.

[44] E. Lee, C. Mavroidis, and J. P. Merlet, "Five precision points synthesis of spatial rrr manipulators using interval analysis," *ASME Conference Proceedings*, no. 36533, pp. 635–644, 2002.

[45] N. Dechev, W. L. Cleghorn, and J. K. Mills, "Microassembly of 3-d microstructures using a compliant, passive microgripper," *Journal of Microelectromechanical Systems*, vol. 13, no. 2, pp. 176–189, Apr. 2004.

[46] A. N. Das, R. Murthy, D. O. Popa, and H. E. Stephanou, "A multiscale assembly and packaging system for manufacturing of complex micro-nano devices," *IEEE Transactions on Automation Science and Engineering*, vol. 9, no. 1, pp. 160–170, 2012.

[47] K. Yesin, P. Exner, K. Vollmers, and B. Nelson, "Design and control of in-vivo magnetic microrobots," in *Medical Image Computing and Computer-Assisted Intervention*, J. Duncan and G. Gerig, Eds. MICCAI, 2005, pp. 819–826.

[48] C. Pawashe, S. Floyd, and M. Sitti, "Modeling and experimental characterization of an untethered magnetic micro-robot," *The International Journal of Robotics Research*, vol. 28, no. 8, pp. 1077–1094, 2009.

[49] D. R. Frutiger, K. Vollmers, B. E. Kratochvil, and B. J. Nelson, "Small, fast, and under control: Wireless resonant magnetic micro-agents," *The International Journal of Robotics Research*, vol. 29, no. 5, pp. 613–636, 2010.

[50] I. A. Ivan, G. Hwang, J. Agnus, M. Rakotondrabe, N. Chaillet, and S. Regnier, "First experiments on magpier: A planar wireless magnetic and piezoelectric microrobot," in *Proc. 2011 IEEE International Conference on Robotics and Automation (ICRA)*, Shanghai, China, May 2011, pp. 102–108.

[51] B. E. Kratochvil, D. Frutiger, K. Vollmers, and B. J. Nelson, "Visual servoing and characterization of resonant magnetic actuators for decoupled locomotion of multiple untethered mobile microrobots," in *Proc. 2009 IEEE International Conference on Robotics and Automation (ICRA)*, Kobe, Japan, May 2009, pp. 1010–1015.

[52] B. R. Donald, C. G. Levey, I. Paprotny, and D. Rus, "Simultaneous control of multiple mems microrobots," in *Algorithmic Foundations of Robotics VIII, STAR 57*, 2010, pp. 69–84.

[53] S. Floyd, E. Diller, C. Pawashe, and M. Sitti, "Control methodologies for a heterogeneous group of untethered magnetic micro-robots," *The International Journal of Robotics Research*, vol. 30, no. 13, p. 15531565, 2011.

[54] R. E. Moore, R. B. Kearfott, and M. J. Cloud, *Introduction to Interval Analysis*. Philadelphia, PA, USA: Society for Industrial and Applied Mathematics, 2009.

[55] C. D. M. J. J. Gorman and R. A. Allen, "Mobile microrobot characterization through performance-based competitions," in *9th Workshop on Performance Metrics for Intelligent Systems*, Gaithersburg, Maryland, USA, 2009, pp. 122–126.

[56] M. Pac and D. Popa, "Interval analysis for robot precision evaluation," in *Proc. 2012 IEEE International Conference on Robotics and Automation (ICRA)*, St. Paul, MN, May 2012, pp. 1087–1092.

[57] M. R. Pac and D. O. Popa, "Interval analysis of kinematic errors in serial manipulators using product of exponentials formula," *under review for IEEE Transactions on Automation Science and Engineering*, 2012.

[58] ——, "Guaranteed manipulator precision via interval analysis of inverse kinematics," in *submitted to IEEE International Conference on Robotics and Automation*, Karlsruhe - Germany, May 2013.

[59] ——, "Interval extension of the poe formulation with applications to robot precision design," *under review for IEEE Transactions on Robotics*, 2012.

[60] ——, "Laser-powered sub-mm untethered microrobots," in *ASME 2010 International Design Engineering Technical Conferences and Computers and Information in Engineering Conference (IDETC/CIE2010)*, Montreal, Quebec, Canada, 2010, pp. 419–424.

[61] ——, "3-dof untethered microrobot powered by a single laser beam based on differential thermal dynamics," in *Proc. 2011 IEEE International Conference on Robotics and Automation (ICRA)*, Shanghai, China, May 2011, pp. 121–127.

[62] D. O. Popa, R. Murthy, and A. N. Das, "M3-deterministic, multiscale, multi-robot platform for microsystems packaging: Design and quasi-static precision evaluation," *IEEE Transactions on Automation Science and Engineering*, vol. 6, no. 2, pp. 345–361, 2009.

[63] K. B. Yesin and B. J. Nelson, "A cad model based tracking system for visually guided microassembly," *Robotica*, vol. 232, no. 4, pp. 409–418, 2005.

[64] D. J. Cappelleri, M. Fatovic, and U. Shah, "Caging micromanipulation for automated microassembly," in *Proc. 2011 IEEE International Conference on Robotics and Automation (ICRA)*, Shanghai, China, May 2011, pp. 3145–3150.

[65] Y. H. Anis, J. K. Mills, and W. L. Cleghorn, "Automated microassembly task execution using vision-based feedback control," in *International Conference on Information Acquisition*, Seogwipo-si, South Korea, 2007, pp. 476–481.

[66] D. O. P. A. N. Das and H. E. Stephanou, "Automated microassembly using precision based hybrid control," in *Proc. 2010 IEEE International Conference on Robotics and Automation (ICRA)*, Anchorage, AK, May 2010, pp. 4106–4112.

[67] D. O. Popa and H. E. Stephanou, "Micro and mesoscale robotic assembly," *WTEC Workshop: Review of U. S. Research in Robotics*, vol. 6, no. 1, pp. 52–71, 2004.

[68] K. N. Andersen, K. Carlson, D. H. Petersen, K. Mlhave, V. Eichhorn, S. Fatikow, and P. Bggild, "Electrothermal microgrippers for pick-and-place operations," *Microelectronic Engineering*, vol. 85, no. 5-6, pp. 1128–1130, 2008.

[69] S. S. Fatikow, *Automated Nanohandling by Microrobots*. Springer, 2008.

[70] T. Udeshi and K. Tsui, "Assembly sequence planning for automated micro assembly," in *6th IEEE International Symposium on Assembly and Task Planning: From Nano to Macro Assembly and Manufacturing*, Montreal, Que, 2005, pp. 98–105.

[71] G. Zhao, C. L. Teo, D. W. Hutmacher, and E. Burdet, "Force-controlled automatic microassembly of tissue engineering scaffolds," *Journal of Micromechanics and Microengineering*, vol. 20, no. 3, p. 035001, 2010.

[72] A. N. Das and D. O. Popa, "Precision evaluation of modular multiscale robots for peg-in-hole microassembly tasks," in *IEEE/RSJ Int. Conf. on Intelligent Robots and Systems*, San Francisco, CA, USA, Sept. 2011, pp. 1699–1704.

[73] W. Veitschegger and C.-H. Wu, "Robot accuracy analysis based on kinematics," *IEEE Journal of Robotics and Automation*, vol. 2, no. 3, pp. 171–179, Sept. 1986.

[74] D. Lepadatu, X. Baguenard, A. Kobi, R. Hambli, and L. Jaulin, "Process optimization using interval computation," in *Qualita*, 2005.

[75] S. Khodaygan, M. R. Movahhedy, and M. S. Fomani, "Tolerance analysis of mechanical assemblies based on modal interval and small degrees of freedom (misdof) concepts," *The International Journal of Advanced Manufacturing Technology*, vol. 50, no. 9, 2010.

[76] F. Hao and J. P. Merlet, "Multi-criteria optimal design of parallel manipulators based on interval analysis," *Mechanism and Machine Theory*, vol. 40, p. 157171, 2005.

[77] J. P. Merlet, "Solving the forward kinematics of a goughtype parallel manipulator with interval analysis," *Int. J. of Robotics Research*, vol. 23, no. 3, p. 221236, 2004.

[78] O. Didrit, M. Petitot, and E. Walter, "Guaranteed solution of direct kinematic problems for general configurations of parallel manipulators," *IEEE Transactions on Robotics and Automation*, vol. 14, no. 2, pp. 259–266, 1998.

[79] E. Lee, C. Mavrois, and J. P. Merlet, "Five precision points synthesis of spatial rrr manipulators using interval analysis," in *Proc. DETC02: 27th Biennial Mechanisms and Robotics Conf.*, 2002.

[80] A. Kortschack, A. Shirinov, T. Truper, and S. Fatikow, "Development of mobile versatile nanohandling microrobots: Design, driving principles, haptic control," *Robotica*, vol. 23, no. 4, pp. 419–434, 2005.

[81] W. Hu, K. S. Ishii, and A. T. Ohta, "Micro-assembly using optically controlled bubbles," in *International Conference on Optical MEMS and Nanophotonics (OMN)*, Istanbul, Turkey, Aug. 2011, pp. 53–54.

[82] K. Vollmers, D. R. Frutiger, B. E. Kratochvil, and B. J. Nelson, "Wireless resonant magnetic microactuator for untethered mobile microrobots," *Applied Physics Letters*, vol. 92, no. 14, p. 144103, 2008.

[83] C. Liu, H. Z. Y. He, and D. Zhang, "Analysis and experimentation of novel asymmetric photo-thermal micro-actuator," *Fourth International Symposium on Precision Mechanical Measurements , Proc. of SPIE*, vol. 7130, no. 3, p. 713011, 2008.

[84] F. R. Szabo and P. E. Kladitis, "Design, modeling and testing of polysilicon optothermal actuators for power scavenging wireless microrobots," in *International Conference on MEMS, NANO and Smart Systems*, 2004.

[85] C. Elbuken, L. Gui, C. L. Ren, M. Yavuz, and M. B. Khamesee, "Design and analysis of a polymeric photo-thermal microactuator," *Sensors and Actuators A: Physical*, vol. 147, no. 1, pp. 292–299, 2008.

[86] O. J. Sul, M. R. Falvo, R. M. Taylor, S. Washburn, and R. Superfine, "Thermally actuated untethered impact-driven locomotive microdevices," *Applied Physics Letters*, vol. 89, no. 20, p. 203512, 2006.

[87] S. Martel, C. C. Tremblay, S. Ngakeng, and G. Langlois, "Controlled manipulation and actuation of micro-objects with magnetotactic bacteria," *Applied Physics Letters*, vol. 89, no. 23, p. 233904, 2006.

[88] E. Steager, C. Kim, J. Patel, S. Bith, C. Naik, L. Reber, and M. J. Kim, "Control of microfabricated structures powered by flagellated bacteria using phototaxis," *Applied Physics Letters*, vol. 90, no. 26, p. 263901, 2007.

[89] M. S. Sakar, E. B. Steager, H. K. Dal, J. A. Agung, M. J. Kim, V. Kumar, and G. J. Pappas, "Modeling, control and experimental characterization of microbiorobots," *The International Journal of Robotics Research*, vol. 30, no. 6, pp. 647–658, May 2011.

[90] B. Behkam and M. Sitti, "Bacteria integrated swimming microrobots," in *50 Years of Artificial Intelligence*, M. Lungarella, F. Iida, J. Bongard, and R. Pfeifer, Eds. Springer Berlin Heidelberg, 2007, pp. 154–163.

[91] E. B. Steager, M. S. Sakar, D. H. Kim, V. Kumar, G. J. Pappas, and M. J. Kim, "Electrokinetic and optical control of bacterial microrobots," *Journal of Micromechanics and Microengineering*, vol. 21, no. 3, p. 035001, 2011.

[92] L. Jaulin, M. Kieffel, O. Ditrit, and E. Walter, *Applied Interval Analysis*. London, Great Britain: Springer-Verlag, 2001.

[93] L. Jaulin and E. Walter, "Set inversion via interval analysis for nonlinear bounded-error estimation," *Automatica*, vol. 29, no. 4, pp. 1053–1064, Nov. 1993.

[94] L. Everett, "Kinematic modelling for robot calibration," in *Proc. IEEE International Conference on Robotics and Automation*, vol. 4, mar 1987, pp. 183–189.

[95] R. He, Y. Zhao, S. Yang, and S. Yang, "Kinematic-parameter identification for serial-robot calibration based on poe formula," *IEEE TRANSACTIONS ON ROBOTICS*, vol. 26, p. 411423, 2010.

[96] R. M. Murray, Z. Li, and S. S. Sastry, *A Mathematical Introduction to Robotic Manipulation*. CRC Press, 1994.

[97] K.-P. Chiao, "Fundamental properties of interval vector max-norm," *Tamsui Oxford Journal of Mathematical Sciences*, vol. 18, no. 2, pp. 219–233, 2002.

[98] S. M. Rump, "Intlab interval laboratory," in *Developments in Realiable Computing*, T. Csendes, Ed. Dordrecht: Kluwer Academic Publishers, 1999, pp. 77–104.

[99] E. P. Oppenheimer and A. N. Michel, "Application of interval analysis techniques to linear systems: Part ii the interval matrix exponential function," *IEEE Transactions on Circuits and Systems*, vol. 35, no. 10, pp. 1230–1242, 1998.

[100] A. Goldsztejn, "On the exponentiation of interval matrices," *ArXiv e-prints*, Aug. 2009.

[101] C. Moler and C. V. Loan, "Nineteen dubious ways to compute the exponential of a matrix, twenty-five years later," *SIAM Review*, vol. 45, no. 1, pp. 3–49, 2003.

[102] M. Ceberio and L. Granvilliers, "Horners rule for interval evaluation revisited," *Computing*, vol. 69, pp. 51–81, 2002.

[103] J. J. Craig, *Introduction to Robotics: Mechanics and Control*, 3rd ed. NJ, USA: Pearson Prentice Hall, 2005.

[104] L. Jaulin and E. Walter, "Guaranteed nonlinear parameter estimation from bounded-error data via interval analysis," *Mathematics and Computers in Simulation*, vol. 35, no. 2, pp. 123–137, Apr. 1993.

[105] O. Felfoul, E. Aboussouan, A. Chanu, and S. Martel, "Real-time positioning and tracking technique for endovascular untethered microrobots propelled by mri gradients," in *Proc. 2009 IEEE International Conference on Robotics and Automation (ICRA)*, Kobe, Japan, May 2009, pp. 2693–2698.

[106] J. V. Clark, D. Bindel, N. Zhou, S. Bhave, Z. Bai, J. Demmel, and K. S. J. Pister, "Sugar: Advancements in a 3d multi-domain simulation package for mems," in *Proceedings of the Microscale Systems: Mechanics and Measurements Symposium*, Portland, OR, 2001.

[107] Q. Huang, N. Ka, and S. Lee, "Analysis and design of polysilicon thermal flexure actuator," *Journal of Micromechanics and Microengineering*, vol. 9, no. 1, p. 64, 1999.

[108] L. Que, J.-S. Park, and Y. B. Gianchandani, "Bent-beam electrothermal actuators-part i: Single beam and cascaded devices," *Journal of Microelectromechanical Systems*, vol. 10, no. 2, pp. 247–254, 2001.

[109] N. I. of Standards and Technology. (2011) Nist mobile microrobotics challenge 2011. [Online]. Available: http://www.nist.gov/el/isd/mmc/, 2011

[110] M. Brown, T. Hubbard, and M. Kujath, "Development of a long-range untethered frictional microcrawler," *Journal of Micromechanics and Microengineering*, vol. 17, no. 5, pp. 1025–1033, 2007.

[111] K. D. Hagen, *Heat Transfer with Applications*. Prentice Hall, 1999.

[112] M. F. Modest, *Radiative Heat Transfer*, 2nd ed. Academic Press, 2003.

[113] L. C. Thomas, *Heat Transfer: Professional Version*. Capstone Pubs, 1999.

[114] T. H. R. Hickey, D. Sameoto and M. Kujath, "Time and frequency response of two-arm micromachined thermal actuators," *Journal of Micromechanics and Microengineering*, vol. 13, no. 1, pp. 40–46, 2003.

[115] L. Lin and M. Chiao, "Electrothermal responses of lineshape microstructures," *Sensors and Actuators A: Physical*, vol. 55, no. 1, pp. 35–41, 1996.

[116] M. J. Madou, *Fundamentals of Microfabrication: The Science of Miniaturization*. CRC Press, 2002.

[117] A. Cowen, G. Hames, D. Monk, S. Wilcenski, and B. Hardy. (2011) Soimumps design handbook, memscap inc. [Online]. Available: http://www.memscap.com/

[118] N. I. of Standards and Technology. (2012) Nist mobile microrobotics challenge 2012: Official rules. [Online]. Available: http://www.nist.gov/el/isd/mmc/

[119] K. Okamura and F. C. Park, "Kinematic calibration using product of exponentials formula," *Robotica*, vol. 14, p. 415421, 1996.

[120] D. Daney, N. Andreff, G. Chabert, and Y. Papegay, "Interval method for calibration of parallel robots: Vision-based experiments," *Mechanism and Machine Theory*, vol. 41, pp. 929–444, 2006.

[121] J. P. Merlet, "A formal-numerical approach for robust in-workspace singularity detection," *IEEE TRANSACTIONS ON ROBOTICS*, vol. 23, no. 3, pp. 393–402, 2007.

[122] ——, "Interval analysis for certified numerical solution of problems in robotics," *International Journal of Applied Mathematics and Computer Science*, vol. 19, no. 3, pp. 399–412, 2009.

[123] BSAC. (2001, Aug.) Sugar: A mems simulation program. manual.pdf. [Online]. Available: http://www-bsac.eecs.berkeley.edu/cadtools/sugar/

BIOGRAPHICAL STATEMENT

Muhammed Raşid Paç was born in İskenderun, Turkey in 1982. He received B.S. and M.S. degrees from Middle East Technical University (METU), Ankara, Turkey, in 2004 and 2007, respectively and his PhD degree from The University of Texas at Arlington (UTA) in 2012, all in Electrical Engineering. From 2004 to 2009, he was with The Scientific and Technological Research Council of Turkey (TÜBİTAK), Ankara, Turkey as a research and development engineer. In 2009, he joined the Research Institute of UTA (UTARI) as a research assistant and also served as a teaching assistant at the Electrical Engineering Department of UTA until 2012. His current research interests include industrial robotics and automation.